Gating and modulation of acid-sensing ion channels

by

Nathan B. Yoder

A dissertation

Presented to the Neuroscience Graduate Program and Oregon Health and Science University School of Medicine in partial fulfillment of the requirements for the degree of:

Doctor of Philosophy

September, 2019

School of Medicine

Oregon Health and Science University

CERTIFICATE OF APPROVAL

This is to certify that the Ph.D. dissertation of

NATHAN B. YODER

has been approved on September 3, 2019

Advisor, Eric Gouaux, Ph.D.

Member and Chair, Francis Valiyaveetil, Ph.D.

Member, Show-Ling Shyng, Ph.D.

Member, Isabelle Baconguis, Ph.D.

Member, Steve Reichow, Ph.D.

Member, William Zagotta, Ph.D.

TABLE OF CONTENTS

Acknowledgements

The success of this work would not have been possible without the constant support and guidance of my mentor, Eric Gouaux, who taught me to approach science with creativity and independence and who never failed to keep me pointed in the right direction despite my best efforts to the contrary. I would also like to thank all of the Gouaux Lab members – both past and present – who have been by my side at every step of this process. Their patience with an inexperienced graduate student as well as their kindness and comradery made the lab a truly special to be. Thanks as well to the members of my thesis defense committee for dedicating their time to supporting my education and advising my research. Special thanks to Jason Shepherd for taking a chance on me at the earliest stage of my career and without whom this may never have happened.

Separately, a huge thank you to my friends and classmates for their unapologetic passion for both science and adventure and for sharing in all of the highs and lows of this experience, they deserve much of the credit for getting me to the finish line in one piece. Finally, I would like to thank my parents, Karen and Scot, and my sister, Katelyn, for decades spent encouraging me to follow my dreams and for always providing the support required to do so. Last, I would like to thank my fiancé, Taryn, not only her love and patience through a challenging five years, but for her endless – and infectious – enthusiasm for discovery.

List of Tables

List of Figures

List of Abbreviations

Δ13	chicken acid-sensing ion channel 1a residues 14-463
Δ25	chicken acid-sensing ion channel 1a residues 25-463
ΔASIC1	chicken acid-sensing ion channel 1a residues 26-463
5-HT	5-hydroxytryptamine
ABS	acrylonitrile butadiene
ALS	Advanced Light Source
AMPA	α-amino-3-hydroxy-5-methyl-4-isoxazolepropionic acid
APETx2	*Anthopleura elegantissima* toxin 2
APS	Advanced Photon Source
AR	anti-reflective
ASIC	acid-sensing ion channel
ASIC1a	acid-sensing ion channel 1a
ASIC1b	acid-sensing ion channel 1b
ASIC1mfc	chicken acid-sensing ion channel 1a residues 2-463
ASIC2a	acid-sensing ion channel 2a
ASIC2b	acid-sensing ion channel 2b
ASIC3	acid-sensing ion channel 3
ASIC4	acid-sensing ion channel 4
ATP	adenosine triphosphate
C10ThioM	n-decyl-β-D-thiomaltopyranoside
cASIC1a	chicken acid-sensing ion channel 1a
CHO	Chinese hamster ovary cell
CHS	cholesteryl hemisuccinate
CNS	central nervous system
Cryo-EM	cryo-electron microscopy
CTF	contrast transfer function
DDM	n-dodecyl-β-D-maltoside
DEG	degenerin
DRG	dorsal root ganglion
DTT	dithiothreitol
ECD	extracellular domain
EDTA	ethylenediaminetetraacetic acid
EGFP	enhanced green fluorescent protein
EGTA	ethylene glycol tetraacetic acid
EMDB	electron microscopy data bank
ENaC	epithelial sodium channel
fASIC1	toadfish acid-sensing ion channel 1
FDM	fused deposition modeling
FPS	frames per second
FSC	fourier shell correlation
FSEC	fluorescence size exclusion chromatography
GABA	gamma aminobutyric acid
HEK	human embryonic kidney cell
hERG	human Ether-ago-go-related gene

HG	histidine-glycine
HPLC	high performance liquid chromatography
LED	light emitting diode
MitTx	*Micrurus tener tener* toxin
MLP	molecular lipophilicity potential
MNI-glutamate	4-methoxy-7-nitroindolinyl caged L-glutamate
MNPS.Na	2-methoxy-5-nitrophenyl sulfate sodium
nAChR	nicotinic acetylcholine receptor
NMDA	n-methyl-D-aspartate
NSAID	nonsteroidal anti-inflammatory drug
PBS	phosphate-buffered saline
PcTx1	*Psalmopoeus cambridgei* toxin 1
PDB	protein data bank
PEG	polyethylene glycol
PHA	pseudohypoaldosteronism
PLA	polylactic acid
PNS	peripheral nervous system
rASIC1a	rat acid-sensing ion channel 1a
rASIC3	rat acid-sensing ion channel 3
RT	room temperature
SEC	size exclusion chromatography
SEM	standard error of the mean
SMA	styrene-maleic acid
SSD	steady-state desensitization
TBS	tris-buffered saline
TM	transmembrane
TM1	transmembrane helix 1
TM2	transmembrane helix 2
TM2a	transmembrane helix 2a
TM2b	transmembrane helix 2b
TMD	transmembrane domain
TTL	transistor-transistor logic
UI	user interface
UV	ultraviolet

Abstract

Acid-sensing ion channels (ASICs) are proton-gated and Ca^{2+}-sensitive members of the epithelial sodium channel/degenerin (ENaC/DEG) superfamily of ion channels, a large and diverse family of ion channels that participate in a myriad of important biological functions throughout the human body. ASICs assemble as homo- or heterotrimeric channels and are primarily localized to the plasma membrane of central and peripheral neurons, where they sense changes in extracellular pH by opening a transient, Na^{+}-selective pore, commonly termed the 'open state', within milliseconds of exposure to protons that then gives way to a non-conducting 'desensitized state' within tens to hundreds of milliseconds. As such, proton-dependent gating of ASICs can be best described by a simple scheme composed of three canonical functional states: (1) high pH resting (closed), (2) low pH open and (3) low pH desensitized. At the onset of this work, x-ray structures of a homotrimeric ASIC, including in both low pH open and low pH desensitized states, informed a wide body of knowledge on the molecular mechanisms that govern channel function. The atomic structure of an ASIC in a high pH resting conformation, however, remained elusive. Moreover, despite a wealth of structural details pertaining to ASICs, the location of binding sites for divalent cations as well as the architecture of the channel's amino terminal domain, which harbors a highly conserved pair of residues long known to be critical for gating in ENaCs, were similarly unknown. Accordingly, the lack of molecular mechanisms for proton-dependent gating and modulation by divalent cations as well as a structural framework for the contribution of amino terminal residues to gating and ion conduction represented fundamental gaps in our understanding of ASICs and ENaC/DEG channels. By leveraging the inhibitory effects of divalent cations Ca^{2+} and Ba^{2+}, I determined the structure of a homotrimeric ASIC in a high pH resting conformation by both x-ray

crystallography and cryo-electron microscopy (cryo-EM). These results demonstrated that collapse of the acidic pocket is required for proton-dependent activation and that flexible linkers within the palm domain rearrange to enable channel desensitization. Moreover, the location of state-dependent Ba^{2+} sites within the acidic pocket and central vestibule, determined by anomalous scattering x-ray crystallography, indicates that inhibition of proton-dependent gating by divalent cations is at least partly due to competition for similar binding sites. To elucidate the architecture of the amino terminal domain, I developed methods to extract and purify ASICs in a lipid environment for structure determination by cryo-EM. Ensuing structures of ASICs in resting and desensitized conformations and in a membrane-like environment exposed an amino terminal re-entrant loop, absent in all prior x-ray and cryo-EM structures, comprised of residues prior to the first membrane spanning helix. The re-entrant loop lines a narrow ion permeation pathway below the selectivity filter and harbors a conserved motif central to gating in ENaCs, providing a structural rationale for the contribution of amino terminal residues to both gating and ion conduction. Finally, in an effort to determine a structure of a proton-activated ASIC, I designed and built a light-coupled cryo-plunger for time-resolved cryo-electron microscopy that uses photo-uncaging of protons to activate ASICs tens of milliseconds prior to vitrification. Ultimately, while the light-coupled cryo-plunge method was successful at generating a conformational change in isolated ASICs, I was only able to resolve the structure of the low pH desensitized channel, demonstrating the need for improved temporal resolution to fulfil the goal of capturing an ASIC in a proton-bound active conformation. Together, these data inform molecular mechanisms for proton-dependent gating and modulation, suggest a role for lipids in maintaining the integrity of the lower ion permeation pathway and introduce a structural motif central to gating and ion permeation for the entire ENaC/DEG superfamily of ion channels.

Furthermore, the development of a light-coupled cryo-plunger provides the expanding field of cryo-EM with a powerful new tool to approach the longstanding goal of time-resolved structural biology.

Chapter 1

Introduction

Bioelectric signals in the nervous system

The mammalian nervous system is a complex network consisting of billions of cells that communicate across trillions of intercellular junctions called synapses. Underlying this intra- and intercellular communication is the propagation of electrical and chemical signals along cellular membranes and across intercellular spaces, respectively. Central to both electrical and chemical signaling mechanisms in the nervous system are ion channels, specialized integral membrane proteins that permit the passage of ions such as Na^+, K^+, Ca^{2+} and Cl^- across cell membranes, often in response to specific stimuli.

The importance of ions to biological function has been understood since the late 19th century, when Sidney Ringer demonstrated that excised frog hearts continued to beat only when bathed in a solution composed of precise ionic components[1,2]. These early experiments gave rise to the concept of 'bioelectric' signals and of 'electrically excitable' cells. Then, in the early 20th century, Julius Bernstein introduced his 'membrane theory' which proposed that membranes of excitable cells were selectively permeable to K^+, and that cellular excitation – a change in membrane potential – stems from an increase in membrane permeability to other ionic species[3].

In a landmark series of papers near the middle of the 20th century, Alan Hodgkin and Andrew Huxley, working with two-electrode voltage-clamped squid giant axons, demonstrated that voltage-dependent changes in ionic conductance shape the action potential, revolutionizing our understanding of bioelectrical signals in the nervous system[4-9]. The work of Hodgkin and Huxley on voltage-dependent conductance in neuronal membranes ushered in a rich era of ion channel biophysics that, combined with the development of the single electrode patch clamp technique by Sakmann and Neher in the late 1970s[10,11] as well as the molecular cloning boom in the 1980s and 1990s, greatly expanded our understanding of ion channels and their many

biological roles. As such, we now know that ion channels are an incredibly diverse family of proteins[12] that harbor many distinct characteristics and respond not only to changes in membrane potential (voltage), as observed by Hodgkin and Huxley, but to an array of intra- and extracellular signals including, but not limited to, chemical[13], thermal[14,15] and mechanical[16] stimuli.

Ion channel structure

Despite the substantial base of biophysical research detailed in the previous section, little was understood about the molecular architecture of ion channels. This changed in dramatic fashion in 1998, when Roderick MacKinnon solved the first high-resolution x-ray structure of the bacterial voltage-gated K^+ channel KcsA[17]. Despite the laborious nature of the process, crystallization of ion channels gained steam, expanding from voltage-gated channels[18] to ligand-gated channels[19-21] and larger, more architecturally complex, neurotransmitter receptors[22-24]. The new array of atomic details on ion channel atomic structure expanded our understanding of cellular communication and signaling mechanisms in the nervous system.

While x-ray crystallography has remained, until recently, the dominant technique for determining high-resolution atomic structures of membrane proteins, the approach is not without limitations. First, obtaining highly pure and monodisperse protein at yields sufficient for crystallographic experiments is both challenging and expensive, requiring the use of large-scale recombinant expression systems and extensive chromatographic purification[25]. Furthermore, the inherent conformational flexibility and heterogeneity of membrane proteins often precludes successful crystal formation. As such, to have any chance at crystallization many complex protein targets require substantial genetic manipulation, including removal of flexible domains and the use of stability-improving residue substitutions[26].

2013 marked a dramatic turning point in membrane protein structural biology as the advent of new direct electron detectors and methods for transmission electron microscopes[27] greatly improved the resolution achievable by single-particle cryo-electron microscopy (cryo-EM) studies of membrane proteins[28]. Though already an established technique to determine ion channel structure[29,30], these rapid improvements in instrumentation and methodology catapulted cryo-EM to the forefront of membrane protein structural biology. Researchers quickly realized the numerous benefits associated with the technique when compared to x-ray crystallography including improved tolerance for the conformational heterogeneity and substantially reduced sample requirements, effectively opening an avenue to structures of full-length native-like proteins as well as macromolecular protein complexes, representing a major leap forward for the field. This pivot towards single-particle cryo-EM has been called the 'resolution revolution'[31] and the number of membrane protein structures published yearly has increased steadily ever since[32].

Acid-sensing ion channels

Acid-sensing ion channels (ASICs) are members of the epithelial sodium channel/degenerin (ENaC/DEG) superfamily of ion channels[33] that gate in response to drops in extracellular pH[34] (**Figure 1.1**). As with other members of the ENaC/DEG family, ASICs are voltage-insensitive, Na^+-selective and sensitive to amiloride[35]. Embedded in the plasma membrane of neurons, ASICs open upon binding protons, allowing an influx of Na^+ into the cell and depolarizing the neuronal membrane[36,37]. In mammals, four ASIC genes encode for at least six distinct subunits that are expressed throughout central and peripheral nervous systems. Despite years of study, however, defined contributions for ASICs in physiological and pathological processes of the nervous system have remained ambiguous.

The first evidence for ASICs was observed in 1980, when Krishtal and Pidoplichko, using a new rapid solution exchange system of their design, recorded fast-activating inward currents in rat dorsal root ganglion (DRG) neurons exposed to low pH[36]. Subsequent reports expanding upon their initial discovery indicated that multiple subtypes of this 'proton receptor' were expressed in a cell-type dependent manner and harbored distinct pH_{50} values and kinetic profiles[38-40]. These pioneering studies described a receptor for protons that was sensitive to amiloride, selective for Na^+ and occupied at least three distinct functional states: a high pH non-conducting resting state, a low pH open state and a low pH non-conducting desensitized state.

Concrete evidence of a proton-gated ion channel arrived nearly 16 years after Krishtal and Pidoplichko's initial work with the cloning of ASIC2a[41], and ASIC1a shortly thereafter[34]. To date, four ASIC genes (ASIC1-4) have been cloned, which, in concert with splice variants ASIC1a/b and ASIC2a/b in mammals and ASIC3a/b/c in humans specifically[42], comprise a total of eight known subunits. While all ASICs can assemble as heteromeric channels, proton-gated homomers composed of ASIC1a, ASIC1b, ASIC2a and ASIC3 have also been identified[43]. ASIC4, the function of which remains largely unknown, is only moderately similar to other ASICs in amino acid sequence and does not form proton-gated homomeric channels[44].

Biophysical and pharmacological properties of ASICs

Flexible stoichiometry across multiple subunits gives rise to numerous possibilities for proton-gated channels that harbor distinct kinetic, selectivity and pharmacological profiles[43]. However, with few exceptions most ASICs adhere to the following basic biophysical traits: (1) they activate in response to protons within milliseconds and enter a long-lived desensitized state within tens to hundreds of milliseconds (**Figure 1.2**), (2) they are selective to Na^+ over K^+ by ~ 10:1[45] and (3) acid-evoked currents are blocked by amiloride, a hallmark of all members of the

ENaC/DEG superfamily of ion channels[46]. Sensitivity to protons differs amongst ASICs, with homomeric ASIC3 the most sensitive (pH_{50} for activation ~ 6.7[47]) and homomeric ASIC2a the least sensitive (pH_{50} for activation ~ 4.1[48]).

ASIC gating is modulated by a number of exogenous and endogenous agents including extracellular Ca^{2+}, which, as first observed by Krishtal and colleagues, reduces acid-evoked currents from proton-gated channels[36]. Indeed, with the cloning and subsequent characterization of homomeric ASIC1a, Waldmann and colleagues confirmed that single channel conductance was decreased in the presence of Ca^{2+} and, somewhat surprisingly, that ASIC1a channels were also marginally permeable to Ca^{2+} (P_{Na}:P_{Ca} ~ 15:1)[34]. Furthermore, in 2001 Immke and McClesky demonstrated that lactic acid potentiates currents from ASIC1a and ASIC3 in an indirect manner by chelating external divalent cations, thus sensitizing channels to external protons and providing a functional role for an interaction between divalent cations and ASICs in ischemic muscle pain[49,50].

While Ca^{2+} inhibits all ASICs, the mechanism of action has been controversial and appears to be dependent on subunit composition[51,52]. Working with rat ASIC3 (rASIC3), Immke and McCleskey proposed that ASICs can be gated by relief of Ca^{2+} blockade in the absence of an accompanying conformational change[53]. Towards this end, they identified a high affinity binding site for Ca^{2+} that they predicted to exist at the extracellular entrance to the ion channel pore. Following these results, Paukert and colleagues identified two residues, Glu 425 and Asp 432, on transmembrane helix 2 of rat ASIC1a (rASIC1a) that were essential to Ca^{2+} block[52]. In contrast to the earlier mechanism proposed by Immke and McCleskey, however, Paukert and colleagues did not observe characteristic traits of gating by relief of Ca^{2+} blockade when both Ca^{2+} sites were mutated, such as constitutively open channels or abolition of proton-dependent gating.

Further confounding the development of a comprehensive mechanism for Ca^{2+} inhibition of ASICs, single channel currents recorded from toadfish ASIC1 (fASIC1) channels by Cecilia Canessa's group did not harbor classical features of an open-channel Ca^{2+} block such as a constant latency to first opening, a reduction of current amplitude or a decrease in mean open time[54]. Rather, they reported an increase in the number of open channels and a reduction in latency to first opening with reduced Ca^{2+}. Therefore, in contrast to rASIC3 and rASIC1a, the data from fASIC1 support an allosteric mechanism whereby Ca^{2+} unbinds from a site at the ECD, allowing for proton-dependent conformational changes that lead to channel activation.

Ca^{2+}, and other divalent cations in general, may compete with protons for similar binding sites at titratable residues as first suggested by Kirshtal and Pidoplichko[36]. However, given the thorough biophysical exploration of the interplay between ASICs and Ca^{2+}, it appears likely that modulation of proton-dependent gating by divalent cations may occur via multiple distinct underlying mechanisms in a subunit- and species-dependent manner. Notably, despite the wealth of structural information for ASICs, including binding sites for Cl^- and Na^+ determined via anomalous scattering x-ray crystallography (using Br^- and Cs^+, respectively)[20,55-57], binding sites for divalent cations have remained elusive. As such, developing a better understanding of where Ca^{2+} binds to ASICs and how this affects proton-dependent gating has remained a central focus within the field of ASIC biology.

In addition to Ca^{2+}, a number of other endogenous divalent cations including, but not limited to, Pb^{2+}[58], Zn^{2+}[59,60], Mg^{2+} and Ba^{2+}[51] impact ASIC gating. Interestingly, Zn^{2+} exhibits disparate effects on ASIC currents in a manner dependent on subunit composition and Zn^{2+} concentration, inhibiting acid-evoked currents from ASIC1a homomers and ASIC1a/2a heteromers at nanomolar levels[59], but potentiating some ASIC currents at micromolar

concentrations[60]. Somewhat surprisingly, the inhibitory effects of Zn^{2+} on ASIC1a appear to be mediated via a single Lys residue positioned at the top of the extracellular domain (ECD), though the molecular mechanism is still largely unknown. Conversely, potentiation of ASIC currents by Zn^{2+} is dependent on a pair of histidine residues within the ECD of ASIC2a[60].

A number of biological toxins have been identified that act as potent modulators of ASICs. The specificity and potency of these toxins have made them effective tools for studying ASIC function in vivo and have greatly contributed to expanding our understanding of the roles of ASICs in the nervous system. Furthermore, toxins have proven to be valuable tools for structural biologists, enabling researchers to bias recombinant channels towards short-lived functional states that are otherwise challenging to capture via conventional crystallographic approaches.

Psalmotoxin-1 (PcTx1) is a 40-residue inhibitor cysteine knot peptide toxin isolated from the South American tarantula[61,62]. Often classified as a potent inhibitor of ASIC1a, PcTx1 increases the apparent proton affinity of ASICs, manifesting as a reduction in acid-evoked currents due to an increased number of channels occupying a proton-bound desensitized state[63]. Therefore, PcTx1 is better classified as a 'gating modifier' of ASICs, with the observed effect on acid-evoked currents dependent on the pH of the preparation. Nevertheless, PcTx1 has been widely used to explore the effects of reducing or removing proton-dependent currents from ASIC1a[64,65].

MitTx, a heterodimeric polypeptide toxin isolated from the venom of Texas coral snakes by David Julius's group in 2011, is a potent agonist of ASIC1a[66]. Application of MitTx to cells expressing ASIC1a produces a sustained, Na^+-selective and amiloride-sensitive current with an EC_{50} in the nanomolar range, indicating that MitTx likely stabilizes a native-like open channel

conformation. Importantly, in addition to their efforts to isolate the toxin, the Julius lab defined a role for ASIC1a in nociception when they observed ASIC1a-dependent pain responses in mice injected with purified MitTx.

Additional evidence of a role for ASICs in nociception surfaced merely a year after the isolation of MitTx, when Eric Lingueglia's group identified a new class of toxin from the venom of the African black mamba that inhibits ASICs to produce a potent analgesic effect[67]. These new toxins, named Mambalgins by Lingueglia's group, belong to the three-finger family of peptide toxins and, when injected into mice, produce an analgesic effect on par with morphine but without respiratory distress. The analgesic effects of Mambalgins are mediated by ASIC1a and ASIC2a channels in central neurons and ASIC1b-containing channels in sensory neurons, further indicating a role for ASICs in both central and peripheral nociception. Intriguingly, in direct contrast to other three-finger toxins, Mambalgins do not appear to have a neurotoxin effect in mice, making them ideal templates for the development of non-opioid analgesics.

Comparatively less studied than the prior three toxins, APETx2, a 42-residue cysteine-rich peptide toxin isolated from sea anemone venom, inhibits ASIC3 homomers and ASIC3-containing heteromers with an IC_{50} in the nanomolar to micromolar range depending on channel composition. APETx2 is not selective for ASICs, however, and inhibits hERG channels[68] as well as a number of voltage-gated Na^+ channels[69].

In addition to the aforementioned toxins and endogenous ions, ASIC gating is modulated by a wide range of endogenous and exogenous agents, with pharmacological profiles differing profoundly in a subunit-dependent manner. Modulatory agents of particular relevance include, but are not limited to, nonsteroidal anti-inflammatory drugs (NSAIDs) ibuprofen (ASIC1a) and aspirin (ASIC3 and ASIC2a), which inhibit ASICs at micromolar concentrations[70], and local

anesthetics lidocaine (ASIC1a)[71] and tetracaine (ASIC3 and ASIC1b)[72], which also inhibit channels albeit at millimolar concentrations. ASIC pharmacology is quite convoluted given the complex interplay between subunit composition, modulator concentration and pH. Nonetheless, mounting evidence shows that ASICs play fundamental roles in nociception and fear memory formation, underscoring the importance of developing targeted pharmaceutical agents against these channels.

Roles for ASICs in the nervous system

A wide expression pattern and an array of heteromeric channels indicate that ASICs may play a variety of roles throughout the central and peripheral nervous systems. Accordingly, many roles for ASICs have been proposed through the years, including but not limited to mechanosensation[73], nociception[39,66,67], synaptic plasticity[74-76], learning and memory[77-79] and neuronal injury[64,80-83]. However, due in large part to the difficulty of controlling and measuring local pH changes and the breadth of ASIC subtypes with overlapping expression patterns, the role of protons as neurotransmitters and the functional contributions of ASICs to neuronal processes and pathologies have not been thoroughly explored in vivo. As such, despite a myriad of functional, behavioral and structural studies, a comprehensive understanding of the role the various ASICs play in the nervous system remains elusive and represents a major gap in our understanding of ASIC biology.

ASIC1a homomers and ASIC1a/2a heteromers are primarily expressed within central neurons where they co-associate with PSD-95 and are thus localized to the postsynaptic density at dendritic spines[76,84,85]. Within the central nervous system (CNS), ASIC1a homomers are particularly enriched in the amygdala[79] and, consistent with this observation, are emerging as a mediator of synaptic plasticity[75] and fear conditioning[77,78,86]. Furthermore, increasing evidence

points to a connection between ASIC1a signaling and mood disorders, including anxiety and depression[87,88], as well as addiction related behaviors[89] and, as a result, ASICs are considered valuable therapeutic targets.

Given the acidic pH (~ 5.5) of synaptic vesicles[90], the exocytic release of neurotransmitters during neuronal activity is accompanied by a release of protons into the synaptic cleft. While transient drops in synaptic pH have been observed at synapses in the retina[91,92] and the hippocampus[93] and have been implicated in an amplification of GABAergic signaling in cerebellar granule cells[94], a defined contribution by ASICs has been lacking. Recently, however, postsynaptic proton-gated and ASIC-mediated currents were observed in central neurons of the amygdala[75], nucleus accumbens[89] and at the calyx of Held, where presynaptic proton release was demonstrated to shape synaptic transmission in an ASIC1a-dependent manner[95]. These results detail a role for protons as neurotransmitters and demonstrate the capacity for postsynaptic ASICs to participate in neuronal function.

In both central and peripheral neurons, a role for ASIC1a in nociception is emerging thanks in large part to the isolation of MitTx[66] and Mambalgin[67] toxins from the venom of Texas coral and Black mamba snakes, respectively. The bites of Texas coral snakes are reported to be very painful to humans[96], and the characterization of MitTx in rodents indicates that this nociceptive response is mediated at least in part by ASIC1a channels, which are constitutively activated by MitTx in the absence of protons. Conversely, Mambalgins, isolated from Black mamba venom, produce potent analgesic effects on par with morphine via selectively and irreversibly inhibiting channels containing ASIC1a. Intriguingly, Mambalgin-mediated analgesia in rodents was absent of the dangerous respiratory side effects commonly associated with

opioids, indicating that exploitation of ASIC1a channels may be a promising target for non-opioid pain management.

Contrary to ASIC1a, which is expressed in both central and peripheral neurons, ASIC3 homomers are expressed predominantly in sensory neurons and are thus a primary mediator of proton-dependent currents in the peripheral nervous system (PNS)[97]. Given the expansive expression pattern of ASIC3 homomers across multiple cell types in the PNS, including at the soma and peripheral terminals of DRG neurons, it is likely that these channels participate in a variety of peripheral processes via a number of distinct mechanisms. Reflecting this reality, ASIC3 channels have been proposed to be involved in nociception[98], musculoskeletal pain[99], and may potentially contribute to mechanosensation via indirect and/or direct mechanisms[100].

Molecular structure of an ASIC

In stark contrast to the difficulties encountered while defining functional roles for ASICs, the family has been remarkably well-characterized from a structural perspective, with numerous high-resolution crystal structures of the homomeric ASIC1a channel in distinct conformational states solved to date. These x-ray structures of ASIC1a defined the trimeric assembly and ion permeation pathway of ASICs (**Figure 1.3**) and informed mechanisms for gating, selectivity and modulation. Moreover, these structures have greatly expanded our understanding of the architecture of the ENaC/DEG superfamily of ion channels in general.

The first atomic structure of the homomeric chicken ASIC1a (cASIC1a) channel, lacking intracellular amino and carboxy termini to improve crystal quality (ΔASIC1, residues 26-463 of cASIC1a), was determined in 2007 to a resolution of 1.9 Å by x-ray diffraction[20]. The homotrimeric ASIC contains a slender transmembrane domain (TMD) and a large threefold symmetric ECD composed of six distinct domains termed wrist, palm, finger, knuckle, thumb

and β-ball, which together resemble a clenched fist. Surface analysis of the structure exposed an 'acidic pocket' that harbored a number of carboxyl-carboxylate pairings between titratable resides of the thumb and finger domains, suggesting a proton-bound conformation consistent with the low pH conditions. Though ΔASIC1 was insensitive to protons, both the presence of asymmetric TMDs closed to ion permeation and the architecture of the acidic pocket led the authors to propose that the x-ray structure represented an ASIC in a low pH desensitized state.

Shortly after the first x-ray structure of ΔASIC1 was published, a 'minimal functional construct' (ASIC1mfc, residues 2-466 of cASIC1a) was identified that retained proton-dependent gating while being amenable to crystallization[57]. Crystals of ASIC1mfc grown at low pH diffracted to a resolution of 3 Å, exposing the structure of a desensitized channel that, unlike ΔASIC1, harbored a C3 symmetric TMD containing a tight constriction along the putative ion permeation pathway at resides Asp 433 and Gly 436. Notably, despite the discrepancies observed at the TMD, both desensitized channels shared nearly identical ECD architectures, including the characteristic carboxyl-carboxylate pairings of the proton-bound acidic pocket.

Following the structures of ASIC1a channels in proton-bound desensitized states, efforts were focused on elucidating the structure of the proton-bound open channel. However, as ASIC1a desensitized in tens to hundreds of milliseconds, efforts to crystallize the channel in a native-like open state proved insurmountable. Fortunately, ASIC1a is subject to gating modulation by a variety of pharmacological and biological agents including a number of aforementioned toxins, providing a host of valuable tools to bias isolated channels towards specific conformational states. Towards this end, two separate groups independently used PcTx1, a peptide toxin isolated from tarantula venom, to capture the first structures of ASIC1a in an open 'gating modified' state[56,101].

Structures of ΔASIC1-PcTx1 and Δ13-PcTx1 (residues 14-464 of cASIC1a) solved by Dawson and Baconguis, respectively, demonstrated that PcTx1 binds at the acidic pocket and stabilizes an open-pore conformation at the TMD. A single PcTx1 binds to each subunit of ASIC1a, anchoring to the α5 helix of the thumb domain via a hydrophobic patch and inserting two Arg resides deep into the acidic pocket. Baconguis and Gouaux crystallized Δ13-PcTx1 at both low (pH 5.5) and neutral (pH 7.5) pH, observing a Na^+-selective and asymmetric pore at low pH and a non-selective C3 symmetric pore at neutral pH. Therefore, while PcTx1 binding was independent of pH, the architecture and selectivity of the TMD was highly pH-dependent.

Fortuitously, just prior to the publication of the PcTx1-bound ASIC1a structures, David Julius's group demonstrated that MitTx, a heterodimeric polypeptide toxin isolated from the venom of the Texas coral snake, was a potent agonist of ASIC1a[66]. Furthermore, application of MitTx to rat trigeminal ganglia neurons produced a sustained, Na^+-selective and amiloride-sensitive inward current mediated by ASIC1a, indicating that MitTx likely stabilizes an open pore reminiscent of the native channel in a proton-activated state.

In collaboration with the Julius Lab, Baconguis and colleagues solved the x-ray structure of the Δ13-MitTx complex in an open state and at low pH to a resolution of 2.1 Å[55]. The heterodimeric MitTx binds 1:1 to each ASIC subunit along the length of the ECD, anchoring at the acidic pocket and extending to the wrist domain, likely activating the channel in a church key-like manner[55]. At low pH, the TMDs of the Δ13-MitTx complex adopt a threefold symmetric conformation with an open ion permeating pathway. Whole-cell patch clamp experiments of Δ13 channels activated by MitTx confirmed that the pore of the Δ13-MitTx channel is selective for Na^+, indicating that the Δ13-MitTx structure harbors a native-like open pore conformation.

Surprisingly, the TM2 helices of the Δ13-MitTx structure broke midway through the membrane to form an extended belt-like structure surrounding the pore, a feature previously unobserved in previous x-ray structures. Now known as the 'GAS belt' for the Gly-Ala-Ser residues that comprise the motif, this TM2 domain swap forms the primary constriction point along the ion permeating pathway. Interestingly, re-analysis of electron density maps from all prior x-ray structures confirmed that, while PcTx1-bound and ΔASIC1 x-ray structures clearly lack discontinuous (domain-swapped) TM2 helices, the GAS belt is indeed present in the structure of ASIC1mfc in a desensitized state at low pH.

The presence of a GAS belt in some, but not all, of the published x-ray structures, as well as the disparate and pH-dependent TM architecture of Δ13-PcTx1 complexes, clearly highlights the conformational plasticity of the ASIC TMD. While still an area of active investigation, evidence that x-ray structures of gating-modified and proton-insensitive channels lack domain-swapped TM2 helices, while both the Δ13-MitTx and ASIC1mfc structures, which best mimic the canonical functional states of ASICs, adopt domain-swapped conformations, suggests that the GAS belt is a characteristic feature of proton-gated channels.

Though less well understood than the much larger ECD, the cytoplasmic domains of ASIC are nonetheless critical for channel function. In particular, the ~ 40 residue amino terminus contains a highly conserved 'His-Gly' (HG) motif critical to proton-dependent gating in ENaCs[102] and purported to contribute to gating and ion conduction in ASICs[103,104], while the ~ 60 residue carboxy terminus is reported to be involved in mediating intracellular interactions via PDZ and α-actinin binding motifs[105,106]. Though secondary structure predictions indicate the presence of substantial helical structure at the amino terminus, electron density for all x-ray structures, including those solved at higher resolutions and those constructs containing nearly

complete amino termini, deteriorates rapidly below the membrane spanning TM helices. Accordingly, the lack of structural information related to the intracellular termini of ASICs serves as a major roadblock to developing a comprehensive understanding of ASIC and ENaC/DEG channel biology and remains an active area of investigation.

Activation of ASICs

Protons exist at a baseline concentration of ~ 40 nM in physiological solutions and are capable of binding titratable amino acid residues including Glu, Asp, His, Lys and Arg, confounding the search for both a classical ligand binding site and a truly comprehensive mechanism for proton-dependent gating of ASICs. Consistent with this notion, steep activation curves for many ASICs[43] (Hill coefficient ~ 9 for cASIC1a)[20] are indicative of multiple binding events preceding channel activation. Despite the numerous challenges, however, x-ray structures, molecular dynamics simulations and electrophysiological studies have generated a wealth of data from which the basic principles of proton-dependent gating can be reasoned.

Proton-dependent activation of ASICs is largely believed to be initiated by conformational changes within at least two distinct and highly electrostatically negative regions of the ECD: the solvent-exposed acidic pocket[20,107] and the central vestibule[108,109]. Given interplay between proton concentration and ionization states of the many titratable residues inherent to all proteins, electrostatics are likely central to proton-dependent gating mechanisms of ASICs. Towards this end, it has been proposed that changes in electrostatic potential may drive conformational changes within regions of ASICs that harbor distinct electrostatic profiles.

At low pH, the acidic pocket harbors numerous acidic Asp and Glu residues positioned such that their titratable carboxyl groups are oriented towards, and in unusually close proximity to, one another[20]. These striking carboxyl-carboxylate pairs are consistent with a proton-bound

channel and are believed to stabilize the tight interface between finger and thumb domains that maintains a 'collapsed' conformation of the acidic pocket at low pH. Consistent with this hypothesis, neutralization of residues within the acidic pocket impacts ASIC gating by altering the hill coefficient and/or shifting the pH_{50} for activation in a residue-dependent manner[20,110].

Further underscoring its contributions to channel gating, the acidic pocket also serves as a binding site for biological toxins that modulate proton-dependent gating of ASICs. Two well-characterized examples of this are PcTx1[56,101] and MitTx[55], both of which were shown to bind at the acidic pocket in x-ray structures of toxin-channel complexes. PcTx1, which anchors to a hydrophobic patch on helix α5 of the thumb domain, inserts a pair of Arg residues deep within the acidic pocket. In agreement with PcTx1 increasing the sensitivity of the channel to protons, the tight interface between thumb and finger domains indicative of a proton-bound acidic pocket is maintained at neutral pH while in the presence of PcTx1[56]. MitTx, which stabilizes homomeric ASIC1a channels in an open state, is proposed to activate ASICs in a church key-like manner by coupling the thumb domain, which frames the collapsed acidic pockets, to the wrist of the channel[55].

Situated within the core of the ECD along the molecular threefold axis, the central vestibule is another highly electrostatically negative region of the channel implicated in the proton-dependent gating of ASICs. In addition to harboring the binding site for modulators of ASIC gating including NSAIDs[70] and the inhibitor Quercetin[108], cysteine accessibility experiments indicated that the flexible lower palm domains and central vestibule of ASIC1a occupy state-dependent conformations consistent with proton-dependent gating rearrangements[111], a hypothesis later confirmed by x-ray structures[20,55-57]. Furthermore, residues

at the entrance to the central vestibule along the lower palm domain have been demonstrated to be important for proton-dependent gating[112,113].

While agonist binding and the accompanying conformational changes that initiate channel activation are believed to be localized to the ECD, residues along the short amino terminus of ASICs and ENaCs have been demonstrated to be involved in proton-dependent gating as well. Specifically, a highly conserved HG motif located just before the first membrane spanning helix is indispensable for gating in ENaCs. Mutations at the Gly position of the HG motif dramatically reduces the open probability of ENaCs[102] and disruption of this motif is known to underlie the salt wasting disorder pseudohypoaldosteronism type 1[114,115]. Additionally, a 'degenerin' site located above the ion channel gate in ASIC1a and conserved across multiple ENaC/DEG family members renders the channel constitutively open when mutated to a bulky sidechain[116-118]. Thus, a significant contribution of intracellular terminal domains and TM helices to proton-dependent gating cannot be excluded.

Desensitization of ASICs

Desensitization, or the loss of ion conduction despite the presence of agonist, is a characteristic trait of all ASICs and, with few exceptions, occurs within tens to hundreds of milliseconds after initial channel activation[43]. X-ray structures of ASIC1a in open [55,56,101] and desensitized[57] states indicate that the upper ECD of the channel adopts nearly identical conformations at low pH and that conformational changes associated with desensitization are primarily confined to the lower palm domains and the TMD.

Structural observations comparing open and desensitized channels align well with earlier predictions of residues involved in desensitization of ASIC1a. Work from the labs of Ed McCleskley, Cecilia Canessa and Stefan Gründer implicated multiple residues on the lower palm

domain[113] and on β1-β2 and β11-β12 linkers[111,119] as contributing to gating and desensitization kinetics. These results hinted at dynamic β1-β2/β11-β12 linkers and state-dependent conformations of the lower palm domain, mimicking subsequent observations from x-ray structures, which show that both β12 and β1 of the lower palm domain experience an upward translation away from the membrane, and that Asn 415 and Leu 414 of the β11-β12 linker undergo a 'side chain swap'[56] upon transition to a desensitized state. Recently, a Gln to Gly substitution at a single lower palm domain residue of human ASIC1a channels was shown to abolish both canonical desensitization and steady-state desensitization properties[120], providing strong evidence that a conformational change at the palm domain is necessary for desensitization in ASICs.

Ion selectivity of ASICs

ASICs are selective for Na^+ over K^+ by a ratio of ~ 10:1[45], with some reports indicating a slight permeability to Ca^{2+}[34]. Access for cations to the hourglass-shaped ion channel pore is mediated by extracellular fenestrations nestled at subunit-subunit interfaces between lower palm and transmembrane domains[55]. Upon activation, expansion of the extracellular vestibule ruptures the closed gate at Asp 433 and Gly 436 and dilates the extracellular fenestrations, exposing binding sites for cations at Tyr 68 via a cation-π interaction[55]. The structure of an ASIC channel bound to MitTx (Δ13-MitTx), which stabilizes an open and Na^+- selective pore, provided the first glimpse of what likely mirrors the proton-activated open pore profile and exposed discontinuous TM2 helices that form an extended GAS belt (Gly 443-Ala 444-Ser 445) motif surrounding the ion permeation pathway[55]. Below the GAS belt, the ion conduction pathway expands outwards to form a large intracellular vestibule lined by TM2b helices.

Mechanisms of selectivity and ion permeation in ASICs have been largely built upon comparisons to heteromeric ENaC channels, which are nearly tenfold more selective for Na^+ than ASICs[121,122]. In ENaCs, the high selectivity for Na^+ has long been proposed to stem from residues along the TM2 helix at a conserved G-X-S motif[35,123,124]. In the Δ13-MitTx structure, this G-X-S motif was observed to form a unique GAS belt structure separating discontinuous TM2 helices and encircling the narrowest point along the pore with a radius of 3.6 Å. Anomalous diffraction crystallographic data from Δ13-MitTx crystals soaked in Cs^+ show density along the threefold axis 4.1 Å from the carbonyl oxygen atoms of Gly 443, consistent with the coordination of a hydrated Cs^+ ion within the GAS belt of Δ13-MitTx. Therefore, a barrier mechanism was proposed for selectivity in ASICs, with the GAS belt serving as the putative selectivity filter.

Following the observation of the GAS belt in the Δ13-MitTx x-ray structure, computational and functional studies of mouse ASIC1a channels demonstrated that residues below the putative GAS selectivity filter may also contribute to ion selectivity and permeation in ASICs[125]. Residues comprising the GAS belt are not tolerant to substitutions, confounding a thorough exploration of the GAS selectivity filter hypothesis by conventional mutagenic manipulation. However, by employing unnatural amino acid substitution and molecular dynamics simulations, Lynagh and colleagues detected minimal contribution to selectivity from the GAS belt residues and instead observed that Glu 451 and Asp 454, residues along TM2b and cytoplasmic to the GAS belt, contribute more profoundly to Na^+ selectivity than had been previously anticipated. In contrast to the above observations, however, the lower pore of the Δ13-MitTx x-ray structure adopts a slayed conformation, positioning both Glu 451 and Asp 454

well away from the ion permeation pathway and making a direct contribution to ion selectivity by these residues unlikely.

The discrepancies between the structural studies of chicken ASIC1a and the functional results from mouse ASIC1a are not without potential explanations beyond a simple difference in species. Importantly, while the Δ13-MitTx complex was shown to be selective for Na^+ over K^+ in electrophysiological recordings and cations were observed within the GAS belt selectivity filter, the x-ray structure nonetheless represents the architecture of a truncated channel embedded in a detergent micelle. Thus, it is possible that the influence of a membrane environment and/or the presence of complete amino and carboxy terminal domains may alter the conformation of the TMDs observed in the Δ13-MitTx channel. Furthermore, despite strong evidence to the contrary, it is also possible that MitTx stabilizes an open channel pore that differs in profile from that opened during canonical proton-dependent activation. As such, further experimentation is required to generate a comprehensive mechanism of ion selectivity and permeation in ASICs.

Significance and approach

ASICs benefit from a rich history of both structural and functional exploration that has generated a wealth of knowledge surrounding the molecular mechanisms that govern channel function. Specifically, x-ray structures of ASIC1a have defined atomic models for desensitized[20,57], open[56] and gating-modified[56,101] channels and, informed by decades of biophysical experiments, provided detailed mechanisms for desensitization and selective ion conduction. Ultimately, however, numerous unanswered questions pertaining to the structure and function of these channels still exist, including: (1) what is the atomic structure of an ASIC in a resting state at high pH and how does proton binding lead to channel activation (2) where on ASICs does Ca^{2+} bind and how does binding modulate proton-dependent gating, and (3) what is

the architecture of the amino terminal domain and how does the HG motif contribute to gating and ion conduction? This dissertation focuses on addressing these unanswered questions by employing both structural biology and electrophysiology approaches to develop comprehensive mechanisms for proton-dependent gating and modulation of ASICs.

While my initial efforts were focused exclusively on applying crystallographic methods to determine the atomic structure of a resting ASIC at high pH and to locate binding sites for divalent cations, the bulk of this work overlapped with the aforementioned 'resolution revolution' which saw cryo-EM leap into the forefront of membrane protein structural biology. The advent of cryo-EM provided many unique opportunities to explore aspects of the structure/function relationship in ASICs and my research expanded to exploit these new capabilities. Toward this end, the conclusion of my research focused on determining structures of full-length ASICs in a membrane-like environment and determining the architecture of their amino terminal domains, thus expanding our structural understanding of ASICs in multiple functional states and, in doing so, developing new methods of cryo-EM sample preparation for capturing short-lived conformational states via 'time-resolved' cryo-EM.

Prelude to the dissertation

Chapter two focuses on the structures of Δ25 (residues 25-463 of cASIC1a) and full-length cASIC1a channels in a resting state at high pH solved by x-ray crystallography and single-particle cryo-EM methods, respectively. The structure of the resting channel highlights key conformational changes at the thumb, palm and finger domains that give rise to an expanded acidic pocket. These results show that the collapsed acidic pocket represents a proton-bound conformation while the expanded acidic pocket represents an unbound (apo) conformation, confirming that acidic pocket collapse is a critical component of channel activation. Further, the

β11-β12 and β1-β2 linkers of the resting channel share a similar architecture to those seen in the open-pore and toxin-bound channels, indicating that desensitized channels harbor a β11-β12 and β1-β2 linker conformation distinct from resting or open channels and that linker rearrangement may underlie channel desensitization. Moreover, the structure of the resting channel harbors a closed gate within the ion channel pore comprised of residues Asp 433 and Gly 436 and nearly identical to that of the desensitized channel. As such, the desensitized channel represents a 'conformational chimera', wherein a proton-bound collapsed acidic pocket maintains an open-like ECD conformation, while a rearrangement at the β11-β12 and β1-β2 linkers permits the lower palm and TMD to adopt a conformation reminiscent of the resting channel.

Chapter three explores the structural mechanisms that underlie modulation of ASIC1a gating by endogenous ions Ca^{2+} and Cl^-. Crystals of Δ25 and Δ13 channels in resting and desensitized states and at high and low pH, respectively, were soaked in $BaCl_2$ to locate divalent cation sites by anomalous scattering x-ray crystallography. Three binding sites per subunit were identified at electrostatically negative regions of the resting Δ25 channel – two in the acidic pocket and one in the central vestibule – that are understood to be important for channel gating and modulation. In contrast, the desensitized Δ13 channel harbors only a single Ba^{2+} site within the mouth of the acidic pocket, which occupies a collapsed conformation at low pH. These results demonstrate that protons and divalent cations likely compete for binding sites on ASICs and indicate that modulation of proton-dependent gating by divalent cations may hinge upon multiple state-dependent binding sites within the acidic pocket and central vestibule.

Chapter four encompasses efforts to determine the structures of full-length cASIC1a channels in a membrane-like membrane environment and in resting and desensitized conformations by single-particle cryo-EM. Accordingly, I developed methods to prepare

recombinant cASIC1a channels using styrene-maleic acid (SMA), copolymers capable of extracting and stabilizing membrane proteins surrounded by endogenous lipids. Full-length ASIC1a channels in a membrane-like environment exposed a re-entrant loop comprised of amino terminal residues with the highly conserved HG motif positioned immediately below the GAS belt TM2 domain swap, defining a role for the amino terminus of ASICs in the ion permeation pathway.

Chapter five details the design and implementation of a light-coupled cryo-plunge device for time-resolved cryo-EM experiments. To overcome the rapid desensitization kinetics of ASIC1a in pursuit of the open channel structure, I developed a custom vitrification system to pair stimulus delivery and sample vitrification within a programmable time window. Borrowing elements from mechanized sample vitrification and photochemistry, this 'flash-plunge' device consists of a high-power UV LED light source and a motorized linear actuator and is capable of vitrifying cryo-EM samples < 10 ms after stimulus (light) delivery. Accordingly, 'pH drop' experiments were intended to capture full-length cASIC1a channels in a proton-activated open state by vitrifying samples following photo-uncaging of protons. Ultimately, 'pH drop' experiments resulted in the structure of a desensitized channel, demonstrating the capacity of the flash-plunge system to generate conformational changes on a cryo-EM grid but exposing the necessity for improved temporal resolution to capture a proton-activated ASIC by this approach.

These chapters describe the structure of an ASIC in a resting state at high pH, define the architecture of the amino terminal domains and provide a unified structural framework for proton-dependent gating across all canonical ASIC functional states. Furthermore, these data expose state-dependent binding sites for divalent cations and generate new insights into the contribution of lipids to ASIC gating. Taken together, these results represent a substantial

contribution to our understanding of the intricate molecular mechanisms that govern the entire ENaC/DEG superfamily of channels.

Figures and legends

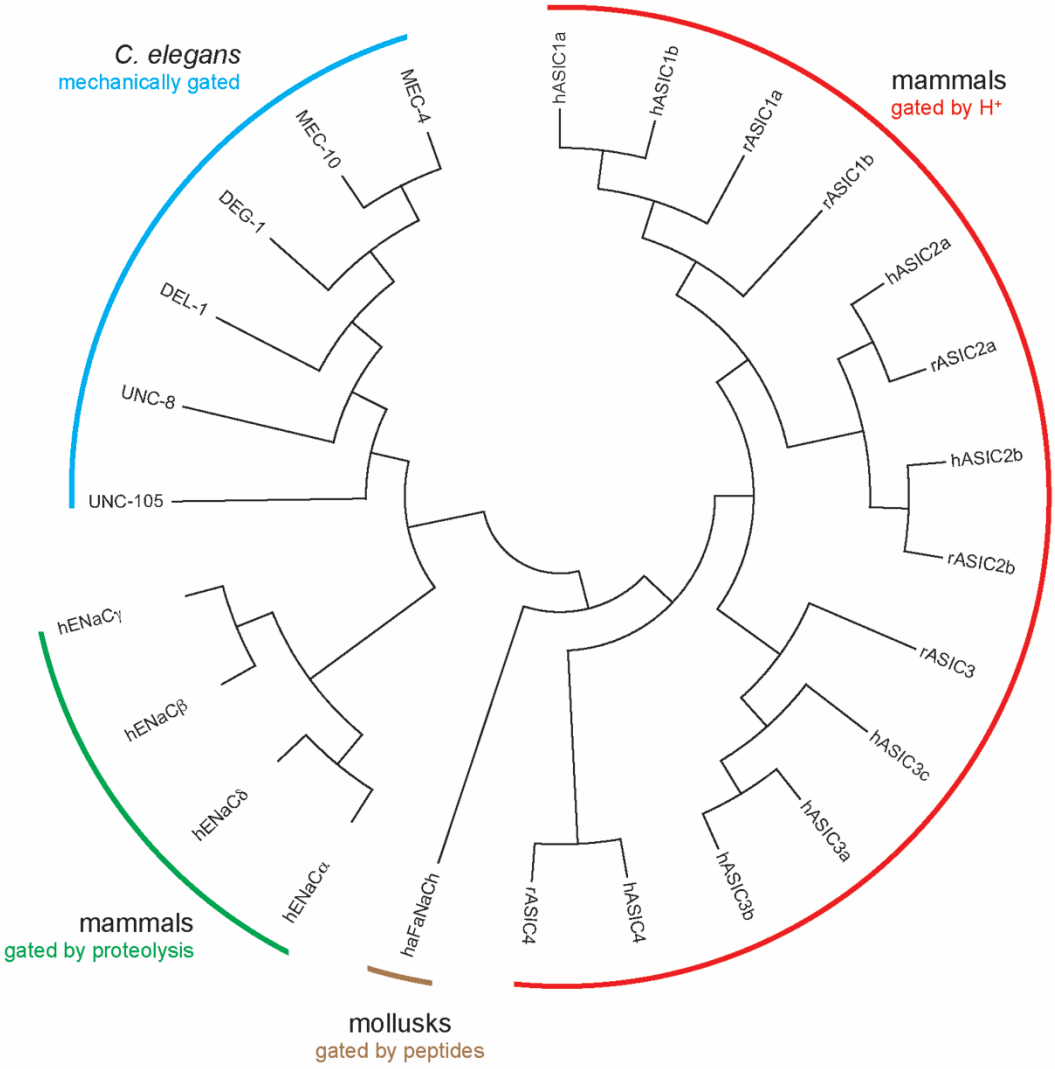

Figure 1.1. Phylogenic tree of the ENaC/DEG ion channels. Protein sequences were aligned using ClustalW. Species used for alignments include human (homo sapiens, h), rat (rattus norvegicus, r), snail (helix aspersa, ha) and nematode (caenorhabditis elegans).

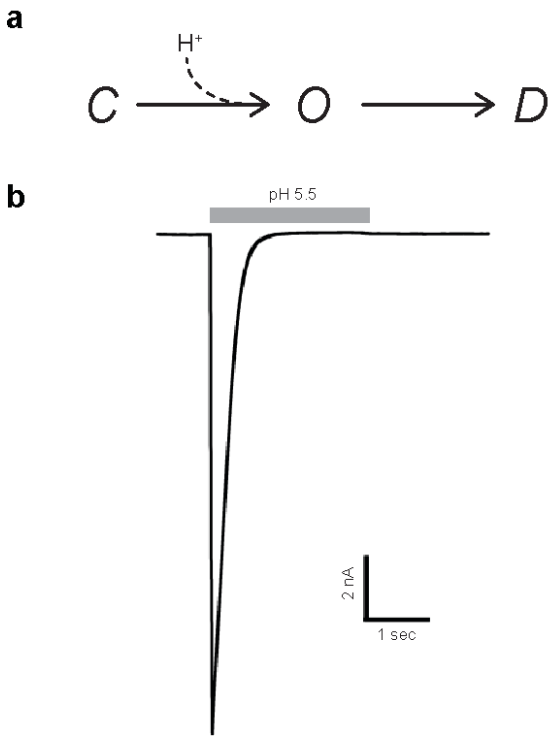

Figure 1.2. Proton-dependent gating scheme of ASICs. a, Linear model of a three-state proton-dependent gating scheme for ASICs. Modified from Zhang et al., 2006[54]. **b,** Whole-cell patch-clamp recording of a proton-gated current from chicken ASIC1a channels expressed in CHO-K1 cells.

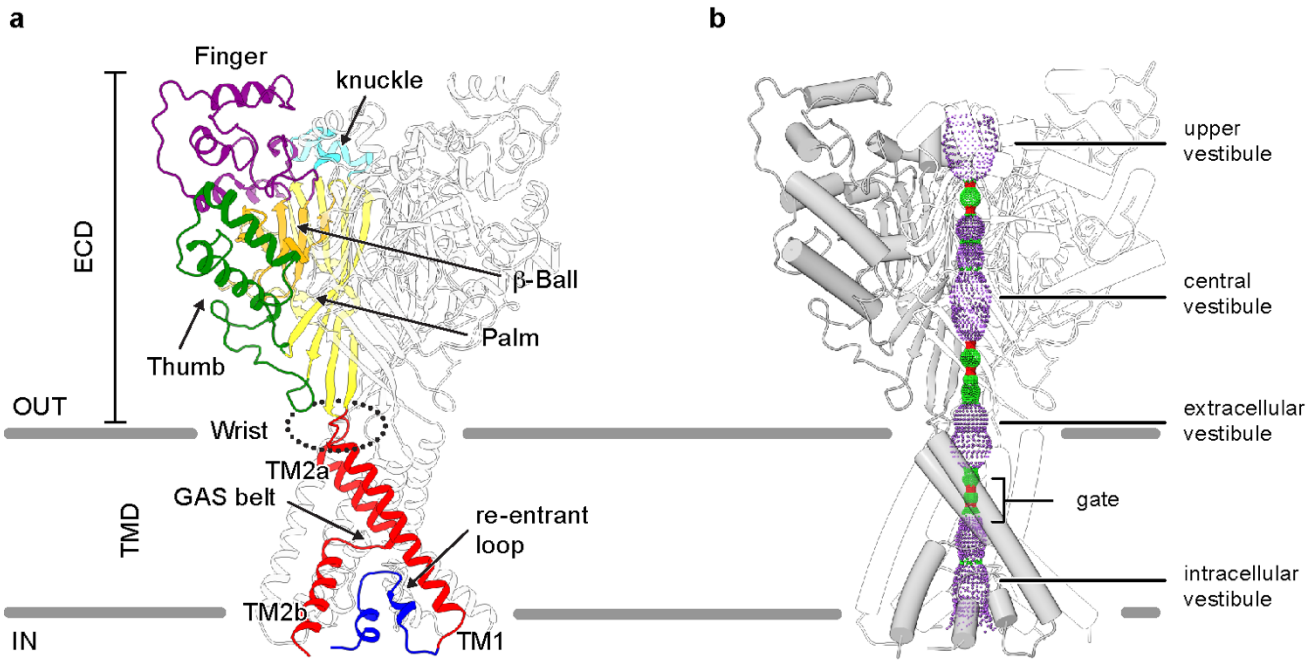

Figure 1.3. Architecture and pore profile of a desensitized ASIC1a channel. a, Cartoon representation of a desensitized ASIC1a channel with domains labeled and independently colored for a single subunit. **b,** Pore profile of an ASIC1a channel in a desensitized state at low pH. Pore radius calculated with HOLE software (pore radius: red < 1.15 Å < green < 2.3 Å < purple).

Chapter 2

Gating mechanisms of acid-sensing ion channels

The contents of chapter two are published in modified form:

Yoder, N., Yoshioka, C. and Gouaux, E. Gating mechanisms of acid-sensing ion channels. *Nature* 555, 387-401 (2018).

Author Contributions

N.Y. and E.G designed the project. N.Y. performed biochemistry, crystallography, and electrophysiology experiments. N.Y. and C.Y. performed cryo-EM data collection. C.Y. performed the cryo-EM data analysis. N.Y wrote the manuscript and all authors edited the manuscript.

Abstract

Acid sensing ion channels (ASICs) are trimeric[20], proton-gated[34,36] and sodium selective[126,127] members of the epithelial sodium channel/degenerin (ENaC/DEG) superfamily of ion channels[35,128] and are expressed throughout vertebrate central and peripheral nervous systems. ASIC gating occurs on a millisecond time scale[43] and can be largely described by a simple mechanism composed of three states: high pH resting, low pH open and low pH desensitized[54]. While previously solved x-ray structures of ASIC1a elucidated the conformations of the open[55] and desensitized[20,57] states, the structure of the high pH, resting state as well as detailed mechanisms for activation and desensitization have remained elusive. Here we present resting state structures of homotrimeric chicken ASIC1a at high pH determined by x-ray crystallography and single particle cryo-electron microscopy, informing a comprehensive molecular mechanism for proton-dependent gating in ASICs. In the resting state, the thumb domain has moved outward relative to its position in the open and desensitized states, expanding the 'acidic pocket'. Activation thus involves 'closure' of the thumb into the acidic pocket, expansion of the lower palm domain and an iris-like opening of the channel gate. Furthermore, we demonstrate how the β11-β12 linkers demarcating upper and lower palm domains serve as a molecular 'clutch', undergoing a simple rearrangement to permit rapid desensitization.

Materials and methods

Receptor construct, expression and purification: The Δ25 crystallization construct has 24 residues removed from the amino-terminus and 64 residues removed from the carboxy-terminus of the full-length chicken ASIC1a construct. Recombinant Δ25 protein was expressed in HEK293S GnTI$^-$ cells by way of baculovirus-mediated gene transduction. HEK293S GnTI$^-$ cells, in suspension culture, were grown to a density of 3.5 X 10^6 ml^{-1} and infected with P3 virus. After 8 hours of culture at 37°C, sodium butyrate was added to 10 mM final concentration and the temperature was shifted to 30°C. After 48 hours of expression, cells were collected by centrifugation, washed with phosphate buffered saline (PBS), and resuspended in Tris buffered saline containing protease inhibitors (TBS; 150 mM NaCl, 20 mM Tris pH 8.0, 1 mM phenylmethylsulfonyl fluoride, 0.05 mg ml^{-1} aprotinin, 2 μg ml^{-1} pepstatin A, and 2 μg ml^{-1} leupeptin). Cells were disrupted via sonication and membrane fractions were isolated by ultracentrifugation. cASIC1a channels were expressed in cell culture similar to the Δ25 construct yet without membrane fraction isolation.

Membrane pellets (Δ25) were resuspended in TBS buffer with protease inhibitors, homogenized, and solubilized in 40 mM *n*-dodecyl β-D-maltoside (DDM) for 1 hour at 4°C. cASIC1a channels were solubilized in an identical manner immediately after cell disruption via sonication. The solubilized material was clarified by ultracentrifugation and the supernatant was incubated in metal ion affinity resin for 1.5 hours at 4°C with 10 mM imidazole. Co^{2+} resin was packed into a column and subjected to three column volume wash steps with buffer containing 300 mM NaCl, 20 mM Tris pH 8.0, 1 mM DDM, and 10 mM imidazole followed by three additional column volume washes with buffer containing 300 mM NaCl, 20 mM Tris pH 8.0, 1 mM DDM, and 30 mM imidazole. Bound protein was eluted with 300 mM NaCl, 20 mM Tris

pH 8.0, 1 mM DDM, and 250 mM imidazole. Cleavage of the histidine-tagged enhanced green fluorescent protein (EGFP) tag was achieved by thrombin digestion. The Δ25 protein was further purified by size-exclusion chromatography (SEC) using a mobile phase containing 300 mM NaCl, 20 mM Tris pH 8.0, 2 mM *n*-decyl β-D-thiomaltopyranoside (C10ThioM), 1 mM dithiothreitol (DTT), 0.2 mM cholesteryl hemisuccinate (CHS) and 5 mM $CaCl_2$ or $BaCl_2$. Peak fractions were collected and concentrated to ~3 mg ml^{-1}.

Crystallization: Cholesterol stocks were maintained at 50 mg ml^{-1} in chloroform and stored at -20°C. Cholesterol aliquots were removed from stock and placed under argon until visibly dry. Dried cholesterol aliquots of 6 mg were resuspended by adding 20 µl of an aqueous solution of 400 mM C10ThioM, followed by gentle stirring for 1 hour at 4°C[129]. Subsequently, 110 µl of purified Δ25 protein at 3 mg ml^{-1} was added to the cholesterol/detergent mixture and incubated for 16 hours at 4°C with gentle stirring. The protein mixture was clarified by two ultracentrifugation steps and used immediately for crystallization experiments. For the Δ25-Ca^{2+} structure, the protein was incubated with cholesterol (6 mg) resuspended in 20 µl of an aqueous solution of 200 mM DDM.

Crystals were obtained at 4°C by way of the hanging drop vapor diffusion method. Reservoir solution contained 100 mM Tris pH 8.5-9.5, 150 mM NaCl, 5-20 mM $CaCl_2$ or $BaCl_2$, and 29-33% (v/v) PEG 400. Drops were composed of 1:1, 1.5:1, 1.75:1, and 2:1 protein to reservoir ratios, respectively. Crystals typically appeared within 2 weeks. Crystals were cryoprotected by increasing the PEG 400 concentration to 36% (v/v), in the protein-containing drop, before flash cooling in liquid nitrogen.

Structure Determination: X-ray diffraction data sets were collected at the Advanced Light Source (ALS) beamline 5.0.2 and at the Advanced Photon Source (APS) beamline 24ID-C and diffraction was measured to ~ 2.95 Å and ~ 3.2 Å for Δ25 with Ba^{2+}, and Ca^{2+}, respectively.

Diffraction data were indexed, integrated, and scaled using XDS and XSCALE[130] software. Diffraction data from Δ25-Ca^{2+} crystals was processed with the microdiffraction assembly method[131]. The Δ25-Ba^{2+} and Δ25-Ca^{2+} structures were solved by molecular replacement using the PHASER program[132]. For both structures, the extracellular domain coordinates of the ΔASIC1 structure (PDB 2QTS) were used as a search probe. All models were built via iterative rounds of manual model building in Coot[133] and refinement in Phenix[134] until satisfactory model statistics were achieved. Ramachandran statistics for both Δ25-Ba^{2+} and Δ25-Ca^{2+} structures were 98.31% favored and 1.69% allowed with none disallowed. 'Omit' maps were employed throughout the building and refinement process and to verify the presence of the GAS domain swap within the second transmembrane domain helix.

Sample preparation, data acquisition, image processing, and model building for cryo-EM: cASIC1a was purified as described for Δ25 with the mobile phase for SEC containing 150 mM NaCl, 20 mM Tris pH 8.0, 1 DDM, 1 mM DTT, 0.2 mM CHS and 5 mM $CaCl_2$. Peak fractions were concentrated to 3.2 mg ml^{-1} and 2.5 μl of cASIC1a sample was applied to a glow-discharged (15 mA for 60 s on carbon side) Quantifoil holey carbon grid (gold, 1.2 μm/1.3 μm hole size/hole space, 300 mesh), blotted for 3 s at 100% humidity with a Vitrobot Mark IV (FEI) and plunge frozen in liquid ethane cooled by liquid nitrogen.

Data were collected on a Titan Krios cryo-electron microscope (FEI) operating at 300 kV. Images were recorded on a Gatan K2 summit direct electron detector, positioned after an energy filter (20 eV slit width), in super resolution mode with a binned pixel size of 1.04 Å.

Images were collected using the automated image acquisition software SerialEM[135] and dose-fractionated to 100 frames at 0.1 s per frame with a total exposure time and dose of 10 s and 40-50 $e^-/Å^2$, respectively. Nominal defocus values ranged from -1 to -3 μm.

Images were motion corrected and summed with UCSF MotionCor2[136] and defocus values were estimated with Gctf[137]. ~ 256000 particles were picked using DoGPicker[138] and followed by reference-free 2D classification in Relion[139] to remove broken particles and aggregates. From 2D classification, ~ 160000 particles were subjected to 3D refinement and classification (C1 symmetry) in Relion to eliminate particles containing some degree of conformational heterogeneity. Inspection of the resulting 3D classes revealed four well-resolved classes containing a total of 33991 particles, which were subjected to further 3D refinement and classification in Relion (C3 symmetry). Finally, a single class containing 26117 particles was carried over for final refinement in cisTEM[140] with C3 symmetry imposed. Refinement in cisTEM was limited to a resolution of 4.5Å (>=0.9 of the FSC) to prevent overfitting. A mask was used in cisTEM that did not exclude the outlying mask areas, but did filter them to a resolution of 30 Å to reduce the influence of the micelle on alignment. The final resolution was estimated to be 3.7 Å based on FSC gold standard analysis in Relion. Local resolution was calculated using blocres from the Bsoft[141] package with a box size of 20 and a 0.5 FSC cutoff.

The Δ25-Ba^{2+} crystal structure was docked into the EM density map for the cASIC1a channel in Chimera[142] and served as a template for manual model building of the cASIC1a channel in Coot. Deteriorating density prevented unambiguous modeling of 103 residues corresponding to the channel's cytosolic domains, limiting extension of the model to 1 and 5 residues on the amino- and carboxy-termini, respectively. The final model contains residues 41-

464 of chicken ASIC1a and was subjected to real-space refinement in Phenix[143] and concluded with a CC of 0.867 for all atoms.

Patch clamp recordings: Whole-cell patch clamp recordings were carried out on CHO-K1 cells 1-2 days after transfection of plasmid DNA encoding cASIC1a and EGFP separated by an internal ribosome entry site. For characterization of Δ25 channels and all I-V experiments, whole-cell patch clamp recordings were carried out on Sf9 cells 36-48 hours after infection with Δ25-EGFP or cASIC1a-EGFP P1 BacMam virus[25]. For all electrophysiology experiments individual cells were only used once for recording, no repeated measurements were taken from the same cell. Pipettes were pulled and polished to 2-4 MΩ resistance and were filled with internal solution containing (in mM): 150 KCl, 2 $MgCl_2$, 5 EGTA, and 10 HEPES pH 7.35. Unless noted, external solution contained (in mM): 150 NaCl, 2 $MgCl_2$, 2 $CaCl_2$, 8 Tris, and 4 MES. Membrane voltage was clamped at -60 mV. The Axopatch 200B amplifier was used for data acquisition and pClamp 10 software was used for trace analysis.

Results

Structure of the high pH resting state

To form well-ordered crystals of an ASIC in a high pH resting state, we employed the Δ25 construct of chicken ASIC1a. This construct includes residues 25-463 of the full-length polypeptide and retains proton-dependent gating activity (**Figure 2.1a-b**). Crystals of the Δ25 construct belonging to the $P2_12_12_1$ space group were grown at high pH in the presence of inhibitory cations Ba^{2+} or Ca^{2+}[51] and diffract to 2.95 and 3.2 Å, respectively (**Table 2.1**).

The Δ25-Ba^{2+} and Δ25-Ca^{2+} structures are nearly identical, adhering to the canonical chalice-like architecture of open[55] and desensitized[20,57] channels. Individual subunits resemble a

clenched fist composed of TMD, palm, wrist, finger, knuckle, thumb, and β-ball domains[20] (**Figure 2.1c**). Relative to open[55] and desensitized[20,57] channels, the resting state structure shows that the thumb and finger domains adopt conformations farther from the molecular threefold axis, giving rise to an expanded extracellular domain (ECD) (**Figure 2.1d-e**) and exposing an additional ~ 595 $Å^2$ of solvent accessible surface area per subunit. The ion channel gate is closed and bears a striking resemblance to the TMD structure of the desensitized channel (**Figure 2.1e**), indicating that pore architecture is conserved across non-conducting functional states and suggesting that TMD conformation is not directly pH-dependent.

Though the Δ25 construct is gated by protons, truncation of the amino- and carboxy-termini reduces selectivity for Na^+ and decreases the Hill slope of proton-dependent ion channel activation (**Figure 2.2a-c**). Point mutations on TM2b, within the cytoplasmic region of the ion channel, also reduce sodium selectivity[125]. Given the altered function of the Δ25 construct and the importance of residues on or near the cytoplasmic domains of the ion channel, we determined the structure of the full-length chicken ASIC1a channel (cASIC1a) in a resting state at high pH and in the presence of Ca^{2+} to a nominal resolution of 3.7 Å by cryo-EM (**Figure 2.3a-d, Figure 2.4, Figure 2.5, Table 2.2**).

Despite their functional discrepancies, Δ25 and cASIC1a structures are almost identical at the present resolutions (**Figure 2.3e-g**). Moreover, the superior quality of the EM density map in regions of the channel that suffer from weak x-ray based electron density provides valuable and unbiased structural information for domains central to gating and ion permeation in ASIC1a, including the acidic pocket and the TMD (**Figure 2.3c-d**). Nevertheless, key features from the x-ray structure are conserved, including an expanded acidic pocket and closed gate (**Figure 2.3c-g**). Furthermore, in both x-ray and cryo-EM structures, TM2 helices undergo a domain swap

permitting the Gly-Ala-Ser motif[123,124,144] (GAS belt) to adopt an extended conformation immediately below the primary channel gate (**Figure 2.1**, **Figure 2.3**, **Figure 2.6**). Taken together, the conformation of the resting channel observed in our x-ray structures was not substantially affected by truncation of the cytoplasmic termini, model bias or crystal packing.

Mechanism for proton-dependent activation

ASIC1a channels populate a resting, closed state at physiological pH and activate within milliseconds in response to extracellular acidosis[47,145]. Consistent with its proposed role in proton-dependent gating[20,107], the acidic pocket, a solvent-exposed and electrostatically negative cavity formed at subunit interfaces, adopts an expanded conformation in both x-ray and cryo-EM resting state structures. We speculate that this conformation is stabilized by hydrophobic and polar contacts across finger, thumb and palm domains (**Figure 2.7a-b, Figure 2.8a-b**). Upon extracellular acidification, the thumb helices α4 and α5 shift towards the channel core as α5 undergoes a 12° lateral pivot about its amino-terminus, anchoring its carboxy-terminus against the palm domain of a neighboring subunit (**Figure 2.8c**). Rearrangements of thumb helices upon activation reduce the distance between titratable residues within the acidic pocket, permitting the formation of proton-mediated carboxyl-carboxylate pairings that stabilize the interface between thumb, finger and palm domains.

The collapse of the acidic pocket upon exposure to protons is transduced to the channel pore by way of the palm domain, a network of β-strands that comprise the core of the channel, link movements of the ECD to the pore domain and frame extracellular fenestrations that provide access for cations to the extracellular vestibule and pore mouth (**Figure 2.9**). Activation initiates rearrangements across the ECD that manifest as ~ 5° counterclockwise rotations of individual subunits around a lateral scaffold comprised of the β-ball and upper palm domains (**Figure 2.7c**).

The rotation of all subunits in concert leads to a flexing of the lower palm towards the plasma membrane, displacing β1 and β12 by ~ 4 Å and inducing a translation of TM1 and TM2a away from the molecular threefold axis (**Figure 2.7d**), culminating in the expansion of the extracellular fenestrations (**Figure 2.9**). The pore profile of the resting channel harbors a closed gate along the threefold axis composed of primary constrictions at Asp 433 and Gly 436 (**Figure 2.10a-b**). Proton-dependent rearrangements originating at the ECD facilitate channel activation via an iris-like opening of TM helices (**Figure 2.10c-d**), shifting the carboxyl groups of Asp 433 by 5.3 Å and rupturing the resting channel gate (**Figure 2.10e-f**).

To elucidate the contributions of acidic pocket collapse to pH-dependent gating, we utilized site-directed double cysteine substitutions with the goal of introducing a disulfide bridge at residues Thr 84 and Asn 357 to anchor the thumb domain to the palm domain of a neighboring subunit, arresting the acidic pocket in an expanded conformation. In whole-cell patch clamp experiments, reducing conditions recovered proton-dependent gating behavior, increasing the magnitude of proton-dependent currents when compared to ambient conditions (**Figure 2.7e-f**). The observation that ASIC1a activation is blocked by an inter-subunit disulfide bond at the acidic pocket supports a previously proposed functional role for subunit-subunit interactions in ASIC1a channels[146], underscores the critical nature of the acidic pocket to ASIC1a gating and supports a simple gating scheme wherein pH-dependent contraction of the acidic pocket drives channel activation.

A molecular 'clutch' at β11-β12 linkers controls desensitization

ASIC1a channels undergo nearly complete desensitization over hundreds of milliseconds[47,145]. Situated at the border of the upper and lower palm domains, the β1-β2 and β11-β12 linkers are important determinants of gating kinetics in ASIC channels[111,112,119,147,148].

The overall conformation of the β1-β2 and β11-β12 linkers in the resting state mimics that of the open channel (**Figure 2.11a-b**). In contrast to the similarities between resting and open states at β11-β12 linkers, however, the side chains of Leu 414 and Asn 415 'swap' positions in the desensitized channel, resulting in a 9 Å reorientation of Leu 414 towards the central vestibule and inducing a striking rearrangement of β11-β12 linkers (**Figure 2.11c**)[56]. We therefore propose that the conformation of β11-β12 linkers adopted in the resting state provides a structural link between upper and lower channel domains, enabling pH-dependent collapse of the acidic pocket, which occurs ~ 40 Å away from the plasma membrane, to drive activation. Furthermore, we speculate that rearrangement of the β11-β12 linkers enables desensitization during prolonged exposure to low pH by serving as a molecular clutch, decoupling the collapsed acidic pocket from the lower channel and allowing TM1 and TM2a to relax by 6 Å and 5 Å, respectively (**Figure 2.11d**), permitting the re-formation of the non-conducting ion channel. Accordingly, desensitization produces a "conformationally chimeric channel" bearing striking resemblance to the resting channel below the β11-β12 linkers (**Figure 2.1d**), and to the open channel above. Upon return to physiological pH, expansion of the acidic pocket initiates the return of β11-β12 linkers to their original conformation, reforming a resting channel primed for subsequent activation.

To explore the contribution of the β11-β12 linker rearrangement to desensitization in ASIC1a channels, we utilized site-directed double cysteine substitution to anchor Leu 414 to an adjacent residue on β1-β2 via a putative engineered disulfide bridge. Exposure to protons elicited an inward current from L86C/L414C channels that displayed an initial slow desensitizing component and gave way to a sustained current despite continued exposure to protons (**Figure 2.11e**). Taken together, our data are consistent with Leu 414 and β11-β12 linkers separating from

the neighboring β1-β2 linkers upon continued exposure to protons, and with this region playing a central role in the mechanism of desensitization.

Discussion

Here we present x-ray and cryo-EM structures of ASIC1a channels in a resting state at high pH and in the presence of inhibitory cations Ba^{2+} or Ca^{2+}. The structure of a resting channel, the last remaining unsolved functional state of ASIC1a, unites our molecular understanding of the canonical functional states of ASIC1a channels and informs a comprehensive molecular model for pH-dependent gating mechanics (**Figure 2.12**). Moreover, in concert with the structure of the full-length cASIC1a in a resting state, our data suggest the TM2 domain swap and GAS belt as functional characteristics of ASIC1a architecture.

At physiological pH, ASIC1a channels largely populate a resting state with a pore closed to ion permeation and an expanded acidic pocket. Upon exposure to low pH, the acidic pocket adopts a collapsed conformation as α5 pivots towards the channel core to enable proton-mediated carboxyl-carboxylate pairings between thumb and finger domains. The collapse of the acidic pocket initiates coordinated movements throughout the ECD that manifest as lateral rotations of individual subunits around their upper palm domain scaffold. Rotation of all subunits in concert displaces the β1 and β12 strands of the lower palm domain towards the membrane and away from the molecular threefold axis. This shift of the lower palm domain results in an expansion of the extracellular fenestrations and an iris-like opening of the channel gate, expanding the GAS belt and allowing ions to pass through the channel pore.

ASIC1a channels undergo rapid and complete desensitization at low pH. Continued exposure to protons results in a swap in sidechain orientation for Leu 414 and Asn 415 residues, inducing a substantial rearrangement of the β11-β12 linkers demarcating upper and lower palm

domains. Reorganization of palm domain linkers uncouples the low pH conformation of the upper ECD from the lower channel, allowing TM helices to relax back into a resting-like conformation and forming a desensitized channel insensitive to protons. Re-priming ASIC1a channels for activation requires the removal of protons. We hypothesize that, upon return to physiological pH values, electrostatic repulsion stemming from the deprotonation of titratable acidic residues drives the expansion of the acidic pocket, permitting β11-β12 to revert back to a non-swapped conformation and recovering proton sensitivity upon formation of a resting channel.

Our results augment previous studies of gating mechanics in ASICs that suggest activation-induced movements at the acidic pocket as well as roles for the lower palm domain and β11-β12 linkers in desensitization[110,149,150]. By contrast, atomic force microscopy studies[151] indicate that human ASIC1a channels undergo a height increase of the ECD upon activation, a conformational change that has so far not been observed by analysis of x-ray crystallographic and cryo-EM structures of chicken ASIC1a. Nevertheless, the high cooperativity by which protons activate cASIC1a is consistent with multiple resting states characterized by varying degrees of protonation, suggesting that our current experimental structures represent an average over an ensemble of protein conformations. As ASICs are structurally the most well characterized members of the ENaC/DEG superfamily of ion channels, our studies provide fundamental insights into the mechanisms of gating and modulation of the entire superfamily.

Acknowledgements

We thank A. Goehring, D. Claxton and I. Baconguis for initial construct screening and advice through all aspects of the project, L. Vaskalis for help with figures, H. Owen for manuscript

preparation and all Gouaux lab members for their support. We acknowledge the Berkeley Center for Structural Biology and the Northeastern Collaborative Access Team for help with x-ray data collection. This research was supported by the National Institute of Diabetes and Digestive Kidney Diseases (5T32DK007680), and the National Institute of Neurological Disorders and Stroke (5F31NS096782 to N.Y. and 5R01NS038631 to E.G.). Additional support was provided by ARCS Foundation and Tartar Trust fellowships. E.G. is an Investigator with the Howard Hughes Medical Institute.

Tables

	Δ25-Ba^{2+} Resting†	Δ25-Ca^{2+} Resting‡
Data collection		
Space group	$P2_12_12_1$	$P2_12_12_1$
Cell dimensions		
a, *b*, *c* (Å)	109.9, 130.4, 157.9	109.2 133.7 157.7
α, β, γ (°)	90.0, 90.0, 90.0	90.0, 90.0, 90.0
Resolution (Å)	50 - 2.95	100 - 3.20
R_{meas} (%)*	12.4 (549.8)	13.1 (58.1)
$I / \sigma I$*	15.39 (0.74)	7.05 (2.06)
Completeness (%)*	100 (100)	97.5 (99.1)
Redundancy	20.6	5.76
Refinement		
Resolution (Å)	25 - 2.95	25 - 3.2
No. reflections	48366	37646
R_{work} / R_{free}	0.226/0.258	0.287/0.297
No. atoms		
Protein	9247	9263
Ligand/ion	88	120
Water	0	0
B-factors		
Protein	145.62	157.29
Ligand/ion	194.47	187.53
Water	n/a	n/a
R.m.s. deviations		
Bond lengths (Å)	0.004	0.003
Bond angles (°)	0.701	0.688

Table 2.1. Crystallographic data collection and refinement statistics.

*Highest resolution shell in parentheses.

† Two crystals were merged for the Δ25-Ba^{2+} resting state structure

‡ Two crystals were merged for the Δ25-Ca^{2+} resting state structure and processed with microdiffraction assembly

5% of reflections were used for calculation of R_{free}.

	ASIC1a (EMDB-7009) (PDB-6AVE)
Data collection and processing	
Magnification	135000
Voltage (kV)	300
Electron exposure (e–/Å^2)	40 - 50
Defocus range (μm)	-1 to -3
Pixel size (Å)	1.04
Symmetry imposed	C3
Initial particle images (no.)	~ 256000
Final particle images (no.)	26117
Map resolution (Å)	3.7
FSC threshold	0.143
Map resolution range (Å)	3.2 - 4.8
Refinement	
Initial model used (PDB code)	5WKU
Model resolution (Å)	4.1
FSC threshold	0.5
Model resolution range (Å)	
Map sharpening *B* factor (Å^2)	-100
Model composition	
Non-hydrogen atoms	9657
Protein residues	423
Ligands	6
B factors (Å^2)	
Protein	100
Ligand	100
R.m.s. deviations	
Bond lengths (Å)	0.008
Bond angles (°)	0.946
Validation	
MolProbity score	1.75
Clashscore	6.0
Poor rotamers (%)	0.0
Ramachandran plot	
Favored (%)	95.02
Allowed (%)	4.98
Disallowed (%)	0.0

Table 2.2. Cryo-EM data collection, refinement and validation statistics.

Figures and Legends

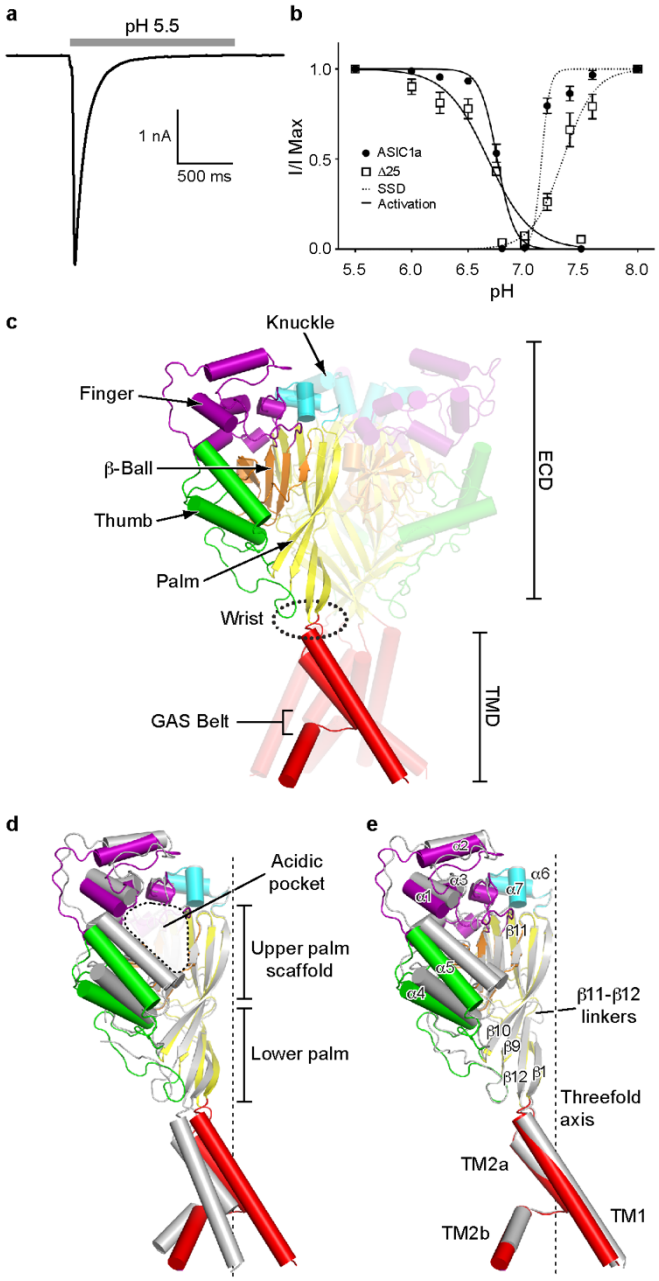

Figure 2.1. Architecture and function of a resting channel. Figure 2.1. Architecture and function of a resting channel. **a-b,** Functional characterization of the Δ25 construct. Representative whole-cell patch clamp recording (**a**) from Δ25 channels activated by step to low pH and dose-response and steady-state desensitization (SSD) curves (**b**) for Δ25 and cASIC1a channels. Data were collected from Sf9 cells infected with Δ25 or cASIC1a BacMam virus. Error

bars represent SEM and the center represents the mean, n = 7 (activation) or 5 (SSD) cells for cASIC1a and 10 (activation) or 7 (SSD) cells for Δ25. Experiments were replicated 7 (activation) or 5 (SSD) times for cASIC1a and 10 (activation) or 7 (SSD) times for Δ25 with similar results. **c,** Structure of a Δ25 channel in a resting state at high pH, colored by domain. **d-e,** Single subunit superposition of resting channels with open (**d**) (PDB 4NTW, grey) and desensitized (**e**) (PDB 4NYK, grey) channels.

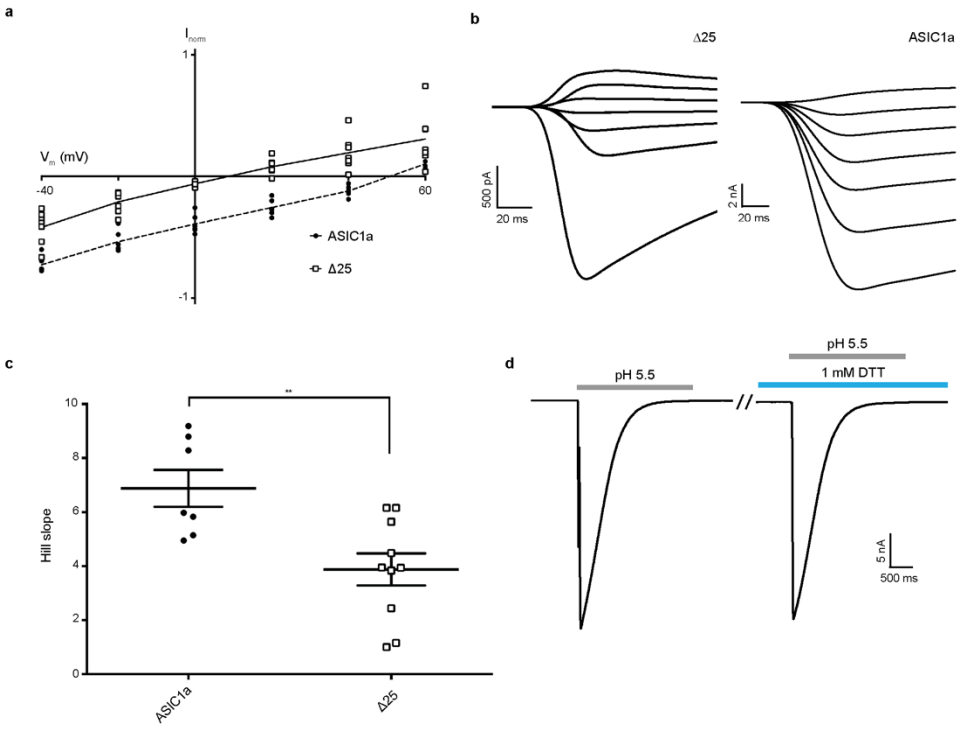

Figure 2.2. Function of ASIC1a constructs. a, I-V relationship for cASIC1a and Δ25 constructs between -40 and 60 mV. Individual data points are displayed and were normalized to current amplitudes at -60 mV, lines represent mean, n = 7 cells for Δ25 and 6 cells for cASIC1a, experiments were replicated 7 times for Δ25 and 6 times for cASIC1a with similar results. **b,** Representative whole-cell patch clamp recordings at stepped potentials from -60 mV to +60 mV for Δ25 and cASIC1a, experiments were replicated 7 times for Δ25 and 6 times for cASIC1a with similar results. **c,** Unpaired t-test results (two-sided) comparing hill slopes of activation for Δ25 and cASIC1a channels. Error bars represent SEM and the center represents the mean, ** indicates $p \leq 0.01$, $p = 0.0054$ and 95% confidence interval = -4.949 to -1.053, n = 7 for cASIC1a and 10 for Δ25, experiments were replicated 7 times for cASIC1a and 10 times for Δ25 with similar results. **d,** Control experiment demonstrating cASIC1a currents evoked by step to low pH under reducing or ambient conditions, experiments were replicated 7 times with similar results. Data were collected from Sf9 cells infected with Δ25 or cASIC1a BacMam virus.

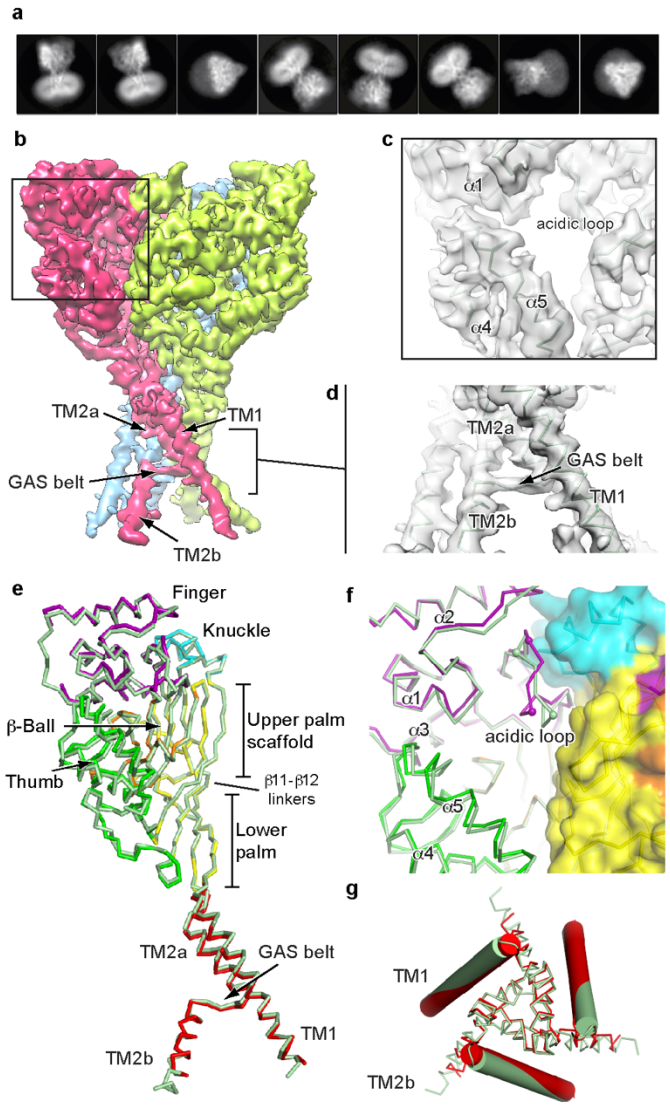

Figure 2.3. Cryo-EM structure of cASIC1a. a-d, Selected 2D classes (**a**) and cryo-EM density map (**b**) for cASIC1a with detail views of model and map for the acidic pocket (**c**) and TM2 domain swap **(d)**. **e,** single subunit superposition of Δ25 (grey) and cASIC1a channels. **f,** View of the acidic pocket from superposed Δ25 (grey) and cASIC1a channels, Gly 235 and Asp 238 α-carbon atoms are offset by ~ 3 Å and are shown as spheres. **g**, Top-down view of the TMD from superposed Δ25 (grey) and cASIC1a channels.

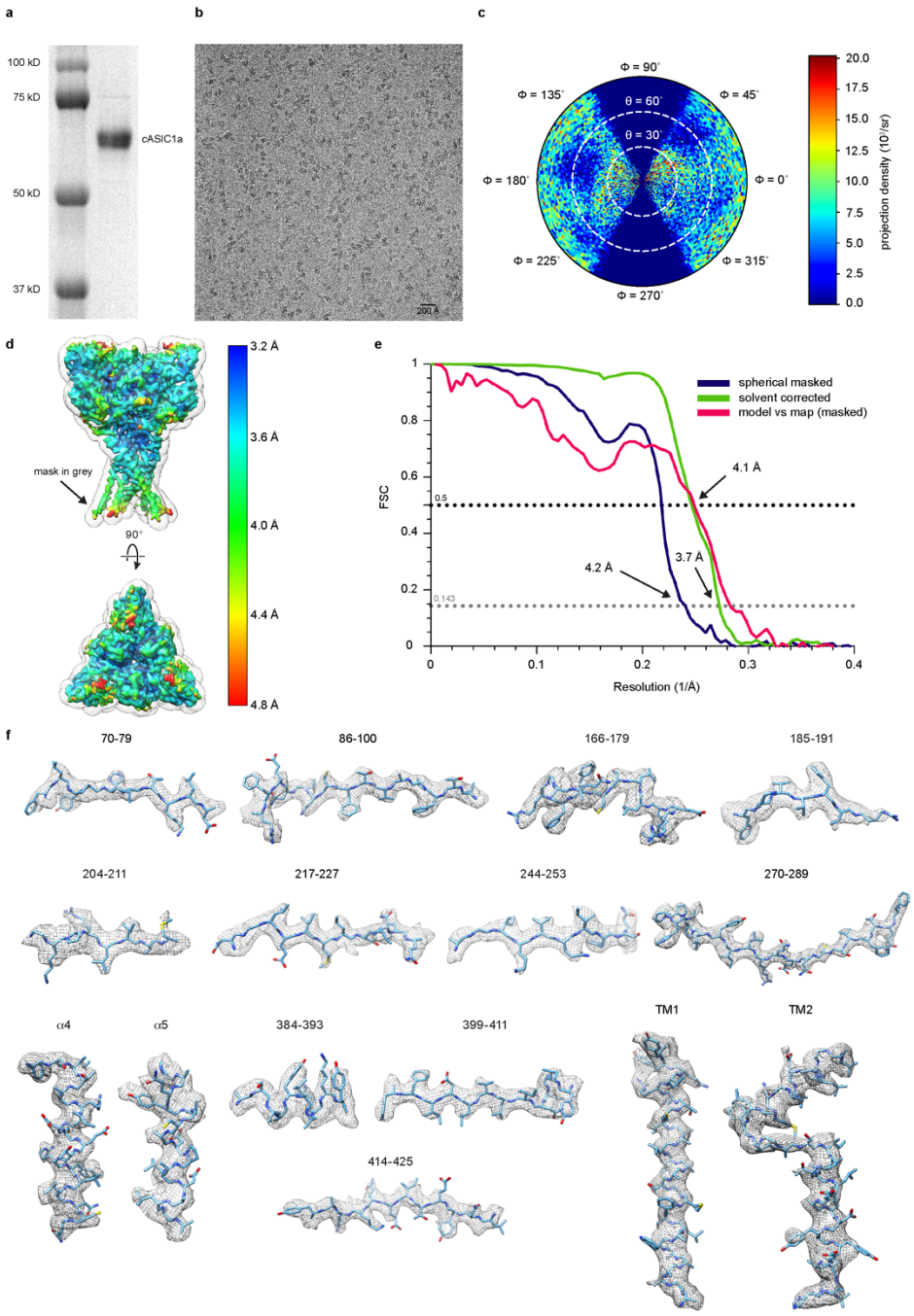

Figure 2.4. Single particle cryo-EM of cASIC1a. a, SDS-PAGE gel of purified cASIC1a. **b,** Representative micrograph of cASIC1a channels embedded in vitreous ice. **c,** Angular distribution of particle projections, sphere size proportional to number of particles. **d,** Density map colored according to local resolution. **e,** Spherical masked and solvent corrected FSC curves

for density maps and for the refined model to the final 3D reconstruction. **f,** Representative density for the cASIC1a reconstruction, identified by residue range or domain above.

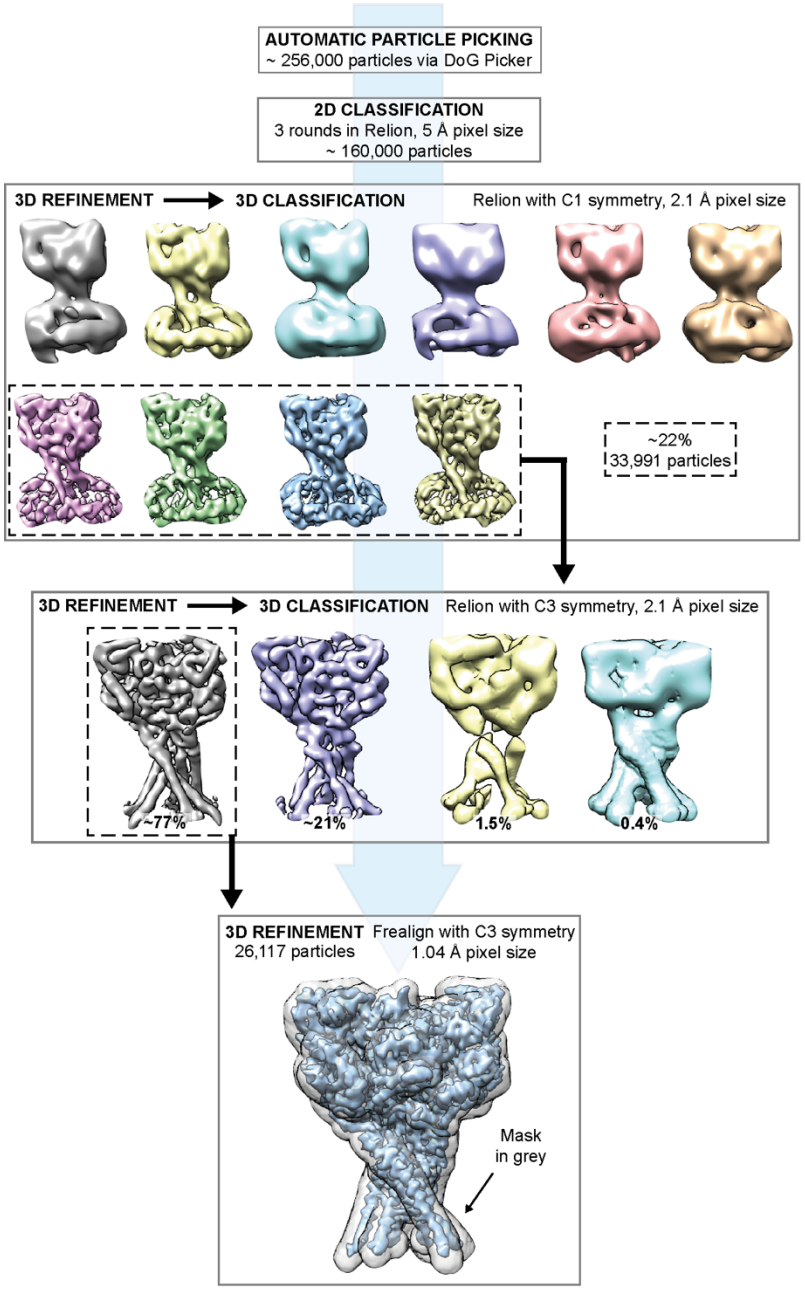

Figure 2.5. Cryo-EM data processing workflow. Representative data processing steps for the cASIC1a reconstruction.

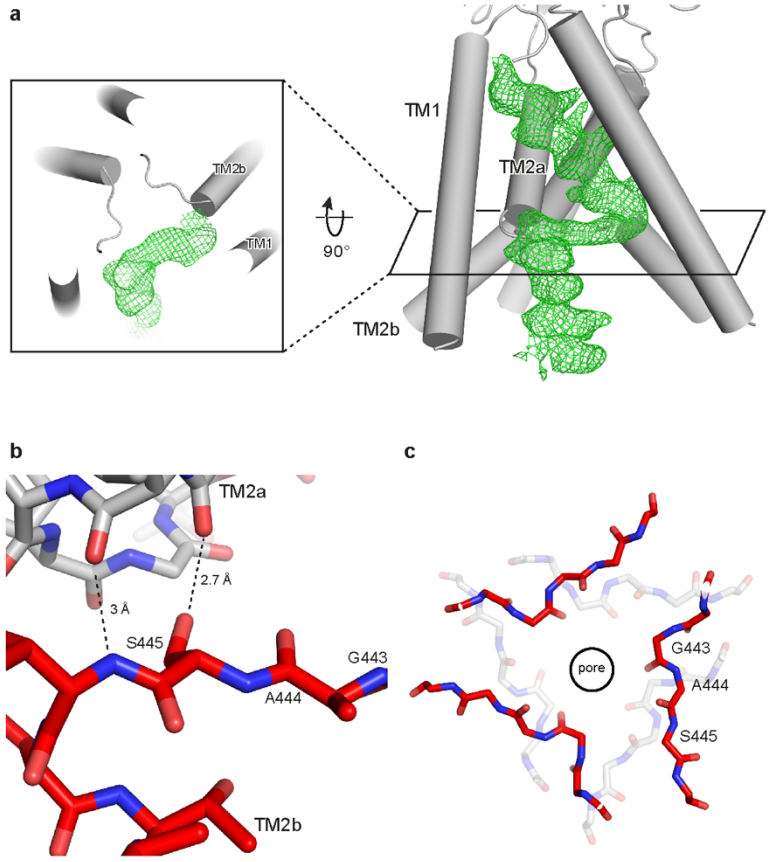

Figure 2.6. GAS domain swap. a, Omit map Fo-Fc density contoured at 2σ for a domain-swapped TM2, top view shown in inset. **b,** Discontinuous TM2 helix stabilized by hydrogen bonds. **c,** Superposition of resting and open (PDB 4NTW, grey) channels demonstrates relative conformations of the GAS belt.

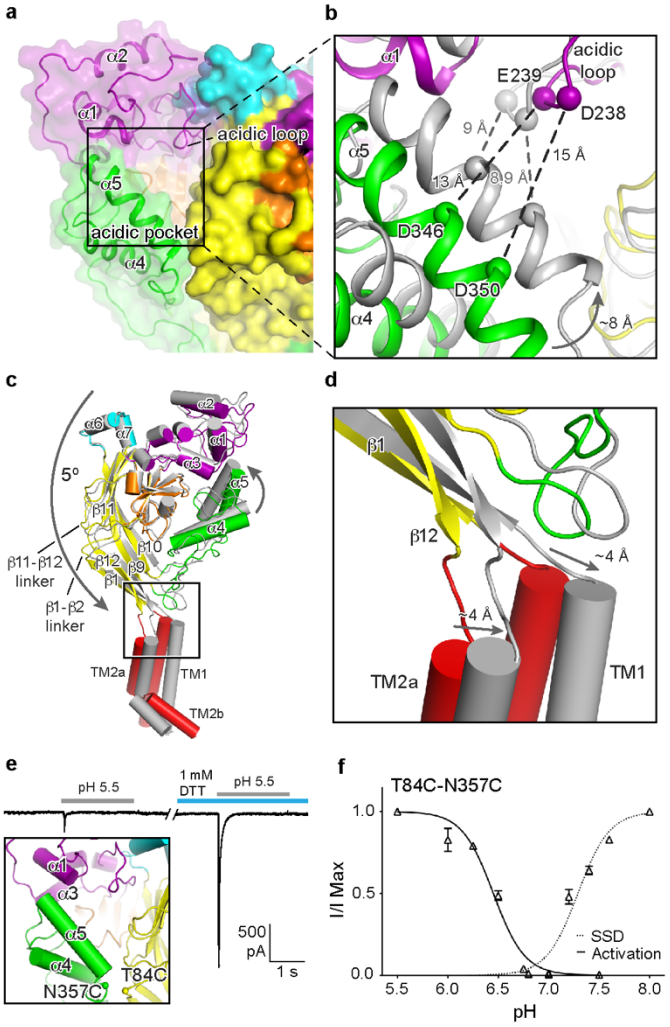

Figure 2.7. Acidic pocket collapse initiates channel activation. a-b, Resting channel acidic pocket (**a**) and superposition (**b**) with open channel (PDB 4NTW, grey). **c-d,** Single subunit superposition of resting and open channels demonstrates global (**c**) and lower palm domain (**d**) conformational changes associated with channel activation. **e,** Whole-cell patch clamp recording from T84C/N357C mutant channels, data were recorded from CHO-K1 cells transfected with cDNA for the T84C/N357C mutant channel or Sf9 cells infected with T84C/N357C BacMam virus, experiments were repeated 11 times with similar results. Schematic representation of site-directed cysteine substitutions shown in inset. **f,** Dose-response and SSD curves for T84C/N357C or cASIC1a channels. Data were collected from Sf9 cells infected with

T84C/N357C or cASIC1a BacMam virus. For T84C/N357C channels, recordings were conducted in 1 mM DTT. Error bars represent SEM and the center represents the mean, n = 7 (activation) or 5 (SSD) cells for cASIC1a and 7 (activation) or 6 (SSD) cells for T84C/N357C. Experiments were replicated 7 (activation) or 5 (SSD) times for cASIC1a and 7 (activation) or 6 (SSD) times for Δ25 with similar results.

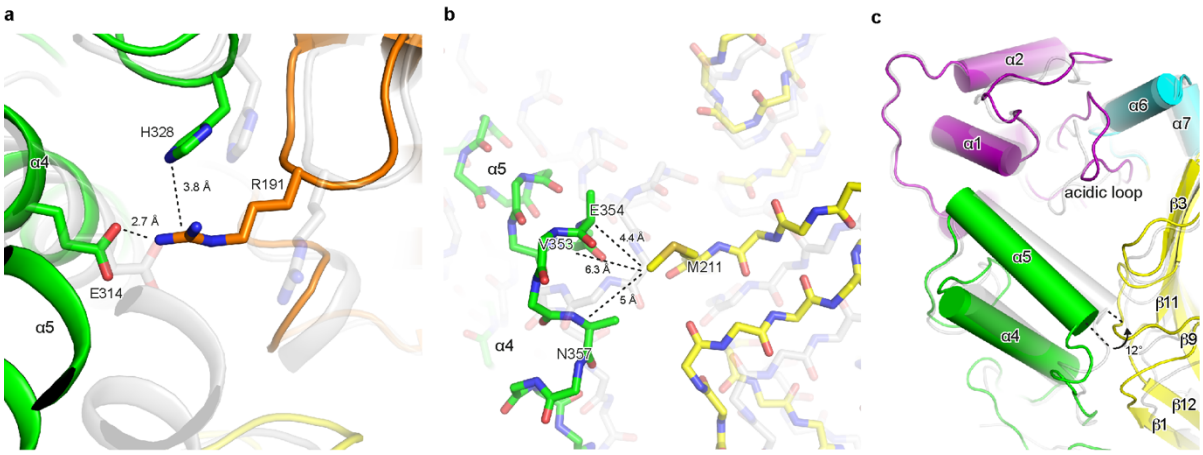

Figure 2.8. Conformational changes at the acidic pocket. a-b, Superposition of resting and open (PDB 4NTW, grey) channels highlight interactions between Arg 191, Glu 314, and His 328 (**a**), as well as between Val 353, Glu 354 and Asn 357 with Met 211 on an adjacent subunit (**b**) that stabilize the expanded, high pH conformation of the acidic pocket. **c,** Local superposition (α1 and α2) of resting and open channels demonstrates α5 pivot upon activation.

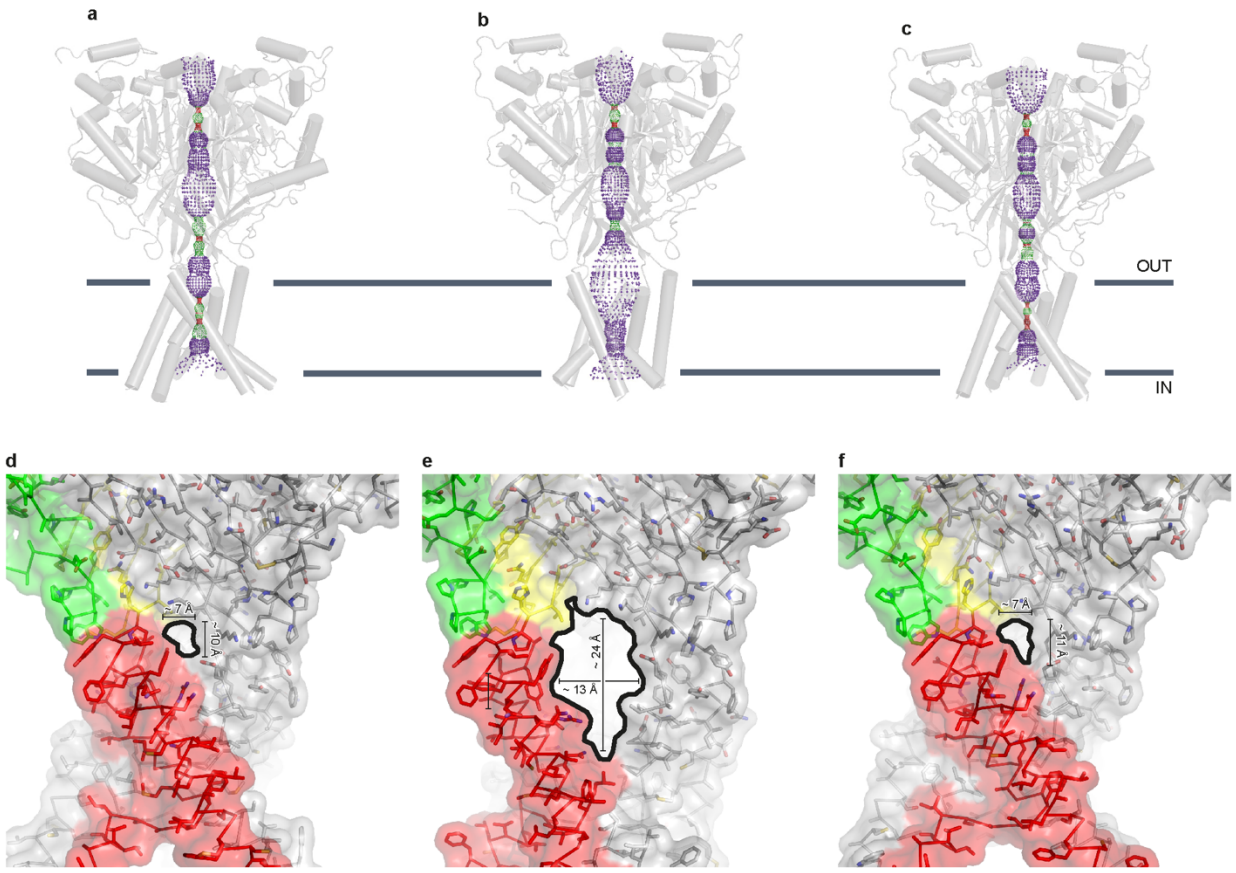

Figure 2.9. State dependence of extracellular fenestrations. a-c, Resting (**a**), open (**b**) (PDB 4NTW), and desensitized (**c**) (PDB 4NYK) channel pore profiles calculated with HOLE software (pore radius: red < 1.15 Å < green < 2.3 Å < purple). **a-c,** Approximate fenestration sizes for resting (**d**), open (**e**), and desensitized (**f**) channels, Approximate fenestration edge outlined with a solid black line.

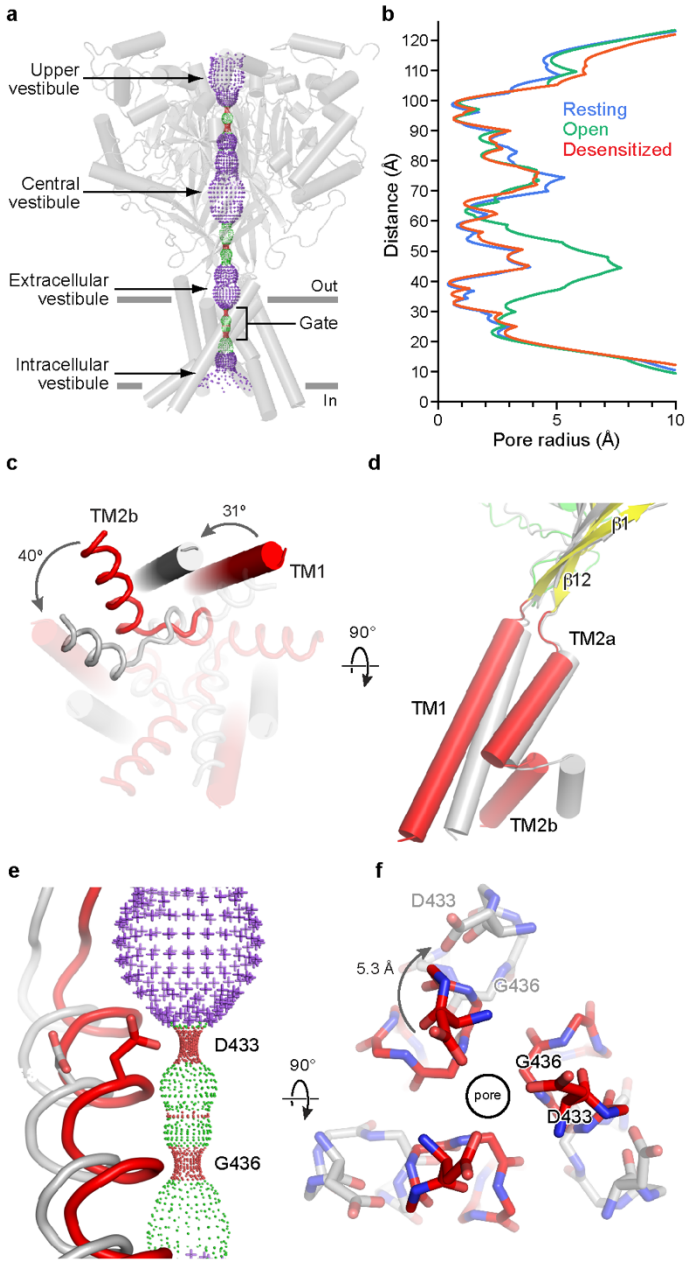

Figure 2.10. State dependent pore conformation. a, Resting channel pore profile calculated with HOLE software (pore radius: red < 1.15 Å < green < 2.3 Å < purple). **b,** Plot of pore radius for resting, open (PDB 4NTW) and desensitized (PDB 4NYK) channels along the molecular threefold axis. **c-d,** Conformation of resting and open TMDs viewed from below (**c**) and the side (**d**). **e-f,** Resting and open gates viewed from the side (**e**) and above (**f**).

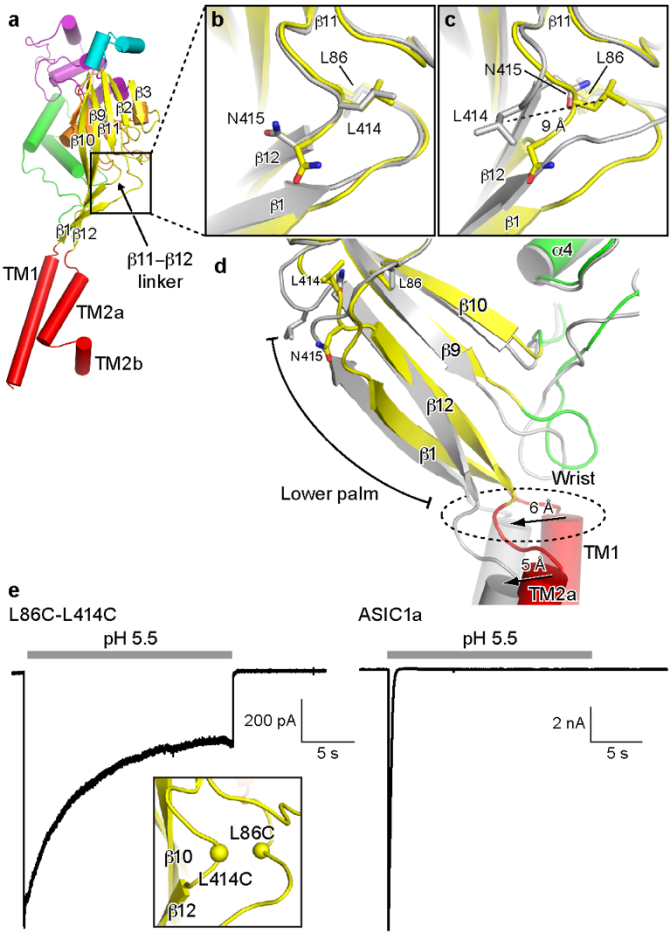

Figure 2.11. A molecular 'clutch' at β11-β12 linkers controls desensitization. a, Individual subunit of an open ASIC1a channel (PDB 4NTW). **b-c,** local alignments of an open channel with resting (**b**) and desensitized (**c**) (PDB 4NYK) channels (both in grey) demonstrate conformational rearrangements associated with desensitization. **d,** Comparison of lower palm and TMDs for open and desensitized (grey) channels. **e,** whole-cell patch clamp recordings from L86C/L414C and cASIC1a channels. Schematic representation of site-directed cysteine substitutions shown in inset. Data were collected from adherent CHO-K1 cells transfected with cDNA for mutant and cASIC1a channels, experiments were replicated 4 times with similar results.

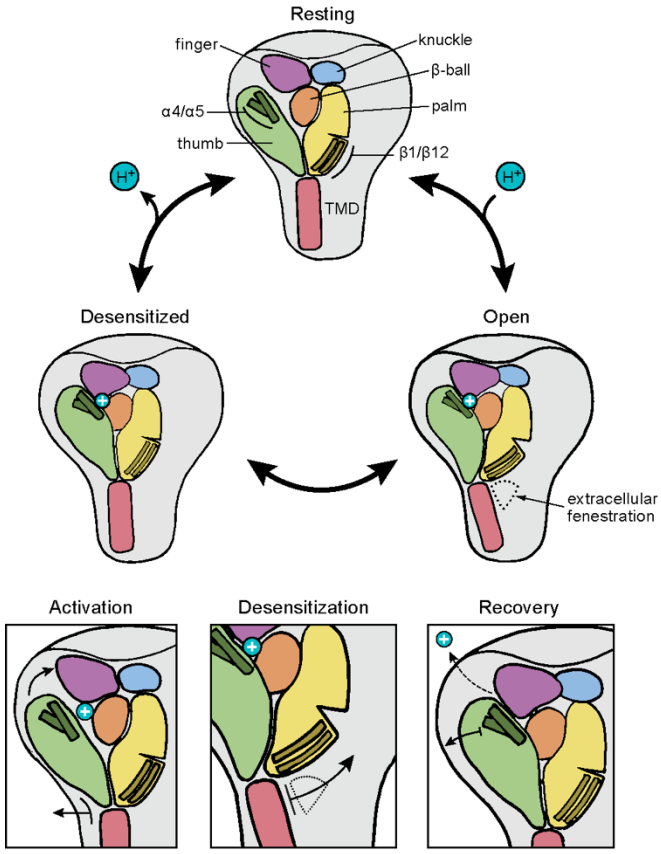

Figure 2.12. Gating scheme. Cartoon representation of proton-dependent gating cycle in ASIC1a channels.

Chapter 3

Divalent cation and chloride ion sites of chicken acid-sensing ion channel 1a elucidated by x-ray crystallography

The contents of chapter three are published in modified form:

Yoder, N. and Gouaux, E. Divalent cation and chloride ion sites of chicken acid sensing ion channel 1a elucidated by x-ray crystallography. *Plos One* 13, (2018)

Author Contributions

N.Y. and E.G designed the project. N.Y. performed biochemistry, crystallography, and electrophysiology experiments. N.Y wrote the manuscript and all authors edited the manuscript.

Abstract

Acid sensing ion channels (ASICs) are proton-gated ion channels that are members of the degenerin/epithelial sodium channel superfamily and are expressed throughout central and peripheral nervous systems. ASICs have been implicated in multiple physiological processes and are subject to numerous forms of endogenous and exogenous regulation that include modulation by Ca^{2+} and Cl^- ions. However, the mapping of ion binding sites as well as a structure-based understanding of the mechanisms underlying ionic modulation of ASICs have remained elusive. Here we present ion binding sites of chicken ASIC1a in resting and desensitized states at high and low pH, respectively, determined by anomalous diffraction x-ray crystallography. The acidic pocket serves as a nexus for divalent cation binding at both low and high pH, while we observe divalent cation binding within the central vestibule on the resting channel at high pH only. Moreover, neutralization of residues positioned to coordinate divalent cations via individual and combined Glu to Gln substitutions reduced, but did not extinguish, modulation of proton-dependent gating by Ca^{2+}. Additionally, we demonstrate that anion binding at the canonical thumb domain site is state-dependent and present a previously undetected anion site at the mouth of the extracellular fenestrations on the resting channel. Our results map anion and cation sites on ASICs across multiple functional states, informing possible mechanisms of modulation and providing a blueprint for the design of therapeutics targeting ASICs.

Introduction

Acid sensing ion channels (ASICs) are voltage-insensitive and proton-gated[36] members of the epithelial sodium channel/degenerin (ENaC/DEG) superfamily of ion channels[35,128] that assemble as homo- or heterotrimeric sodium-selective ion channels[20] and are expressed throughout vertebrate central and peripheral nervous systems. ASICs exhibit a simple three-state gating scheme, populating a non-conducting resting state at high pH, opening upon exposure to protons and quickly desensitizing[54], recovering proton-sensitivity only upon return to high pH. ASICs gate rapidly, fully activating in milliseconds and undergoing complete desensitization in hundreds of milliseconds[47,145]. The homotrimeric splice variant ASIC1a is highly enriched in the central nervous system (CNS) and participates in numerous physiological processes including learning and memory[76] and nociception[39]. Furthermore, ASIC1a is moderately permeable to Ca^{2+} and has been implicated in various forms of acidosis-induced neuronal injury and neurological disorders[87,88].

ASIC1a activity is modulated by endogenous divalent cations including Zn^{2+}, Mg^{2+}, and Ca^{2+}[51,52,54,59] and the modification of ASIC1a gating by extracellular Ca^{2+} has been an area of active investigation. Previous studies of homotrimeric ASIC1a and ASIC3 channels have proposed both allosteric[54] and pore blockade[52,53,152] mechanisms and suggested correspondingly distinct binding sites [52]. Furthermore, residues corresponding to Glu 426 and Asp 433 of cASIC1a are located at the mouth of the extracellular fenestration and within the pore, respectively, and are critical to Ca^{2+}-dependent block[52]. However, ambiguous results and a lack of defined Ca^{2+} binding sites have fallen short of a comprehensive mechanism for gating modification of ASIC1a channels by Ca^{2+}.

Extracellular Cl^- ions modulate a variety of ASIC1a characteristics including proton-dependent gating, desensitization kinetics and tachyphylaxis[153]. In x-ray structures of ASIC1a channels in open and desensitized states, a bound Cl^- is buried within the thumb domain near helices α4 and α5[20,55,57]. At low pH, Cl^- ions are positioned at a subunit-subunit interface coordinated by Arg and Glu residues on α4 of the thumb domain and by a Lys residue on the palm domain of a neighboring subunit. Residues involved in Cl^- binding are highly conserved amongst ASICs, and modulation by extracellular Cl^- has also been observed in ENaC channels at a likely similar inter-subunit binding site[154,155], demonstrating the importance of extracellular Cl^- to the ENaC/DEG superfamily of ion channels.

Here, we determine binding sites for anions and divalent cations on resting and desensitized ASIC1a channels at high and low pH, respectively. Our results map a complex network of divalent cation sites on ASICs within domains closely involved in proton-dependent gating and demonstrate state-dependence for both anion and cation binding. These data present a structural framework for understanding the interplay between gating and ion binding in ASICs and provide a template for the development of ASIC1a-specific modulatory agents.

Materials and methods

Receptor construct, expression and purification: The Δ25 and Δ13 crystallization constructs have 24 or 13 residues removed from the amino-terminus, respectively, and 64 residues removed from the carboxy-terminus[55,56,156] of the full-length chicken ASIC1a construct. Recombinant protein was expressed in HEK293S GnTI$^-$ cells[157] as previously described[156]. In brief, HEK293S GnTI$^-$ cells grown in suspension were infected with BacMam virus[25] and collected by centrifugation after 48 hours of culture. Cell pellets were resuspended in tris buffered saline

(TBS; 150 mM NaCl, 20 mM Tris pH 8.0, 1 mM phenylmethylsulfonyl fluoride, 0.05 mg ml^{-1} aprotinin, 2 μg ml^{-1} pepstatin A, and 2 μg ml^{-1} leupeptin), disrupted by sonication, and membrane fractions were isolated by ultracentrifugation.

Membrane pellets were solubilized in TBS with 40 mM *n*-dodecyl β-D-maltoside (DDM) and clarified by ultracentrifugation. Solubilized membranes were incubated with Co^{2+} affinity resin and protein was eluted with buffer containing 300 mM NaCl, 20 mM Tris pH 8.0, 1 mM DDM, and 250 mM imidazole. Protein purification buffers for Δ13 were identical to those used for Δ25 but contained 150 mM NaCl. The histidine-tagged enhanced green fluorescent protein (EGFP) tag was cleaved with thrombin digestion and the protein was further purified by size-exclusion chromatography using a mobile phase containing 300 mM NaCl, 20 mM Tris pH 8.0, 2 mM *n*-decyl β-D-thiomaltopyranoside (C10ThioM), 1 mM dithiothreitol (DTT), 0.2 mM cholesteryl hemisuccinate (CHS) and 5 mM $BaCl_2$. Δ13 protein was further purified by size-exclusion chromatography (SEC) using a mobile phase containing 150 mM NaCl, 20 mM Tris pH 8.0, 1 mM DDM, 1 mM DTT, and 0.2 mM CHS. Peak fractions were collected and concentrated to ~2-3 mg ml^{-1}. The source for all cell lines was ATCC.

Crystallization: Crystallization of purified Δ25 protein was accomplished as previously described[156]. Purified Δ13 protein was used for crystallization trials immediately following SEC and was not subject to any additional treatment. The Δ13 crystals were obtained at 20°C by way of the hanging drop vapor diffusion method. Reservoir solution contained 100 mM HEPES pH 6.9, 150 mM sodium formate and 18% (w/v) PEG 3,350. Drops were composed of 1:1, 1:2, and 2:1 protein to reservoir ratios, respectively. Crystals typically appeared within 2 weeks. Crystals were cryoprotected with 30% (v/v) glycerol, in the protein-containing drop, before flash cooling in liquid nitrogen.

Anomalous scattering experiments: To locate Ba^{2+} sites on Δ25 channels, crystals were grown using a reservoir solution composed of 150 mM NaCl, 100 mM Tris pH 8.5, 20 mM $BaCl_2$, and 29% PEG 400 (v/v). The Δ25 crystals were soaked in solution containing 150 mM NaCl, 100 mM Tris pH 8.5, 50 mM $BaCl_2$, 36% PEG 400 (v/v), 2 mM C10ThioM and 0.2 mM CHS for 5 minutes prior to freezing in liquid nitrogen. To locate Cl^- sites on Δ25 channels, we exploited the anomalous scattering from bromide and grew crystals of Δ25 using a reservoir solution composed of 150 mM NaCl, 100 mM Tris pH 8.5, 5 mM $BaCl_2$ and 33% PEG 400 (v/v). Crystals were soaked in solution containing 150 mM NaBr, 100 mM Tris pH 8.5, 5 mM $BaCl_2$, 36% PEG 400 (v/v), 2 mM C10ThioM and 0.2 mM CHS for 2 minutes prior to freezing in liquid nitrogen. To locate Ba^{2+} sites on Δ13 channels, crystals were soaked in solution containing 150 mM sodium formate, 100 mM HEPES pH 6.9, 50 mM $BaCl_2$, 30% (v/v) glycerol, 1 mM DDM and 0.2 mM CHS for 5 minutes prior to freezing in liquid nitrogen.

Structure Determination: X-ray diffraction data sets were collected at the Advanced Light Source (ALS) beamline 5.0.2 and at the Advanced Photon Source (APS) beamline 24-ID-C. For anomalous diffraction experiments, diffraction data from crystals soaked in solutions containing 150 mM NaBr and belonging to the $P2_12_12_1$ space group were measured using an x-ray beam tuned to 13,490 eV at APS beamline 24-ID-C. Crystals soaked in solutions containing 50 mM $BaCl_2$ belonged to the $P2_12_12_1$ space group (Δ25) and H3 (Δ13) and diffraction data were measured using an x-ray beam tuned to 6,400 eV at ALS beamline 5.0.2. Diffraction for both $BaCl_2$ and NaBr-soaked crystals was measured to ~ 3.7-4.0 Å resolution.

Diffraction data were indexed, integrated, and scaled using XDS and XSCALE[130] software and structures were solved by molecular replacement using the PHASER program[132]. To identify anomalous difference peaks in Ba^{2+}-soaked and NaBr-soaked Δ25 crystals,

coordinates from the Δ25-Ba^{2+} structure[156] (PDB 5WKU) were used as a search probe for molecular replacement in PHASER and anomalous difference Fourier maps were generated in Phenix[158]. To identify anomalous difference peaks in Ba^{2+}-soaked Δ13 crystals, coordinates from the desensitized state structure[57] (PDB 4NYK) were used as a search probe for molecular replacement. To generate anomalous difference maps, diffraction data was truncated at 5.0 Å for Ba^{2+} and 6.0 Å for Br^-. Anomalous signals in the difference Fourier maps for Δ25 channels were enhanced by real-space averaging around the molecular 3-fold axis using Coot[133]. Anomalous difference peaks were inspected and used to assign Ca^{2+} binding sites in the Δ25-Ca^{2+} structure[156] (PDB 5WKV). Only peaks stronger than 6 σ were considered for Ba^{2+} peaks and greater than 5 σ for Br^- peaks after non-crystallographic symmetry averaging, in the corresponding anomalous difference electron density maps. Accession codes 5WKX (Supporting information figure 1), 5WKY (Supporting information figure 2), and 6CMC (Supporting information figure 3) correspond to Ba^{2+} sites on Δ25, Br^- sites on Δ25 and Ba^{2+} sites on Δ13, respectively.

Patch clamp recordings: Whole-cell patch clamp recordings of CHO-K1 cells expressing recombinant protein were performed as previously described[156]. The Axopatch 200B amplifier and pClamp 10 software were used for data acquisition and trace analysis and only single recordings were taken from individual cells. In high Ca^{2+} experiments, both low pH and conditioning solutions contained 10 mM Ca^{2+}. The source for all cell lines was ATCC.

Results

Crystallization of ASIC1a in resting and desensitized states

The Δ25 and Δ13 crystallization constructs span residues 25-463 and 14-463 of chicken ASIC1, a homolog of human ASIC1a, respectively, and maintain proton-dependent gating characteristics[55,56,156]. Crystals of resting Δ25 channels belong to the $P2_12_12_1$ space group and were obtained at high pH and in the presence of Ba^{2+}. Crystals of desensitized Δ13 channels belong to the H3 space group and were obtained at low pH. All x-ray structures were determined by molecular replacement and built via iterative rounds of manual model building and refinement. All ion sites were confirmed via anomalous diffraction experiments using synchrotron radiation tuned to 6,400 eV for Ba^{2+} and 13,490 eV for Br^- (**Table 3.1**).

Cation binding sites on the resting channel at high pH

Gating of chicken ASIC1a channels is modulated by Ca^{2+}, manifested as an acidic shift in pH_{50} with increasing concentrations of extracellular Ca^{2+} (**Figure 3.1a**). Despite extensive scrutiny, proposed mechanisms of gating modulation by Ca^{2+} remain uncertain. Inspection of the Fo-Fc density maps from the x-ray structure of a resting ASIC1a channel at high pH and in the presence of Ca^{2+}[156] revealed strong positive difference density positioned within the electrostatically negative acidic pocket and central vestibule, regions of the channel involved in proton-dependent gating[110]. In an effort to unambiguously assign binding sites for divalent cations on the resting channel structure, Δ25 crystals grown at high pH were soaked in Ba^{2+}, whose effect on ASIC1a channels mimics that of Ca^{2+}[51]. Inspection of anomalous difference electron density maps subjected to real space threefold averaging revealed nine Ba^{2+} sites within the acidic pocket and the central vestibule (**Figure 3.1b**), in general agreement with electron density maps from the Δ25-Ca^{2+} x-ray structure. However, given the resolution limitations we

are unable to define the protein atoms directly coordinating the Ba^{2+} ions and we therefore simply describe the protein residues that surround the ion sites.

The acidic pocket, an electrostatically negative cavern which harbors binding sites for toxins [55,56,101] and putative proton sites, and undergoes a large conformational change during channel activation, contains two anomalous difference peaks for Ba^{2+} on the resting channel at high pH. The 9 and 6 σ anomalous difference peaks for Ba^{2+} are positioned ~ 8 Å apart at opposite corners of the acidic pocket, which is in an expanded conformation at high pH (**Figure 3.1c**). Electron density is poor within the solvent-exposed cavern, restricting modeling of some sidechains to α-carbon atoms and precluding a comprehensive picture of ion coordination. Despite this limitation, the position of the 9 σ anomalous difference peak deep within the acidic pocket suggests possible coordination of Ba^{2+} by acidic residues Glu 98 and Glu 239 of the channel's finger domain. The weaker, 6 σ Ba^{2+} peak is situated at a subunit-subunit interface within the acidic pocket near highly conserved residues Glu 243 of the finger domain and both Glu 220 and Asp 408 from the palm domain of a neighboring subunit.

The central vestibule, buried within the channel core and situated along the threefold axis of resting ASIC1a channels, harbors a trio of threefold symmetric 8 σ anomalous difference peaks for Ba^{2+}. These Ba^{2+} ions are situated at the nexus of upper and lower palm domains ~ 5 Å from Glu 412, Glu 417, Glu 374 and Gln 277 residues and immediately off of β11-β12 linkers (**Figure 3.1d**).

Recently published x-ray structures of chicken ASIC1a in a resting state at high pH highlighted the structural transitions underlying channel activation and desensitization[156]. During the rapid transition from a non-conducting, resting state at high pH to the open state at low pH, the electrostatically negative acidic pocket collapses as helices α4 and α5 swing inwards towards

the acidic loop of the finger domain (**Figure 3.2a-b**). Collapse of the acidic pocket fully occludes the 9 σ peak positioned off of Glu 98 and Glu 239, suggesting that occupancy of this site may be incompatible with a fully activated channel and may therefore provide a mechanism for gating modification. In contrast, the 6 σ peak positioned near the carboxy-terminal end of α5 remains solvent-exposed, indicating that occupancy of this site may not contribute to gating modification by divalent cations (**Figure 3.2c**). These results indicate a degree of state-dependence with respect to divalent cation binding at the acidic pocket and suggest that acidic residues surrounding the 9 σ anomalous peak, including Glu 98 and Glu 239, are likely relevant to cation binding and thus to divalent cation modulation of ion channel gating.

Structural changes during activation take place throughout the ECD, resulting in a slight contraction of the central vestibule as the lower palm domain flexes towards the membrane (**Figure 3.2a, d**). Consequently, Arg 370 within the central vestibule pivots towards the palm domain of a neighboring subunit upon exposure to low pH. Activation-induced reorientation of Arg 370 positions its guanidine group into a direct clash with the Ba^{2+} site on the resting channel at high pH (**Figure 3.2e**), rendering the open channel's central vestibule not permissive to Ba^{2+} binding at the same site as in the resting channel. Because we do not have structural information on an open channel in complex with divalent cations, we cannot rule out the possibility of a unique binding site within the central vestibule that is only occupied in the open channel state. These results suggest that binding sites for divalent cations within the central vestibule are state-dependent and may play a previously unanticipated role in the modification of ASIC gating by divalent cations. Moreover, the location of Ba^{2+} within the central vestibule of the resting channel overlaps that of the putative binding site for quercetin, an inhibitor of ASIC1a, ASIC2a,

and ASIC3 homomers[108], suggesting that the central vestibule may serve as a common site for modulatory agents.

Cation binding sites on a desensitized channel at low pH

To better explore the state-dependence of divalent cation binding to ASICs, we soaked crystals of the Δ13 construct of chicken ASIC1a grown at low pH in Ba^{2+}, following a protocol identical to that used for Δ25 crystals grown at high pH. At low pH the Δ13 construct adopts the canonical desensitized channel structure[57], exhibiting a collapsed acidic pocket and closed gate. Inspection of anomalous difference electron density maps revealed a strong, ellipsoidal density for Ba^{2+} at the acidic pocket, indicating the presence of at least one bound ion (**Figure 3.3a**). Similar to the 6 σ site within the resting channel's acidic pocket, the Ba^{2+} site of the desensitized channel is positioned near the carboxy-terminus of α5 at the mouth of the pocket. The proximity of numerous acidic residues indicates possible coordination of Ba^{2+} by Asp 238, Asp 350 and Glu 354, all of which are located between 3.4 and 4.3 Å from the Ba^{2+} site (**Figure 3.3b**). Notably, divalent cation sites within the resting channel's central vestibule at high pH are absent on the desensitized channel at low pH. Moreover, despite a slight contraction at the central vestibule of the desensitized channel (Figure 3C), the conformation of the single Gln and three Glu residues that comprise the Ba^{2+} binding site on the resting channel site (**Figure 3.3d**) are remarkably similar in both resting and desensitized states. As such, the absence of an anomalous signal for Ba^{2+} for the desensitized channel, in addition to the presence of titratable resides lining the binding site, suggest that one or more of the aforementioned glutamate residues is protonated at low pH, thus disfavoring the binding of divalent cations.

Contribution of acidic residues to channel modulation

Inspection of electron density maps for the Δ25-Ca^{2+} x-ray structure (PDB 5WKV)[156] indicates that putative Ca^{2+} sites are in good agreement with anomalous difference peaks for Ba^{2+} on the resting channel at high pH. Within the acidic pocket and central vestibule of the Δ25-Ca^{2+} structure, Ca^{2+} ions are positioned off of Glu 98, Glu 220 and Glu 374 residues[156]. To illuminate their contribution to channel modulation, we neutralized these three acidic residues via single E98Q, E220Q and E374Q as well as triple E98Q/E220Q/E374Q substitutions. In all mutant channels, increasing extracellular Ca^{2+} from 2 to 10 mM shifted the pH_{50} to more acidic values, though with less statistical significance than observed in cASIC1a channels (**Figure 3.4a-b**). The effect on modulation of gating by Ca^{2+} was least pronounced in the E220Q mutant, in good agreement with the observation from anomalous diffraction experiments that the divalent cation site within the acidic pocket near Glu 220 is occupied in both resting and desensitized states. Moreover, in contrast to all other mutant channels, neutralization of Glu 220 did not have a meaningful effect on pH_{50} at 2 mM Ca^{2+} when compared to cASIC1a (**Figure 3.4a-b**).

Our electrophysiological results highlight the complex relationship between divalent cation binding and gating in ASICs. We suggest that evidence of divalent cation binding within regions of the channel that undergo pH-dependent conformational changes as well as differences in Ba^{2+} sites observed between resting and desensitized channels demonstrate that ion occupancy is at least partly state-dependent and indicative of an overlap between pH-dependent gating and ion coordination. Furthermore, for E98Q, E374Q and triple mutant channels, changes in pH_{50} values in 2 mM Ca^{2+} as well as the less significant effect of Ca^{2+} on gating indicate that these residues both participate in proton-dependent gating and may contribute to modulation of gating by extracellular Ca^{2+}. However, our electrophysiological results fall short of conclusively

identifying residues within the acidic pocket or central vestibule that are essential to the mechanism by which divalent cations modulate channel gating. As such, additional experiments are required to generate a comprehensive understanding of the molecular mechanisms by which divalent cations modulate ASICs.

State-dependent chloride binding

Cl^- is the predominant anion in the CNS, with extracellular concentrations maintained at ~ 120-130 mM[159,160]. Additionally, Cl^- has been shown to modulate the function and structural stability of kainate receptors via a binding site at a subunit interface[160]. In structures of ASIC channels in open and desensitized states, a bound Cl^- ion is located within the thumb domain coordinated by Arg 310 and Glu 314 of helix α4 and by a neighboring subunit via Lys 212[20,55,57] (**Figure 3.5a-b**). Disrupting Cl^- binding at this site alters pH-dependent gating, speeds desensitization and attenuates channel tachyphylasis[153]. Notably, no electron density for Cl^- was observed in structures of a resting ASIC1a channel at high pH[156]. Additionally, the rearrangement of thumb helices α4 and α5 to form the resting channel's expanded acidic pocket at high pH disrupts the subunit-subunit interface at the carboxy-terminus of α5 and alters the architecture of the canonical and highly conserved Cl^- binding site (**Figure 3.5b**). These results suggest that Cl^- binding within the thumb domain of ASICs may be state-dependent and demonstrate how Cl^- may play a role in channel gating by stabilizing the collapsed conformation of the acidic pocket at low pH.

To further probe Cl^- binding to the resting channel at high pH, we soaked Δ25 crystals in 150 mM NaBr. Consistent with 2Fo-Fc density maps from Δ25-Ba^{2+} and Δ25-Ca^{2+} x-ray structures[156], anomalous difference maps subjected to real space threefold averaging did not indicate the presence of a bound Cl^- ion at the canonical thumb domain site. Surprisingly, further

inspection of these difference maps revealed strong peaks located at the mouth of the extracellular fenestrations, just above the TMD (**Figure 3.5c**). Placement of a Cl^- ion at this high pH binding site off of Lys 77 and Lys 422 partially occludes the narrow extracellular fenestrations that provide access for Na^+ ions to the channel pore (**Figure 3.5d-e**) and that undergo a dramatic expansion upon channel activation[156]. Furthermore, a recent study demonstrated that Lys 422, positioned less than 3 Å from the high pH Cl^- site, is important for inhibition of ASIC1a by ibuprofen[70], indicating that this region of the channel is critical for proton-dependent gating and serves as a binding site for channel modulators. Moreover, while the biological significance of a high pH Cl^- site on the resting channel remains unknown, the absence of a bound Cl^- at the canonical low pH site in crystal structures of the resting channel at high pH demonstrates how Cl^- ions, in addition to protons and divalent cations, play an important role in the pH-dependent function of ASICs.

Discussion

Here we map binding sites for anions and divalent cations, determined by anomalous scattering x-ray crystallography, on x-ray structures of resting and desensitized ASIC1a channels at high and low pH, respectively. At high pH, each subunit of the resting channel harbors three binding sites for divalent cations, two of which are within the expanded conformation of the acidic pocket, and one is within the central vestibule. At low pH, the desensitized channel contains a single Ba^{2+} site at the edge of the acidic pocket. Thus, upon transition from the high pH resting state to the low pH desensitized state the divalent cation binding site in the central vestibule is lost and there is a reduction in the number of binding sites in the acidic pocket,

consistent with the notion that divalent cations bind to and stabilize the high pH resting state of the channel.

We also demonstrate that the high pH resting state of the channel lacks a bound Cl^- ion within the thumb domain[20]. This binding site for Cl^-, or Br^-, is occupied in low pH desensitized and MitTx-bound open states, the latter of which was determined at pH 5.5. Electrophysiological studies have shown that this Cl^- site is important for ion channel desensitization kinetics and tachyphylaxis[153]. When we carried out anomalous scattering x-ray crystallography experiments to study the occupancy of the thumb domain Cl^- site at high pH we found no evidence of ion binding, demonstrating that the thumb domain Cl^- site is unoccupied at high pH. The absence of a bound Cl^- within the thumb domain at high pH is likely due to conformational changes at the Cl^- site resulting from the pH-dependent expansion of the acidic pocket. Fortuitously, our crystallographic experiments uncovered a halide binding site at the extracellular fenestrations of the ion channel pore in the high pH structure of the resting channel. Further experiments are required to determine the significance of these halide binding sites on ion channel function.

A recent report demonstrated a binding site for Ca^{2+} within the pore of rat ASIC3 located within a ring of Glu residues that correspond to Gly in cASIC1a[152]. These results further corroborate the observation of a Ca^{2+}-dependent block reported previously for ASIC3 channels[53]. Intriguingly, neither our anomalous diffraction data nor inspection of electron density maps from the Δ25-Ca^{2+} x-ray structure (PDB 5WKV)[156] indicate the presence of divalent cations near or within the channel pore as has been previously proposed[52]. However, lacking structural information from an open ASIC1a channel in complex with divalent cations, we are unable to rule out the possibility of a binding site at the pore unique to the open channel.

Finally, while both Ba^{2+} and Ca^{2+} modify ASIC gating and have similar coordination requirements, Ba^{2+} has a slightly larger ionic radii[12] and it is possible that Ba^{2+}-based anomalous diffraction experiments may preclude the detection of all Ca^{2+} binding sites. Therefore, while anomalous difference peaks confirm the presence of Ba^{2+} sites in resting and desensitized x-ray structures, we acknowledge the possibility of Ca^{2+} sites on ASIC1a that are incompatible with Ba^{2+} binding and thus undetected by our current experimental methods.

State-dependence for both anion and cation binding suggests an interplay between ion binding and proton-dependent gating in ASIC1a. Moreover, our results show that binding sites for divalent cations are positioned within electrostatically negative regions of the channel that undergo substantial conformational changes during gating[156], highlighting potential mechanisms of modulation. Therefore, while our results fall short of providing a detailed molecular mechanism or identifying individual residues responsible for modulation of ASICs by endogenous ions, these data underscore the complexity of the mechanisms underlying ionic modulation of ASICs and highlight the importance of additional experimentation to further improve our understanding of the relationship between ion binding and channel gating.

Acknowledgements

We thank A. Goehring, D. Claxton and I. Baconguis for initial construct screening and advice through all aspects of the project, L. Vaskalis for help with figures, H. Owen for manuscript preparation and all Gouaux lab members for their support. We acknowledge the Berkeley Center for Structural Biology and the Northeastern Collaborative Access Team for help with x-ray data collection. E.G. is an investigator with the Howard Hughes Medical Institute.

Tables

	Δ25-Ba^{2+} Resting Ba^{2+} - soaked (5WKX)	Δ13-Desensitized Ba^{2+} - soaked (6CMC)	Δ25-Ba^{2+} Resting Br^{-} - soaked (5WKY)
Data collection	ALS 502	ALS 502	APS 24ID-C
Space group	$P2_12_12_1$	H3	$P2_12_12_1$
Cell dimensions a, b, c (Å)	108.0 126.3 156.3	133.9 133.9 122.7	109.6 134.5 159.1
Cell angles α, β, γ (°)	90.0, 90.0, 90.0	90.0, 90.0, 120.0	90.0, 90.0, 90.0
Wavelength (Å)	1.94	1.94	0.9191
Resolution (Å)*	50 – 4.0	42.14 – 3.7	45 – 4.00
Completeness*	99.5 (97.1)	99.61 (98.8)	99.9 (99.4)
Multiplicity*	4.1 (5.1)	3.6 (3.5)	7 (6.2)
I/σI*	8.82 (0.81)	6.78 (0.98)	9.46 (0.77)
R_{meas} (%)*	11.8 (326.9)	15.2 (135.7)	13.2 (206.6)
$CC_{1/2}$ (%)*	99.9 (35.7)	99.7 (31.6)	100 (53.4)
Refinement			
Resolution (Å)	49.7 – 4.0	42.1 – 3.7	43.2 – 4.0
No. of reflections	17205	8949	20402
R_{work}/R_{free}	30.2/31.3	28.4/30.0	28.1/29.9
Average *B*-factor (A^2)			
Protein	142.0	133.0	133.0
Ligand	190.8	119.9	181.6
R.m.s. deviations			
Bond lengths (Å)	0.004	0.004	0.004
Bond angles (°)	0.705	0.98	0.706
Ramachandran plot			
Favored (%)	98.31	95.39	98.31
Allowed (%)	1.69	4.61	1.69
Disallowed (%)	0	0	0
Rotamer outliers (%)	1.24	1.78	1.24

Table 3.1. Crystallographic data collection and refinement statistics.

*Highest resolution shell in parentheses.

5% of reflections were used for calculation of R_{free}.

Figures and legends

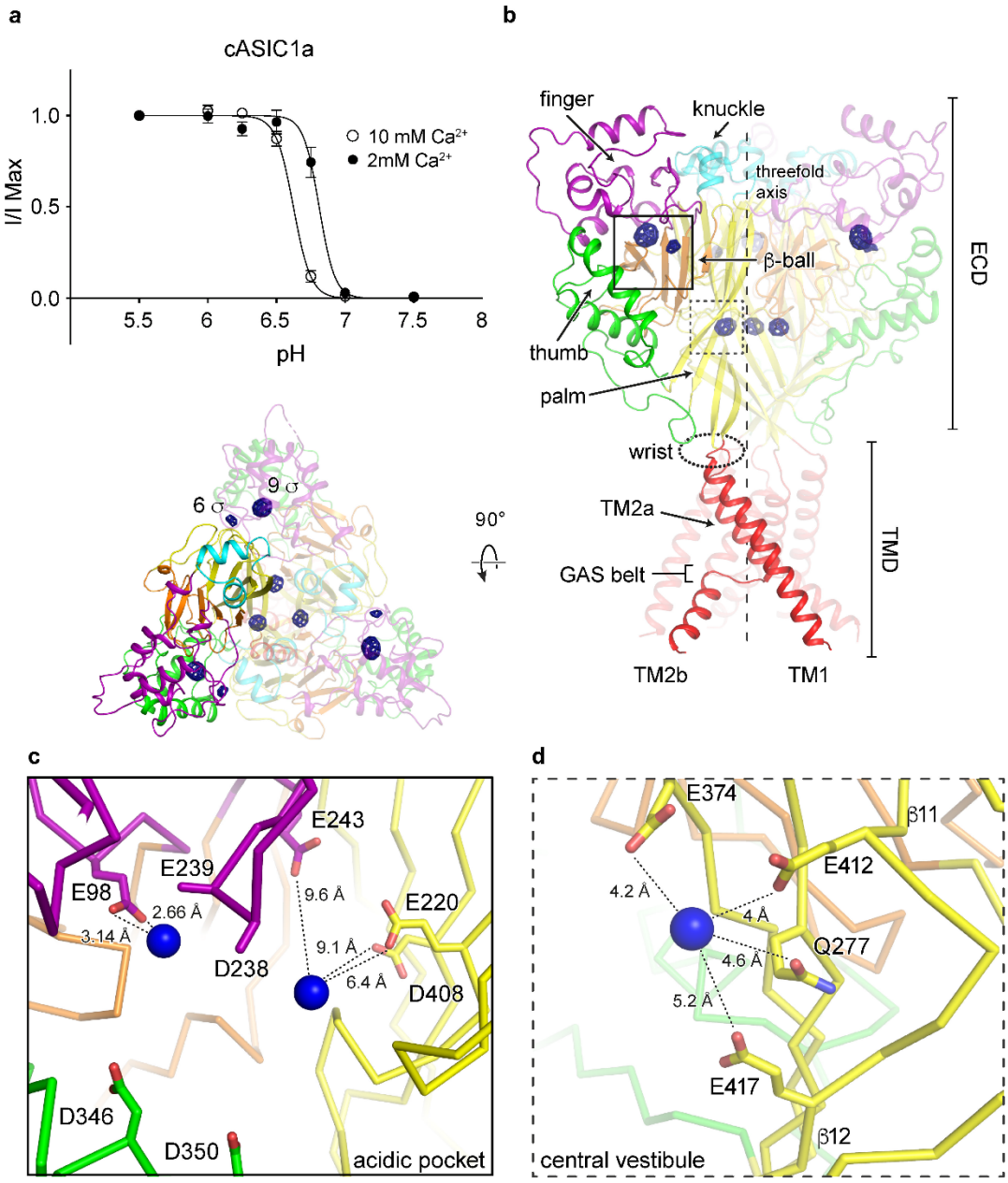

Figure 3.1. Binding sites for divalent cations on a resting chicken ASIC1a channel at high pH. a, Proton dose-response curves for cASIC1a channels in 2 or 10 mM external Ca^{2+}. Error bars represent SEM, n = 4-8 cells. Data were collected in whole-cell patch clamp configuration from adherent CHO-K1 cells transfected with cDNA for cASIC1a channels. **b-d,** Ba^{2+} anomalous difference peaks (blue mesh) contoured at 5.5 σ and mapped on a resting channel at

high pH (**b**, channel colored by domain) with detail views of the acidic pocket (**c**) and central vestibule (**d**) binding sites. Blue spheres represent Ba^{2+}.

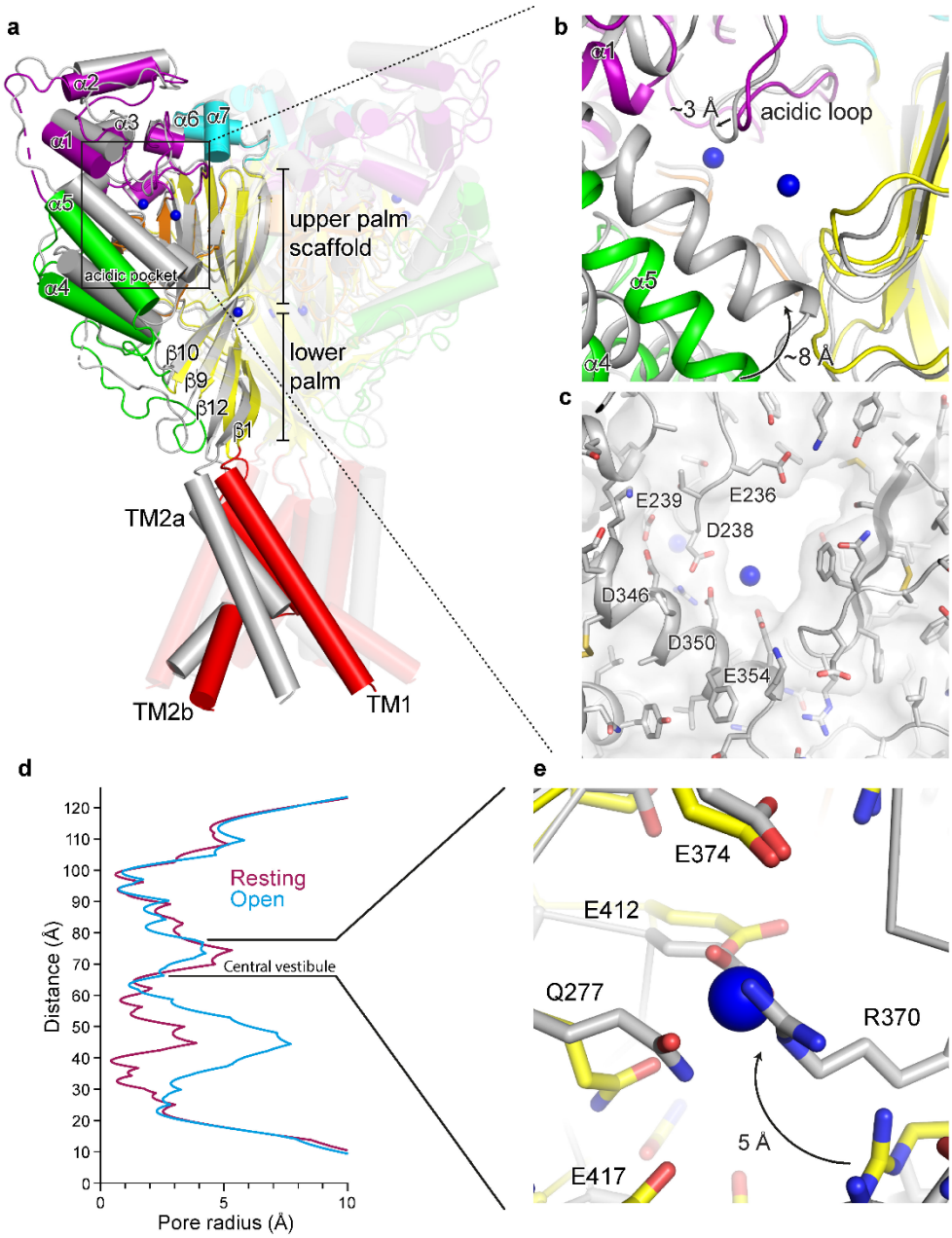

Figure 3.2. Activation initiates changes at binding sites for divalent cations. a-b, Superposition of resting and open (PDB 4NTW, grey) channels (**a**) with a detailed view of the acidic pocket (**b**). Blue spheres represent Ba^{2+} sites of the resting channel. **c,** Surface representation of the collapsed acidic pocket of the open channel (PDB 4NTW, grey). Blue spheres represent Ba^{2+} sites of the resting channel. **d,** Pore profiles for resting (PDB 5WKU) and open (PDB 4NTW) channels. **e,** Detail view of the central vestibule of superposed resting and open (PDB 4NTW, grey) channels. Blue spheres represent Ba^{2+} sites of the resting channel.

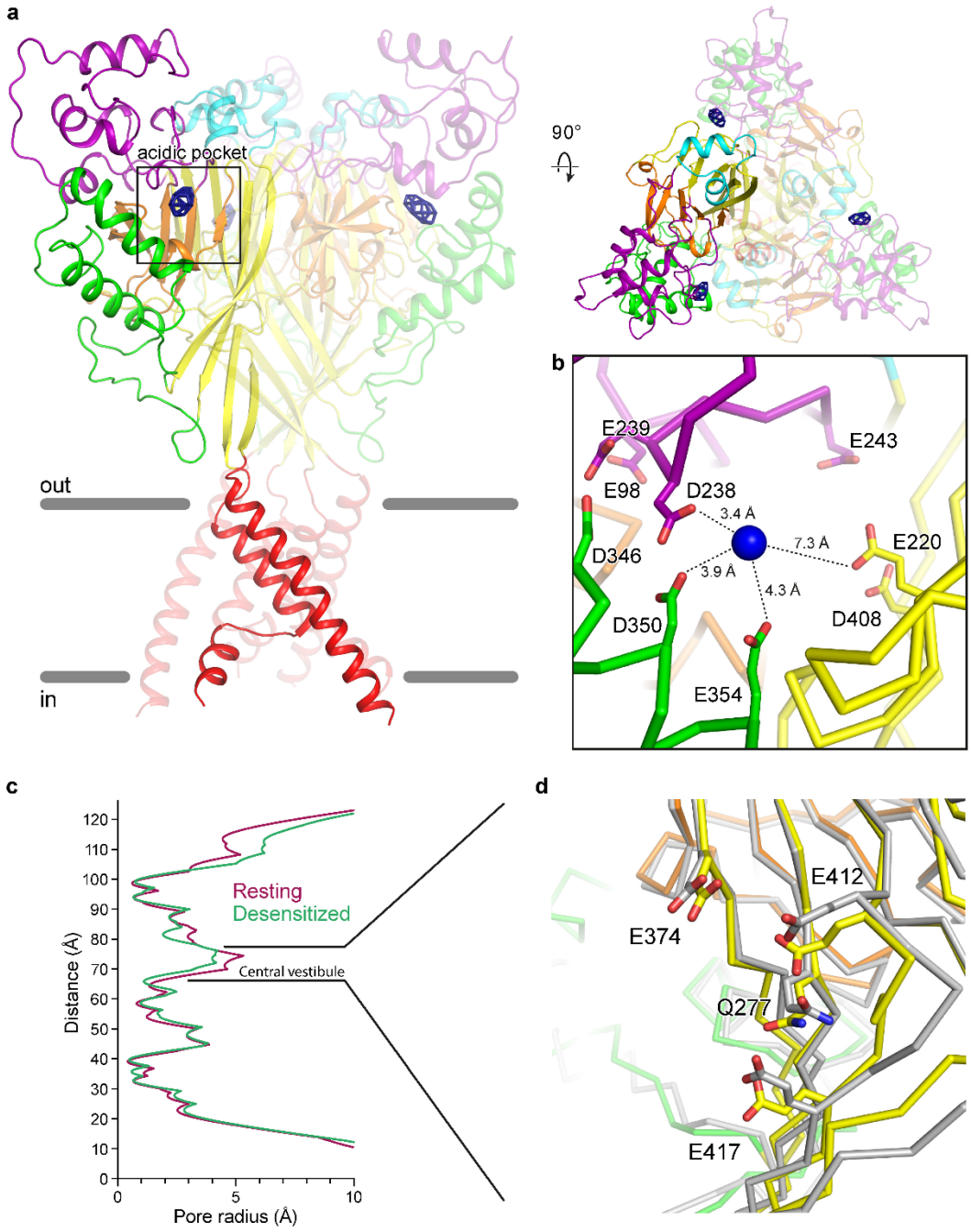

Figure 3.3. Binding sites for divalent cations on a desensitized chicken ASIC1a channel at low pH. a, Ba^{2+} anomalous difference peaks (blue mesh) contoured at 6.5 σ and mapped on a desensitized channel at high pH (channel colored by domain). **b,** Detail view of the Ba^{2+} binding site within the acidic pocket. Blue spheres represent Ba^{2+} sites of the desensitized channel. **c,**

Pore profiles for resting (PDB 5WKU) and desensitized channels. **e,** Detail view of the central vestibule of superposed desensitized and resting (PDB 5WKU, grey) channels.

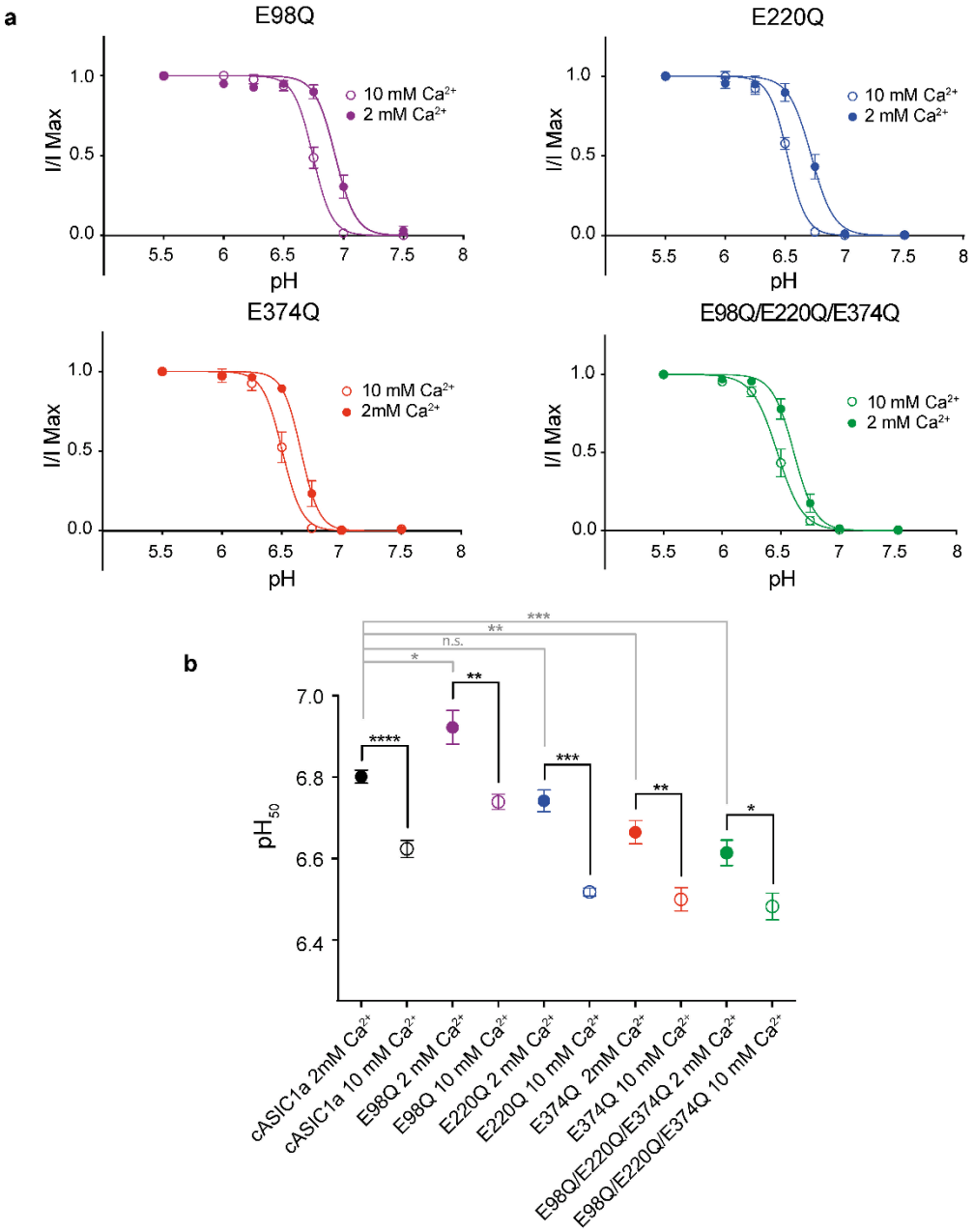

Figure 3.4. Gating modification by Ca2+ in cASIC1a neutralization mutants. a, Dose response data in 2 or 10 mM Ca^{2+} for cASIC1a mutant channels. Data were collected in whole-cell patch clamp configuration from adherent CHO-K1 cells transfected with cDNA for mutant channels. **b,** Unpaired t-test results (two-sided) comparing changes in pH_{50} for cASIC1a (dose response data shown in Figure 1A) and mutant channels in 2 vs 10 mM Ca^{2+} (black lines) or

comparing pH_{50} of cASIC1a to individual mutant channels in 2 mM Ca^{2+} (grey lines). For all experiments, error bars represent SEM, n = 4-8 cells. For comparisons of pH_{50} values for each channel at 2 or 10 mM Ca^{2+}, p values and 95% confidence intervals in parentheses are $p < 0.0001$ (-0.237 to -0.118) for cASIC1a, 0.0078 (-0.296 to -0.070) for E98Q, 0.0002 (-0.293 to -0.156) for E220Q, 0.0022 (-0.255 to -0.075) for E374Q), and 0.0165 (-0.234 to -0.030) for E98Q/E220Q/E374Q. For comparisons of pH_{50} values between channels at 2 mM Ca^{2+}, p values and 95% confidence intervals in parentheses are $p < 0.0405$ (0.008 to 0.234) for cASIC1a and E98Q, 0.0935 (-0.132 to 0.013) for cASIC1a and E220Q, 0.0036 (-0.213 to -0.060) for cASIC1a and E374Q, and 0.0006 (-0.268 to -0.107) for cASIC1a and E98Q/E220Q/E374Q.

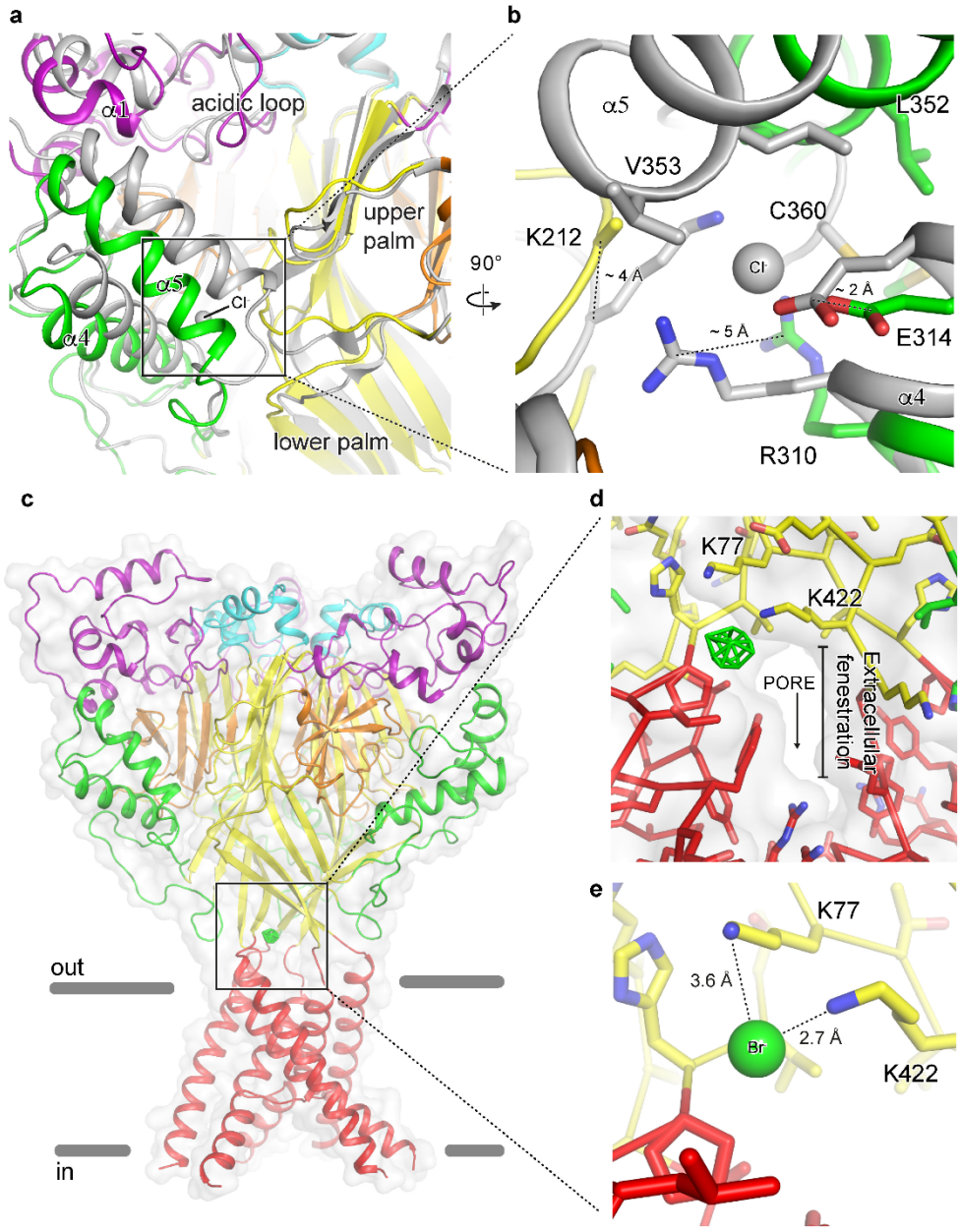

Figure 3.5. Anion binding site of a resting chicken ASIC1a channel. a-b, The acidic pocket (**a**) and canonical thumb domain Cl^- binding site (**b**) of superposed resting and desensitized (grey) channels. **c-e,** Br^- anomalous difference peak (green mesh) contoured at 5 σ and mapped on a resting channel at high pH (**c**) and detail views of the Br^- binding site with (**d**) and without (**e**) surface representation. One anion site, of the three, is shown.

Chapter 4

Structures of acid-sensing ion channels in a lipid environment reveal motifs central to gating and ion permeation

The contents of chapter four will be submitted for publication in modified form:

Yoder, N. and Gouaux, E. Structures of acid-sensing ion channels in a lipid environment reveal motifs central to gating and ion permeation. (to be submitted)

Author Contributions

N.Y. and E.G. designed the project. N.Y. performed the biochemistry, structural analysis and electrophysiology recordings. N.Y wrote the manuscript and all authors edited the manuscript.

Abstract

Acid-sensing ion channels (ASICs) are voltage-insensitive and proton-gated members of the epithelial sodium channel/degenerin (ENaC/DEG) superfamily of ion channels and are expressed throughout central and peripheral nervous systems. The homotrimeric splice variant ASIC1a has been the focus of particular scrutiny given its role in nociception, fear memory formation and mood disorders and, as such, represents a valuable therapeutic target. Here we present atomic models of full-length chicken ASIC1a channels in both high pH resting and low pH desensitized conformations and in a membrane-like lipid environment by single-particle cryo-electron microscopy (cryo-EM). The structures of resting and desensitized channels were solved to nominal resolutions of 3.7 and 2.8 Å, respectively, and expose a re-entrant loop prior to the first transmembrane domain that harbors a conserved His-Gly motif known to be critical for gating in ENaCs that had not been observed in prior x-ray or cryo-EM structures.

Introduction

In humans, four ASIC genes, in concert with splice variants, encode for at least eight distinct subunits that assemble as proton-gated voltage-insensitive heteromeric or homomeric channels. The homotrimeric splice variant ASIC1a is primarily localized to the dendrites, post-synaptic spines, and cell bodies of central neurons[34,84] and is enriched in the amygdala[79]. ASIC1a channels participate in an array of central nervous system (CNS) processes including fear conditioning[77,78,86], nociception[39,66] and synaptic plasticity[67,74-76] and are therapeutic targets[83,161,162] with localization patterns, Ca^{2+} permeability and proton-dependent activation implicating these channels in acidosis-induced neuronal injury[64,80,82,163] and mood disorders[87,88].

Homotrimeric ASIC1a channels exhibit moderate Na^+ selectivity with $P_{Na} / P_K \sim 7.8$ and $P_{Na} / P_{Ca} \sim 18.5$ [126,127] and fast gating kinetics[43], opening in response to acidosis in milliseconds and entering a long-lived desensitized state in hundreds of milliseconds[145]. As such, the gating mechanism of ASICs can be best described as containing three primary states: high pH resting, low pH open and low pH desensitized[54].

Members of the ENaC/DEG superfamily of ion channels are trimers, with each subunit composed of a large extracellular loop, two transmembrane helices, and intracellular amino and carboxyl termini[20]. The most structurally well-characterized of the ENaC/DEG family of ion channels, previous x-ray and single-particle cryo-EM structures of chicken ASIC1a in detergent micelles highlighted distinct conformations associated with resting[156], open[55] and desensitized[20,57] states. These findings defined conducting and non-conducting pore profiles and elucidated molecular mechanisms for proton-dependent gating and desensitization. Notably, residues belonging to the intracellular termini have been disordered in all existing x-ray and

cryo-EM structures, representing a significant gap in our understanding of how these regions contribute to channel function.

Numerous lines of evidence indicate that the amino terminus of ENaC/DEG channels contributes to gating and ion conduction properties, including a conserved His-Gly (HG) motif located within the amino terminus known to be critical for gating in ENaCs. Indeed, mutation of the conserved glycine in the β subunit of ENaC channels reduces channel open probability[114] and underlies one form of Pseudohypoaldosteronism type 1 (PHA-1)[115]. In ASICs, pre-transmembrane domain 1 (TM1) amino terminal residues have been shown to participate in ion selectivity and proton-dependent gating[104], further demonstrating that the amino terminus of ENaC/DEG channels plays an important role in ion channel function and may comprise portions of the ion pore. Ultimately, despite the wealth of structural information surrounding ASICs and, more recently, ENaCs[164], the architecture of the cytoplasmic terminal domains as well as the molecular mechanisms by which the HG motif in particular or the pre-TM1 residues in general contribute to channel function have remained elusive.

Here we present structures of full-length homotrimeric chicken ASIC1a channels (cASIC1a) in a membrane-like lipid environment at low and high pH. Our results reveal that amino terminal pre-TM1 residues form a re-entrant loop, and that the highly conserved HG motif supports the GAS belt TM2 domain swap from below at a subunit interface along the lower ion permeating pathway. Furthermore, we show that the lower half of the ion permeation pathway in resting and desensitized states is comprised entirely of pre-TM1 re-entrant loop residues, informing mechanisms for the contribution of the amino terminus to ion permeation properties. These studies provide structures of an ASIC in a membrane-like environment and uncover a

novel structural motif central to gating and ion permeation and of high therapeutic relevance to the entire ENaC/DEG superfamily of ion channels.

Materials and methods

Expression and purification of cASIC1a channels: Recombinant full-length acid-sensing ion channels (gallus gallus) were expressed in modified HEK-293 cells and membrane fractions were isolated as previously described[156]. Membrane pellets were resuspended in ice cold tris-buffered saline (TBS) containing protease inhibitors, dounce homogenized, and solubilized for 1 hour at 4°C by addition of SL30010 (polyscope) styrene-maleic acid copolymers to 2% (w/v) final concentration. Membrane debris was removed via centrifugation at 40,000 rpm for 30 minutes at 4°C and the supernatant containing SMA-cASIC1a particles was bound in batch to Ni-NTA beads overnight at 4°C in the presence of 10 mM imidazole.

SMA-cASIC1a particles bound to Ni-NTA beads were immobilized on an XK-16 column and subject to two washes, first with three column volumes of TBS containing 10 mM imidazole and last with three column volumes of TBS containing 30 mM imidazole. Purified SMA-cASIC1a particles were eluted with TBS containing 250 mM imidazole, and peak fractions were pooled and concentrated to ~ 5 mg/ml. 8x-His enhanced green fluorescent protein (EGFP) tag was removed via thrombin digestion (1:25) overnight at room temperature (RT). The following day, SMA-cASIC1a particles were further purified via size-exclusion chromatography (superose 6 increase) using a mobile buffer composed of TBS with 1 mM dithiothreitol (DTT). A single peak fraction was collected and concentrated to ~ 1 mg/ml for cryo-EM sample preparation.

Cryo-EM of SMA-cASIC1a particles*:* Quantifoil holey carbon grids (R1.2/1.3 200 mesh Au) were glow discharged for 1 minute at 15 mA, carbon side facing up. For structure determination

of SMA-cASIC1a particles at high pH, purified protein at ~ 1 mg/ml was used immediately for grid preparation. For structure determination at low pH, the pH of the sample was adjusted to 7.0 by addition of MES pH 6.0 following concentration of purified protein to ~ 1.0 mg.ml.

4 μl of sample, applied to the carbon side of the grid, was blotted manually with pre-cooled filter paper (Whatman, grade 1) and the grids were vitrified in ethane/propane mix using a custom-built manual-plunge apparatus housed in a 4°C cold room with 60-70% relative humidity.

Cryo-EM data acquisition for SMA-cASIC1a*:* For the resting channel structure at high pH, data were collected on a Titan Krios cryo-electron microscope (ThermoFisher) operated at 300 keV. Images were recorded on a Gatan K3 camera positioned after an energy filter (20 eV slit width) operating in super-resolution mode with a binned pixel size of 0.648 Å. Data were collected with SerialEM[135] and dose-fractionated to 50 frames for a total exposure time of 2-3 s and a total dose of 40-50 e^{-} $Å^{-2}$.

For the desensitized channel structure at pH 7.0, data were recorded on a Titan Krios cryo-electron microscope operated at 300 kV and equipped with a spherical aberration corrector. Images were recorded on a Gatan K2 Summit camera in super-resolution mode with a binned pixel size of 1.096 Å. Data were acquired using Leginon[165] and dose-fractionated to 48 frames at 0.15 s per frame for a total exposure time of 7.25 s and a total dose of 50 e^{-} $Å^{-2}$.

Cryo-EM data processing for SMA-cASIC1a*:* Images were motion corrected using UCSF MotionCor2[136] and CTF estimation was performed using Gctf[137]. Particles picked using DoG Picker[138] were subjected to reference-free 2D classification in cryoSPARC V2[166]. Following initial classification, an ab-initio model was generated in cryoSPARC V2 and used for iterative rounds of 3D classification and refinement in cryoSPARC V2. For the low pH dataset, per-

particle CTF estimation was performed using Gctf. Final reconstructions for both datasets were obtained via non-uniform refinement (C3 symmetry) in cryoSPARC V2.

Electrophysiology recordings*:* Whole-cell patch-clamp recordings were conducted on sf9 cells 1-3 days after infection with BacMam virus containing DNA encoding EGFP-cASIC1a or cysteine substitution mutant channels. For all electrophysiology experiments, all cells were recorded from only once and membrane voltage was clamped at -60 mV. Pipettes pulled to 2-4 MΩ resistance were filled with internal solution containing 150 mM KCl, 2 mM $MgCl_2$, 5 mM EGTA, and 10 mM HEPES pH 7.35. External solution contained 150 mM NaCl, 2 mM $MgCl_2$, 2 mM $CaCl_2$ and 8/4 mM Tris/MES pH 8.0 or 5.5. The Axopatch 200B amplifier and pClamp 10 software suite were used for data collection and analysis.

Results

Architecture of resting and desensitized channels in a lipid environment

To maintain ASICs in a native-like local lipid environment through structure determination, we extracted and purified recombinant full-length chicken ASIC1a channels in lipid particles bounded by styrene-maleic acid (SMA) copolymers[167,168]. After two step chromatographic purification, SMA-cASIC1a particles showed good purity by SDS-PAGE analysis and were monodisperse by fluorescence-detection size exclusion chromatography (FSEC) [169] (**Figure 4.1a-b**). Furthermore, preliminary negative stain transmission electron microscopy demonstrated good particle distribution and limited aggregation (**Figure 4.1c**).

Pursuing single-particle cryo-EM of SMA-cASIC1a particles, we obtained reconstructions of ASIC1a channels in low pH desensitized (pH 7.0) and high pH resting (pH 8.0) conformations to ~ 2.8 and 3.7 Å, respectively (**Table 4.1, Figures 4.2-4.5, Figure 4.6a-b**).

The homotrimeric ASIC1a channel resembles a clenched fist composed of thumb, palm, finger, knuckle, wrist, β-ball and transmembrane domains (TMDs) and harbors domain-swapped TM2 helices (**Figure 4.6c**). Both desensitized and resting channels are closed to ion permeation as evidenced by a constricted gate within the upper third of the TMD (**Figure 4.6d-e**). At pH 7.0, SMA-cASIC1a populates a desensitized state that mirrors the architecture of the existing x-ray structure[57], including the presence of a proton-bound collapsed acidic pocket (**Figure 4.6f**). In contrast, SMA-cASIC1a particles maintained at pH 8.0 occupy a high pH resting conformation, characterized by an expanded acidic pocket (**Figure 4.6g**) that mimics both x-ray and cryo-EM structures solved previously at high pH[156] .

Amino terminal residues form a re-entrant loop

Numerous experiments have implicated residues within the pre-TM1 region of ASICs and ENaCs in both gating and selectivity[102,104,114]. Indeed, the highly conserved 'His-Gly' (HG) motif, disruption of which lowers the open probability in ENaCs and underlies PHA type 1 disorder[114,115], is located within the pre-TM1 region of ASICs and ENaCs. Intriguingly, all existing x-ray and cryo-EM structures of ASIC1a and ENaC channels contain disordered terminal residues and, as such, structural mechanisms for a contribution of the amino terminus to gating and permeation in ENaC/DEG channels has remained elusive.

Surprisingly, in cryo-EM maps of both desensitized and resting SMA-cASIC1a channels maintained in a membrane-like environment, strong protein density corresponding to amino terminal residues was observed (**Figure 4.7a-b**). The quality of the 2.8 Å density map pertaining to the desensitized conformation was sufficient to extend the existing model to residue 17 of cASIC1a (**Figure 4.2**) and demonstrated that pre-TM1 residues form a re-entrant loop motif comprised of two short helical segments separated by a loop abutting the GAS-belt TM2 domain

swap from the cytoplasmic side (**Figure 4.7c-g**). Interestingly, the presence of the re-entrant loop does not noticeably impact the position of either transmembrane helix from those observed in prior x-ray or cryo-EM structures. Rather, the re-entrant residues are pinned within the inverted 'v-shaped' cavity formed between the lower transmembrane helices and maintained primarily by virtue of intra-subunit contacts with TM2b and TM1 (**Figure 4.8**).

While the quality of the resting channel's density map at the pre-TM1 residues was not sufficient for unambiguous model building (**Figure 4.4c**), no significant differences in re-entrant loop conformation were observed between desensitized or resting channels at the current resolutions (**Figure 4.7f**), allowing us to rigid body fit pre-TM1 residues into the resting state map. Contrary to the amino terminus, the majority of the residues belonging to the cytoplasmic termini remained unresolved in both reconstructions.

The re-entrant loop harbors the His-Gly motif

Separated by more than 400 residues in sequence space, both GAS and HG motifs are highly conserved amongst ENaC/DEG channels (**Figure 4.9a**) and have been extensively implicated in gating[102] and ion selectivity[35,123,144,170]. Interestingly, the HG motif, which contains a well-characterized disease mutation at the absolutely conserved Glycine residue[114,115], is situated on the loop between the re-entrant helices where it supports the TM2 domain swap and GAS belt residues from below (**Figure 4.9b**). Residing along the ion permeation pathway and at a subunit interface, the HG motif is capped by the carboxyl terminus of TM2a via an intra-subunit hydrogen bonding interaction with Ile 442 and participates in an inter-subunit hydrogen bonding interaction with a neighboring GAS-belt residue via Ser 445 (**Figure 4.9c**). That this intricate network of intra- and inter-subunit interactions is formed between highly conserved

motifs via the TM2 domain swap and amino terminal re-entrant loop underscores the critical nature of the lower pore architecture to ENaC and ASIC function.

To probe the physiological relevance of the unique re-entrant pre-TM1 architecture, we engineered a disulfide bridge via directed cysteine substitutions at Thr 27 and Thr 448, which engage in a hydrogen bonding interaction connecting TM1 and TM2b (**Figure 4.9b-c**). Whole-cell patch clamp experiments show that the double-cys substitute retains proton-dependent gating and rapid activation of the wild-type channel but harbors markedly disparate desensitization characteristics (**Figure 4.9d**). In lieu of a reconstruction of the proton-activated channel in a membrane-like environment, these results suggest that channel activation and desensitization may not require a rearrangement of the pre-TM1 re-entrant loop, but that desensitization kinetics are sensitive to disruptions of the local chemical environment surrounding the TM2b and pre-TM1 interface.

Pre-TM1 residues form the lower ion permeation pathway

In structures of both desensitized and resting SMA-cASIC1a channels, the upper ion permeation pathway is comprised of TM2a residues and contains a closed gate between Gly 432 and Gly 436, in good agreement with existing x-ray and cryo-EM models (**Figure 4.10a**). However, where structures of ASIC1a in resting[156], open[55] and desensitized[57] conformations highlight a lower ion permeation pathway comprised entirely of TM2 residues that expands outwards to form a wide intracellular vestibule, re-entrant amino terminal residues of SMA-cASIC1a channels line a narrow ion permeation pathway extending below the GAS belt (**Figure 4.10a-b**).

The electrostatically negatively ion conduction pathway of non-conducting SMA-cASIC1a channels is formed by re-entrant amino terminal residues Ser 24 through His 29

(**Figure 4.10c**), the latter of which is situated immediately below the GAS belt and is oriented towards the threefold axis where it forms the primary constriction point below the gate in the desensitized channel (**Figure 4.10d**). Our data demonstrate that pre-TM1 residues line the lower ion conduction pathway in structures of non-conducting cASIC1a channels embedded in a membrane-like environment, providing a structural rationale for earlier reports which indicated that pre-TM1 residues may form part of the pore[103] and contribute to ion permeation and Na^+ selectivity of ASICs[104].

In the x-ray structure of an open channel, hydrated Na^+ ions encounter a central constriction at the GAS belt TM2 domain swap[55], which has long been thought to underpin ion selectivity in ENaC/DEG channels[35,123,124]. Recently, however, residues along TM2a and TM2b both above and below the GAS belt have been demonstrated to be important determinants of selectivity in ASIC1a[125]. Despite the presence of an ordered re-entrant loop and a narrower pore, we did not observe a change in the position of either TM2a/b or the GAS belt residues. As such, despite defining potential roles for re-entrant amino terminal residues in ion conduction and gating, in the absence of the structure of a full-length open channel in a membrane-like environment we cannot extend our structural data beyond a non-conducting pore and are therefore unable to address mechanisms of selectivity.

Putative lipid density hints at protein-membrane interactions

Contrary to conventional nanodisc methods, SMA copolymers are capable of extracting membrane proteins from the lipid bilayer directly, eschewing detergent entirely and permitting the study of such proteins in a 'membrane-like' lipid environment[171]. While benefits associated with conventional nanodiscs include a controlled and defined lipid composition, SMA

copolymers are, in theory, capable of maintaining many of the protein-lipid interactions that occur at the cell membrane[172].

While the majority of the density surrounding the TMD of SMA-cASIC1a channels was disordered, we observed multiple ordered elongated densities situated in lipophilic channels along the TMD in the 2.8 Å structure of the desensitized channel (**Figure 4.11a**) that we suggest may correspond to bound lipids. Separated into spatially-distinct clusters (**Figure 4.11b**), putative lipid densities reside near the top of the membrane sandwiched between TM2a and TM1 helices (**Figure 4.11c**) and near the bottom of the membrane between TM1 and TM2b (**Figure 4.11d**).

Thus far, our results have suggested that the local lipid environment is important for maintaining the architecture of the re-entrant pre-TM1 residues in ASIC1a and thus the integrity of the lower pore pathway. Therefore, the location of at least one cluster of putative lipid densities within a lipophilic cleft immediately adjacent to re-entrant loop residues and the GAS belt TM2 domain swap (**Figure 4.11d**) is intriguing, especially given that the cryo-EM structure of a full-length cASIC1a channel in an N-dodecyl-β-D-maltoside detergent micelle lacked ordered amino terminal residues[156]. However, given the molecular ambiguity of SMA-cASIC1a particles we are unable to assign this density to any specific lipid. As such, we suggest that future experiments are needed to determine the molecular composition of SMA-cASIC1a particles and to explore relevant interactions between ASICs and the plasma membrane.

Discussion

Here we present structures of an ASIC embedded in a membrane-like environment in both high pH resting and low pH desensitized conformations. While the conformation of both

resting and desensitized channels throughout the ECD faithfully mirrors those solved previously via detergent-based methods, our structures demonstrate that amino terminal residues prior to TM1 form a re-entrant loop that comprises the lower portion of the ion permeation pathway. In both resting and desensitized structures, the conserved HG motif is situated within the re-entrant loop immediately below the GAS belt TM2 domain swap where it forms a constriction along the ion permeation pathway and is stabilized by a complex network of inter and intra subunit interactions. Finally, we detected elongated ordered densities within lipophilic channels of the TMD, including adjacent to the re-entrant amino terminus, that we propose may correspond to bound lipids.

These results provide a structural basis for contributions of the amino terminus to both ion permeation and proton-dependent gating of ASICs, reveal the location of the conserved HG motif along the ion conduction pathway and expose a role for the plasma membrane in maintaining the TMD architecture of ASICs. Given the structural similarities between ENaCs and ASICs, as well as the highly conserved and functionally-important nature of the HG and GAS belt residues, these results provide detailed structural information pertaining to a pair of motifs central to gating and ion permeation and of high therapeutic relevance to the entire superfamily of ENaC/DEG ion channels.

Acknowledgements

We thank L. Vaskalis for help with figures, H. Owen for manuscript preparation and all Gouaux lab members for their support. This research was supported by the National Institute of Diabetes and Digestive Kidney Diseases (5T32DK007680), and the National Institute of Neurological Disorders and Stroke (5F31NS096782 to N.Y. and 5R01NS038631 to E.G.). Cryo-EM data was

collected at the Pacific Northwest Center for Cryo-EM and at the National Center for Cryo-EM access and Training. Additional support was provided by ARCS Foundation and Tartar Trust fellowships. E.G. is an Investigator with the Howard Hughes Medical Institute.

Tables

	pH 7.0 SMA-cASIC1a	pH 8.0 SMA-cASIC1a
Data collection/processing		
Microscope	Krios (NCCAT)	Krios (PNCC)
Camera	K2	K3
Magnification	105,000	105,000
Voltage (kV)	300	300
Exposure time (s)	7.25	2
Frames (no.)	48	50
Electron exposure (e–/Å^2)	45-50	40-50
Defocus range (μm)	-0.8 – -2.6	-0.8 – -2.6
Pixel size (Å)	1.096	0.648
Initial micrographs (no.)	3,396	1,946
Micrographs used (no.)	3,221	1,946
Particles picked (no.)	1,874,332	608,152
2D-cleaned particles (no.)	327,268	57,209
Final Refinement		
Symmetry imposed	C3	C3
Final particles (no.)	121,140	48,338
Map resolution (Å)	2.8	3.7
FSC threshold	0.143	0.143
Model statistics		
Initial model used (PBD code)	4NYK	5WKU
Model resolution (Å)	3.1	4.0
FSC threshold	0.5	0.5
Map sharpening *B* factor (Å^2)	99	121
Model composition		
Non-hydrogen atoms	10686	10242
Protein residues	1338	1338
Ligands	6	6
B factors (Å)		
Protein	69.42	32.15
Ligand	89.03	124
R.m.s. deviations		
Bond lengths (Å)	0.005	0.004
Bond angles (°)	0.834	0.807
Validation		
MolProbity score	1.29	1.54
Clashscore	3.10	5. 90
Poor rotamers (%)	0.0	0.0
Ramachandran plot		
Favored (%)	96.85	96.62
Allowed (%)	3.15	3.38
Disallowed (%)	0.0	0.0

Table 4.1: Cryo-EM data collection, refinement and validation statistics

Figures and legends

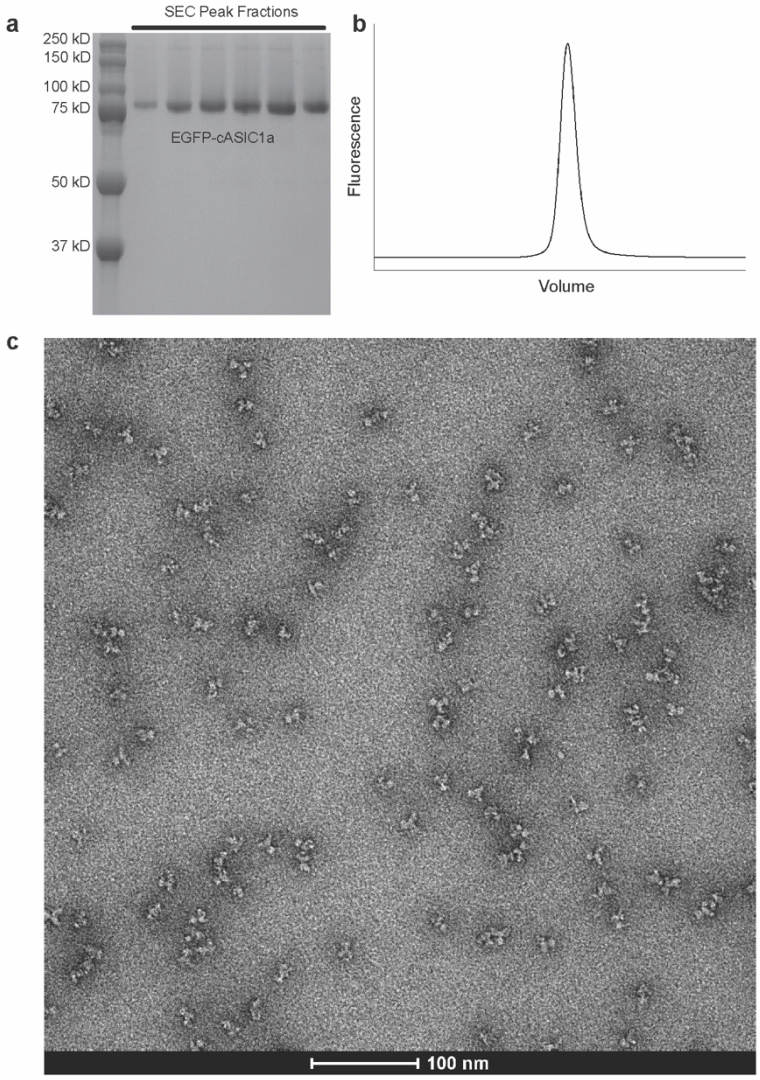

Figure 4.1. Purification of SMA-cASIC1a. a-b, SDS-PAGE (**a**) and FSEC (**b**) analysis of SMA-solubilized EGFP-cASIC1a particles after size-exclusion chromatography. **c,** Negative stain transmission electron microscopy of SMA-solubilized EGFP-cASIC1a particles.

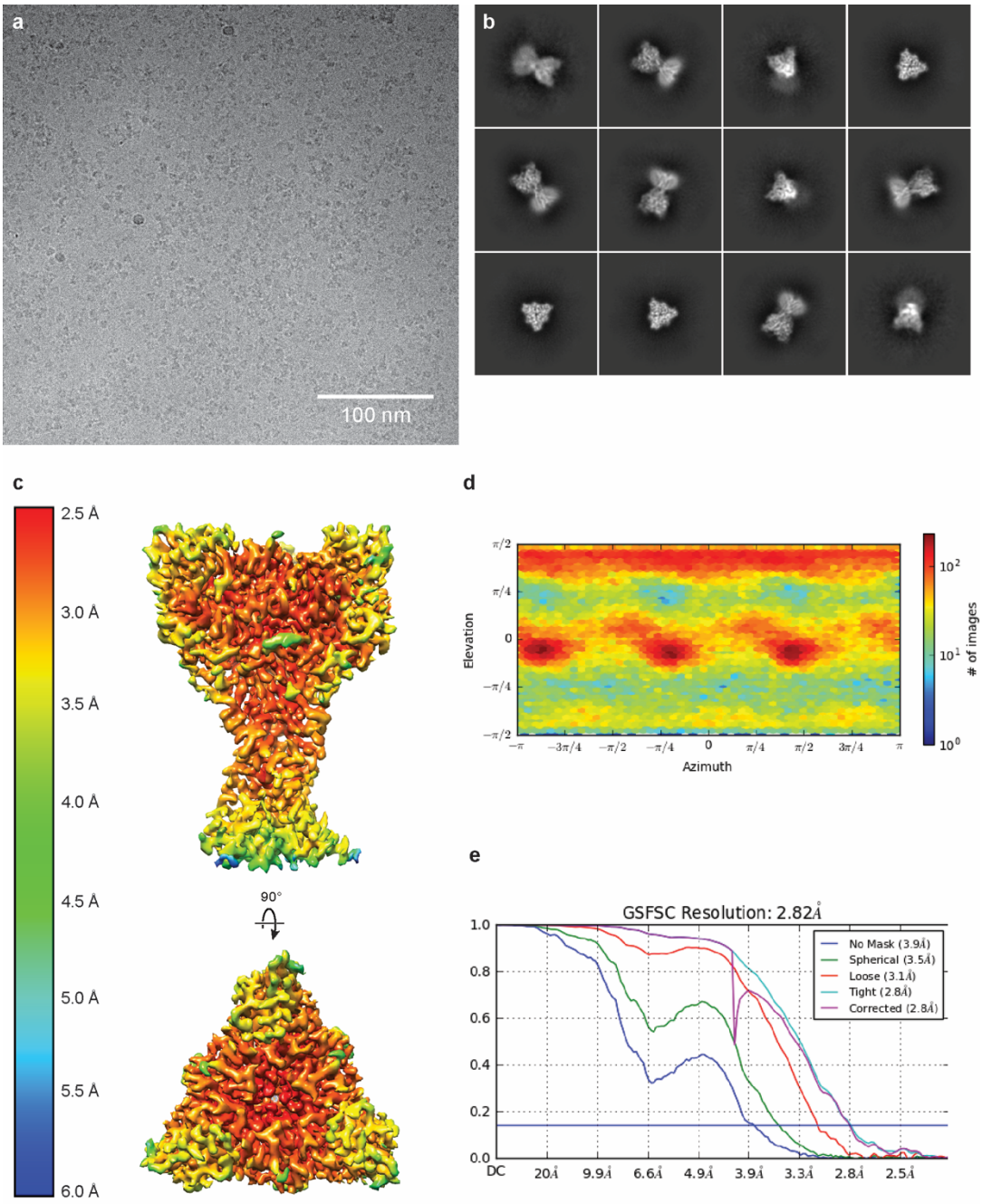

Figure 4.2. Cryo-EM of SMA-cASIC1a at pH 7.0. a-b, Representative micrograph (**a**) and 2D classes (**b**) of SMA-cASIC1a at pH 7.0. **c-e,** Local resolution estimation (**c**) particle distribution (**d**) and gold standard FSC resolution estimation (**e**) from final non-uniform refinement in cryoSPARC V2.

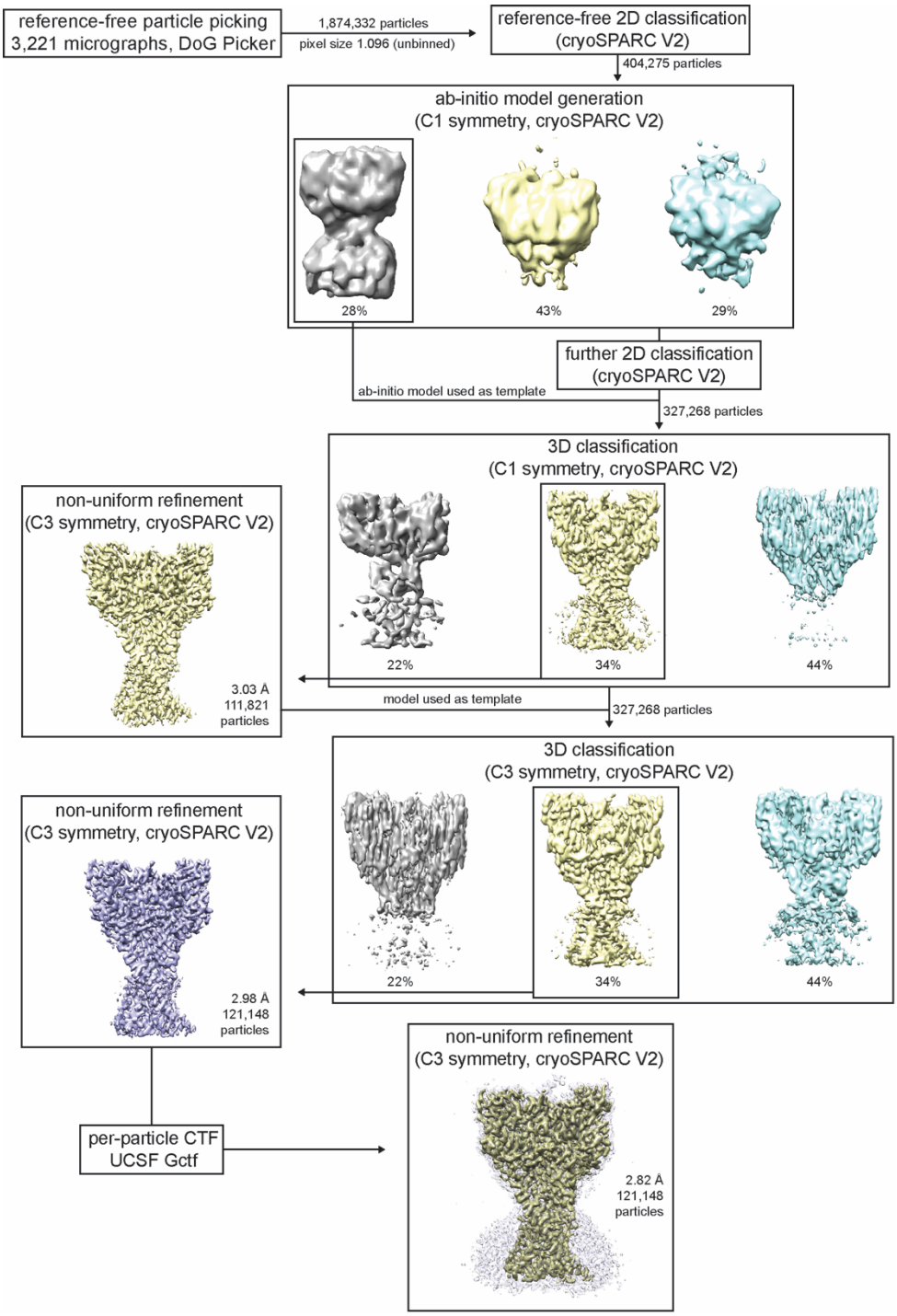

Figure 4.3. Cryo-EM data processing for SMA-cASIC1a at pH 7.0. Data processing strategy for SMA-cASIC1a pH 7.0 dataset.

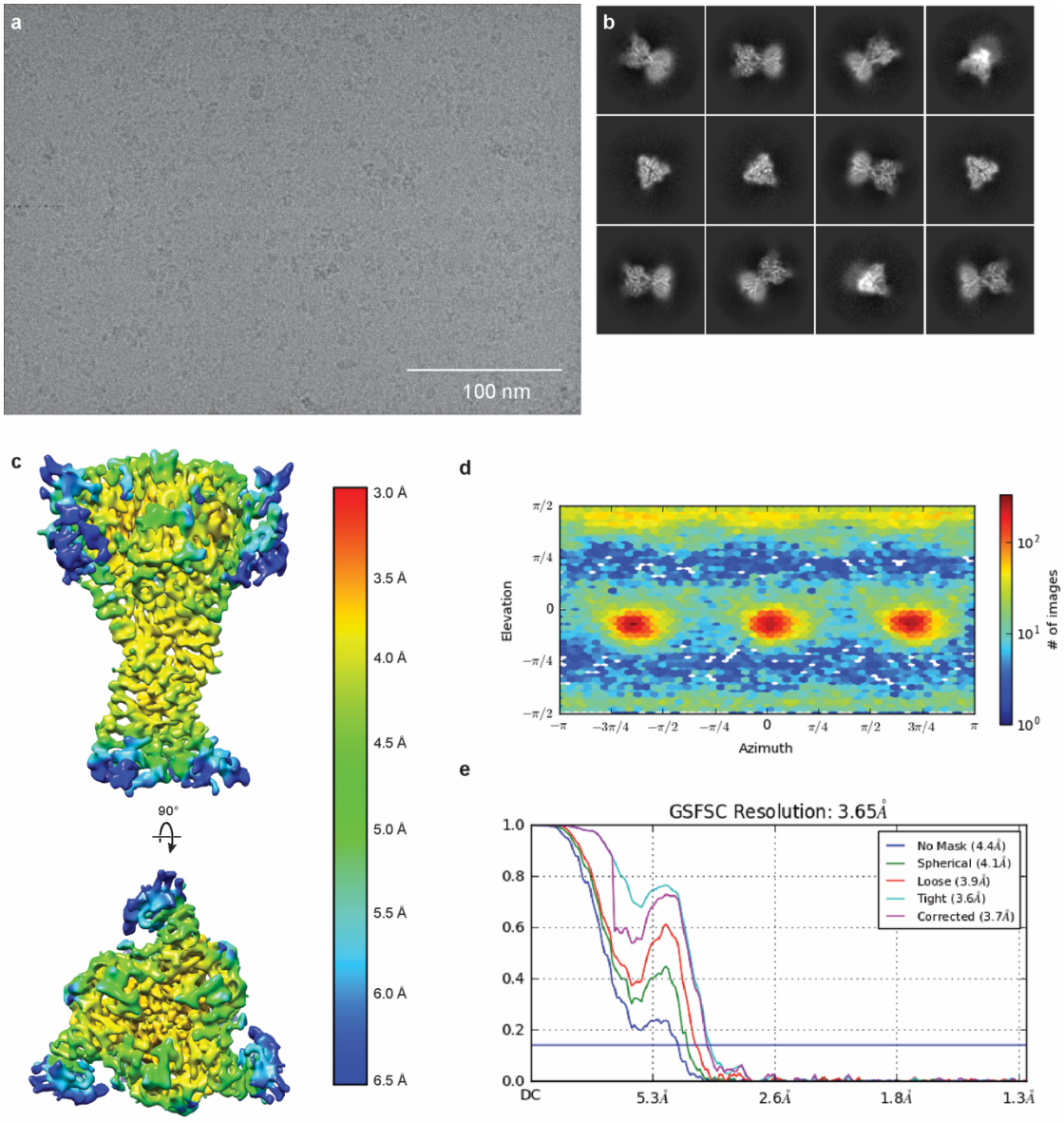

Figure 4.4. Cryo-EM of SMA-cASIC1a at pH 8.0. a-b, Representative micrograph (**a**) and 2D classes (**b**) of SMA-cASIC1a at pH 80. **c-e,** Local resolution estimation (**c**) particle distribution (**d**) and gold standard FSC resolution estimation (**e**) from final non-uniform refinement in cryoSPARC V2.

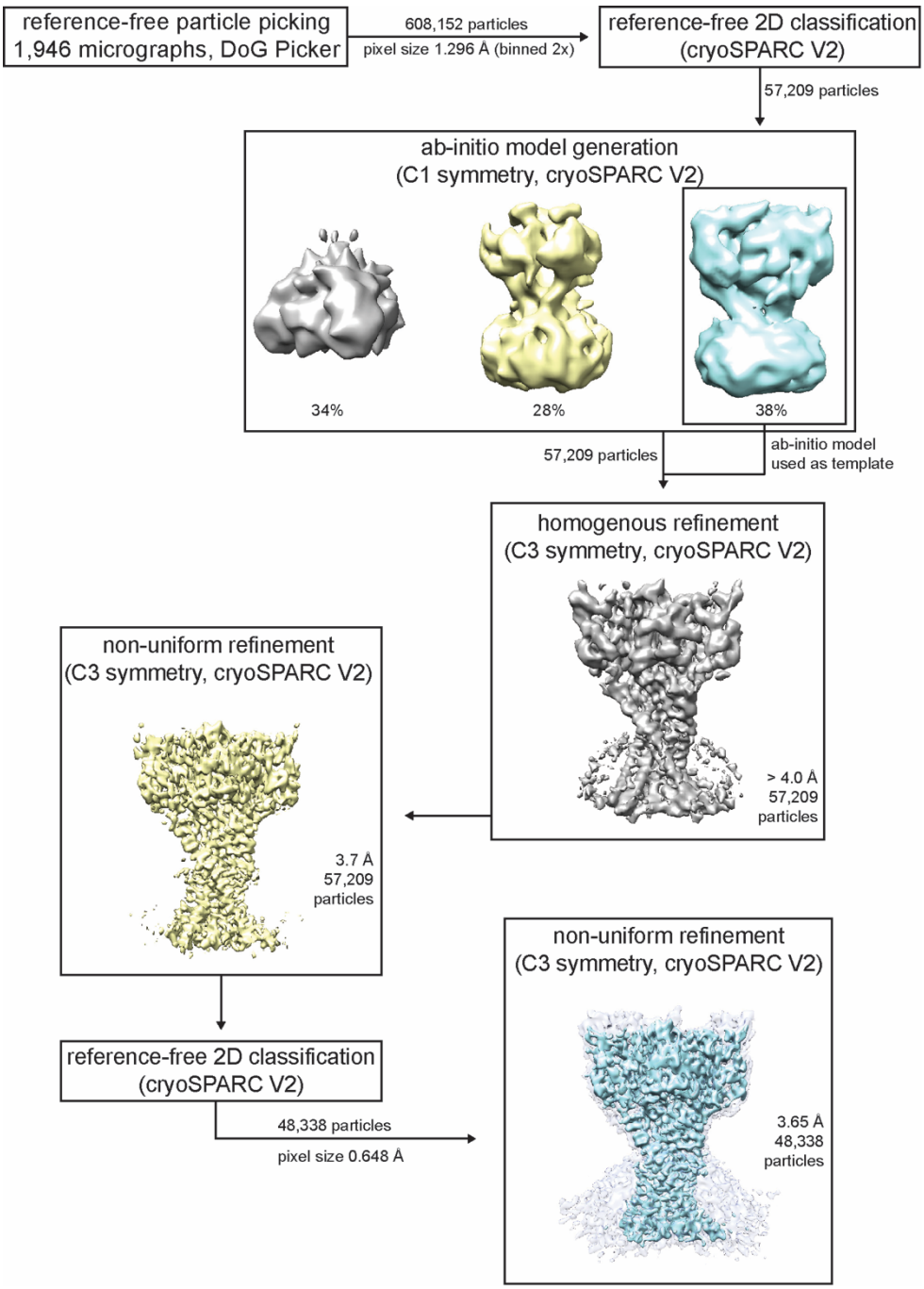

Figure 4.5. Cryo-EM data processing for SMA-cASIC1a at pH 8.0. Data processing strategy for SMA-cASIC1a pH 7.0 dataset.

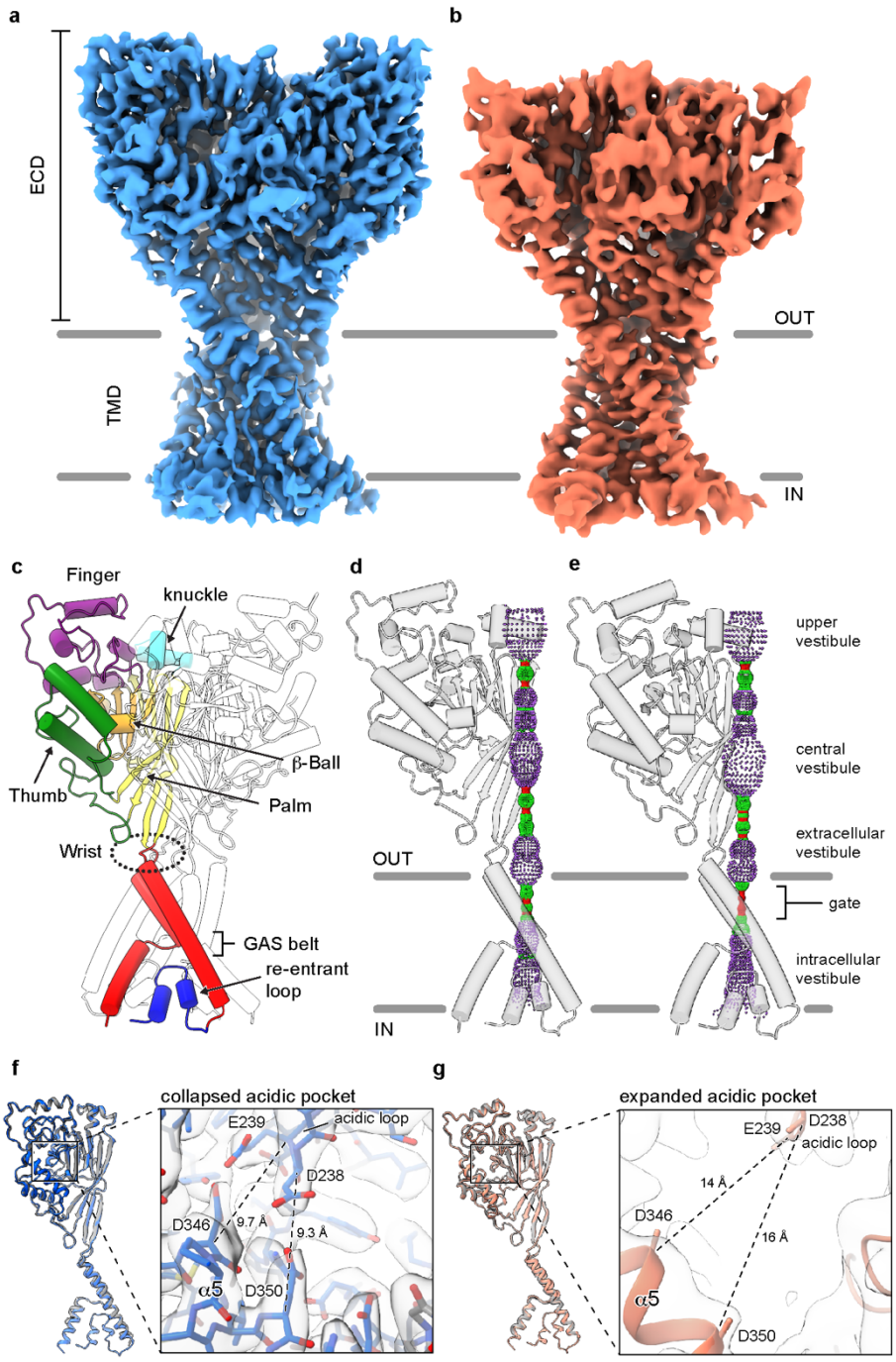

Figure 4.6. Cryo-EM structures of SMA-cASIC1a at high and low pH. a-b, Cryo-EM maps of SMA-cASIC1a at pH 7.0 (**a**) and pH 8.0 (**b**). **c,** Cartoon diagram of cASIC1a with single subunit shown colored by domain for clarity. **d-e,** Pore profiles for SMA-cASIC1a in a desensitized (**d**) and resting (**e**) state calculated with HOLE software (pore radius: red < 1.15 Å <

green < 2.3 Å < purple). **g,** Single subunit superposition of SMA-cASIC1a in a desensitized state (blue) and the desensitized state x-ray structure (PDB 4NYK, grey). Detail view of the collapsed acidic pocket shown in inset. **h,** Single subunit superposition of SMA-cASIC1a in a resting state (salmon) and the desensitized state x-ray structure (PDB 5WKU, grey). Detail view of the expanded acidic pocket shown in inset.

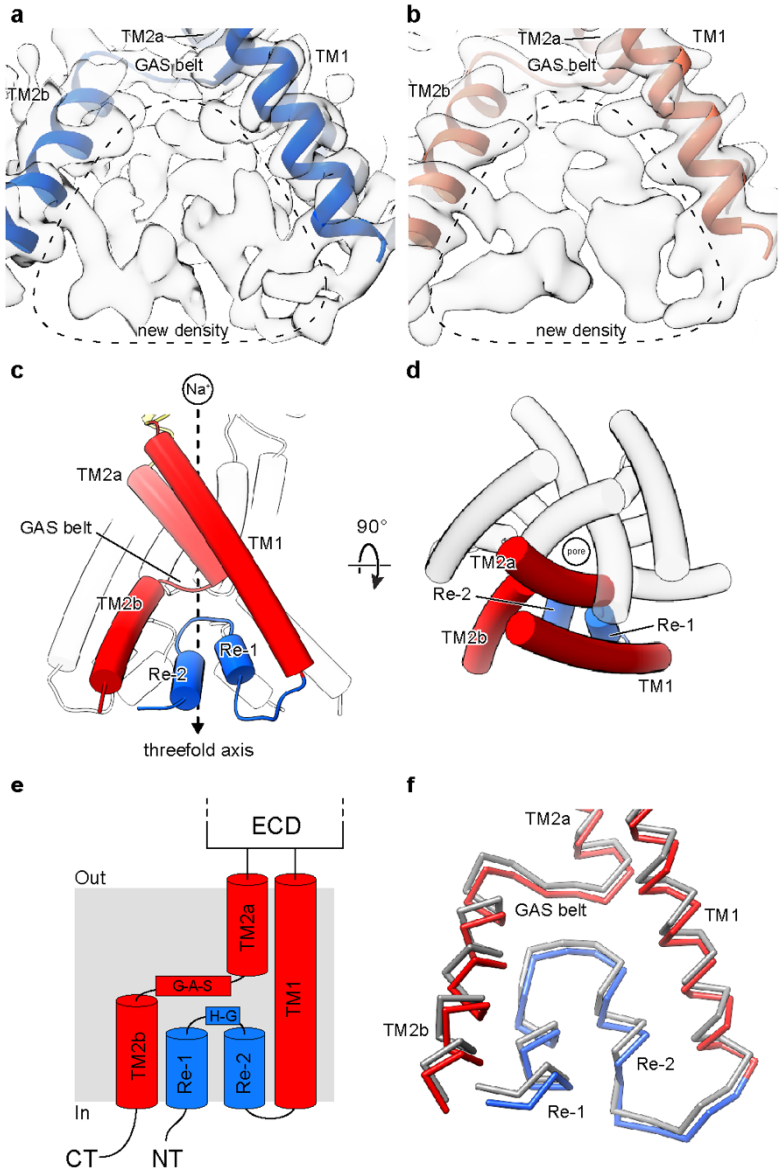

Figure 4.7. Cryo-EM density and architecture of the re-entrant pre-TM1 domain. a-b, Unanticipated cryo-EM density corresponding to amino terminal residues of SMA-cASIC1a in pH 7.0 (**a**) and pH 8.0 (**b**) reconstructions. **c-d,** Side (**c**) and top-down (**d**) views of the TMD from SMA-cASIC1a in a desensitized state at low pH. Single subunit shown colored by domain for clarity. **e,** Linear diagram depicting the transmembrane organization of cASIC1a channels. **f,** Backbone superposition of SMA-cASIC1a in desensitized (colored by domain) and resting (grey) states.

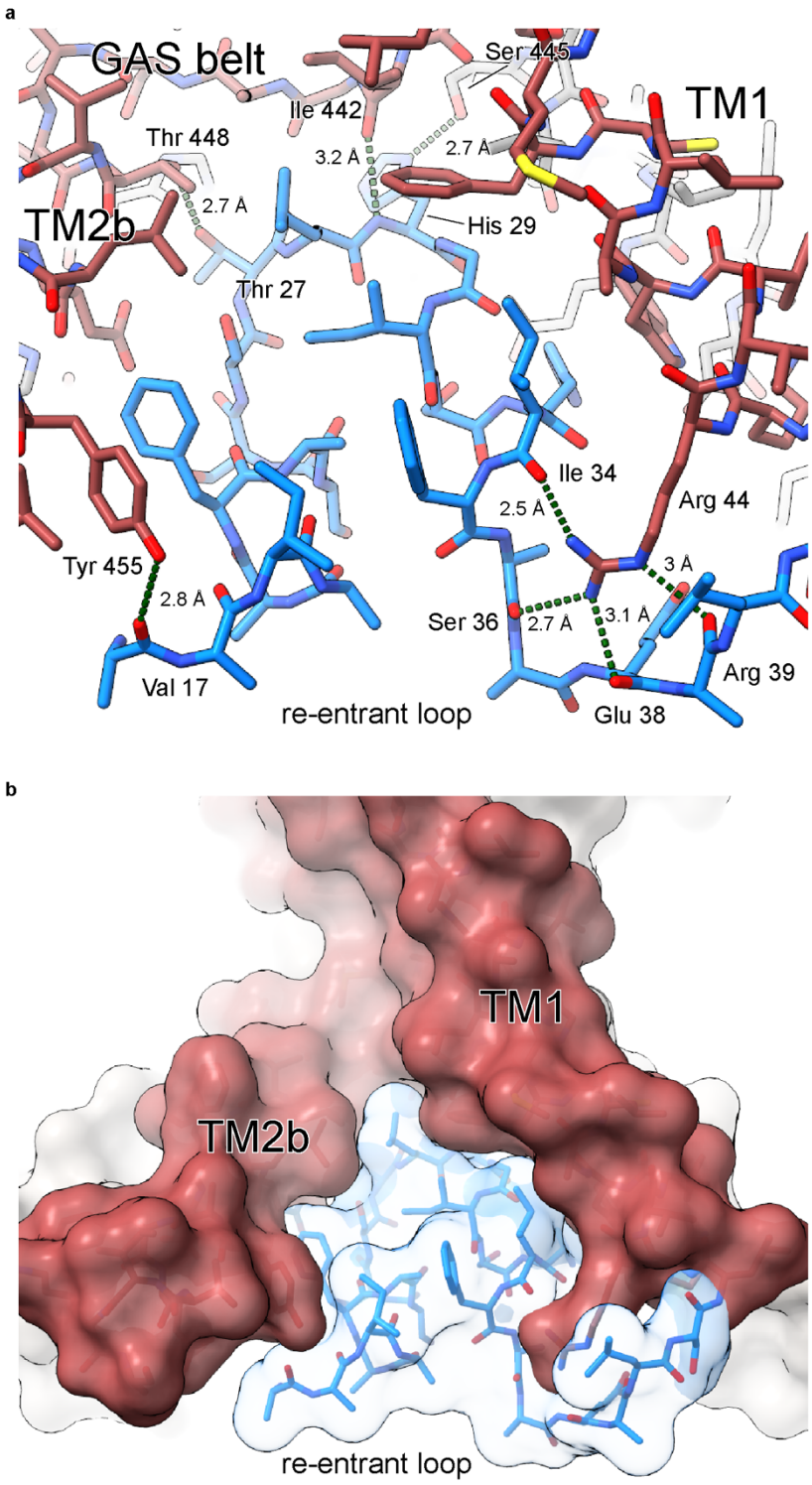

Figure 4.8. Polar contacts and domain interfaces at the re-entrant loop. a, Polar interactions between the re-entrant loop and neighboring residues. **b,** Surface representation of lower TMD showing interfaces between the re-entrant loop residues and TM1 and TM2b helices.

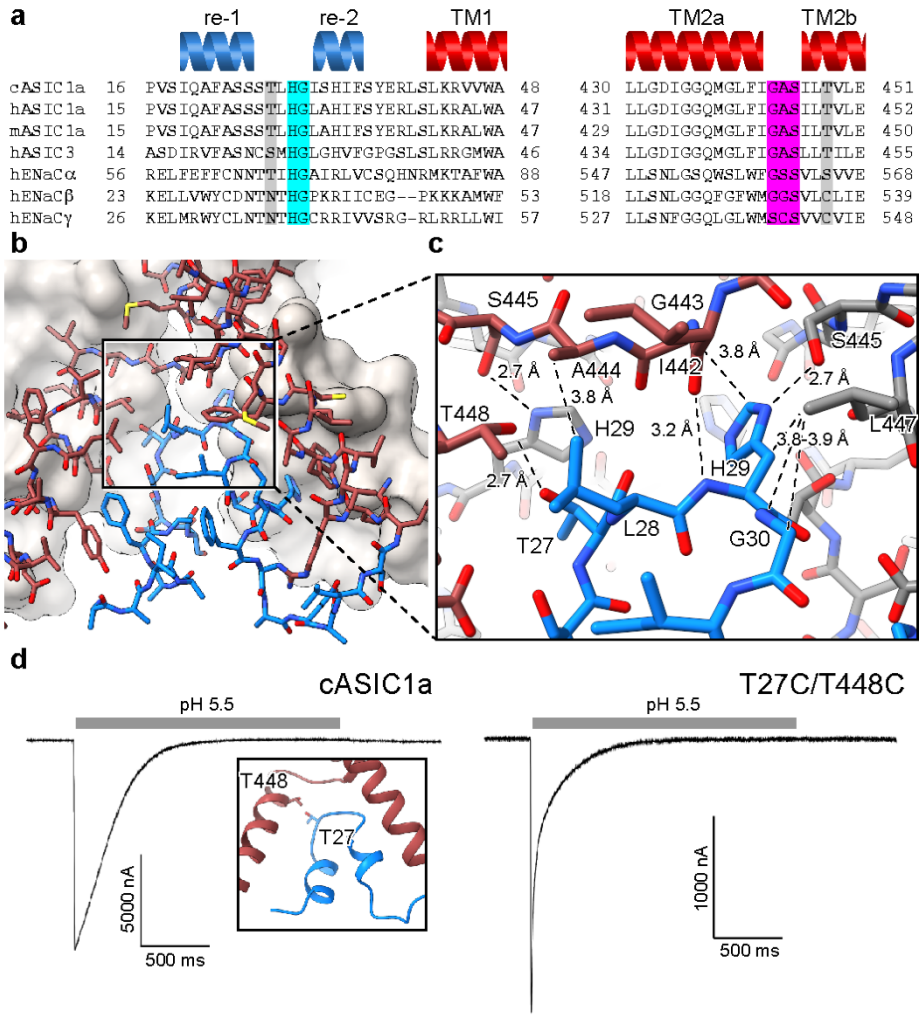

Figure 4.9. The HG motif sits at a subunit interface below the GAS belt domain swap. a, Sequence alignment of selected ASIC1, ASIC3 and ENaC channels covering the pre-TM1 and TM2 domains with GAS domain and HG motif residues highlighted in pink and light blue, respectively, and secondary structure for cASIC1a shown above. **b-c,** View of the chemical environment around the re-entrant loop (**b**) with a detail view of the GAS domain and HG motif interface (**c**). **d,** Whole-cell patch clamp recordings of cASIC1a and cysteine substituted channels with cartoon representation of cysteine substitution sites shown in inset. Data were recorded from sf9 cells infected with BacMam virus containing DNA for cASIC1a or mutant channels. Experiments were performed 5 times with similar results. Of note, for cASIC1a recordings we

observed a deviation from the typical decay kinetics of ASIC1a channels that may be due to series resistance artifacts given the large magnitude of the proton-gated currents.

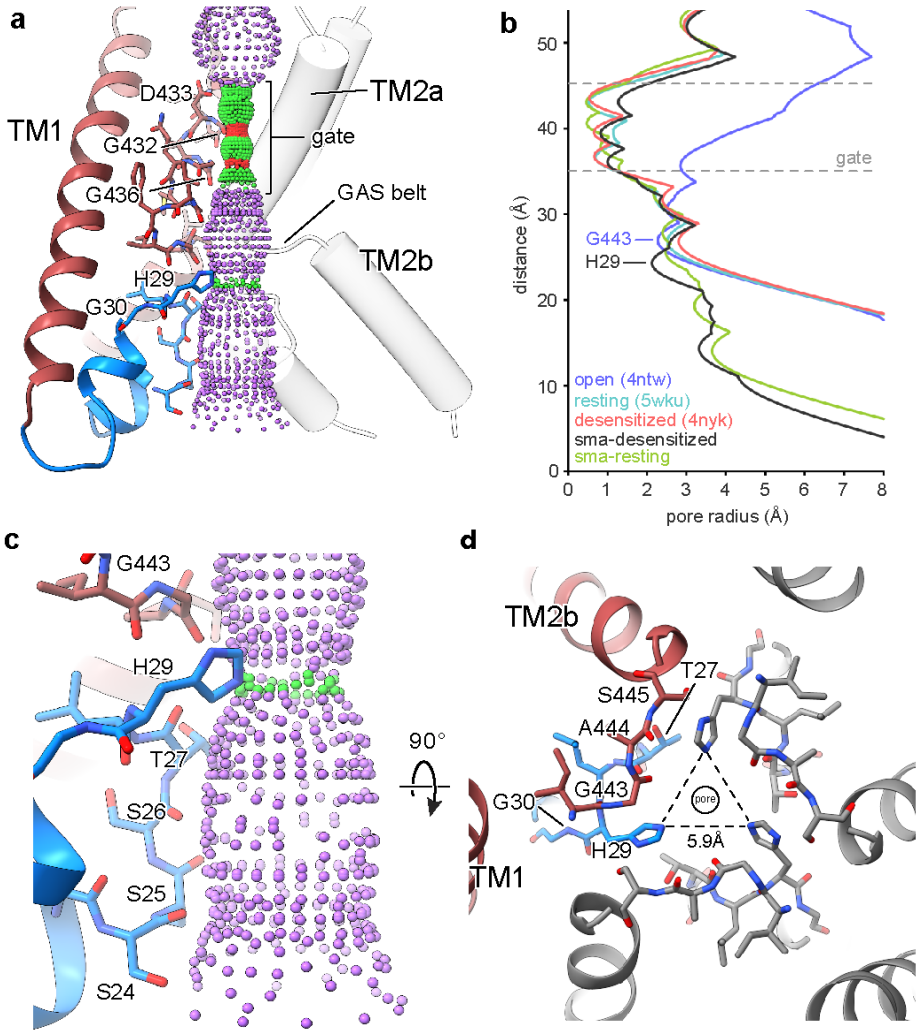

Figure 4.10. The re-entrant loop forms the lower ion permeation pathway. a, Overview of pore-forming residues of desensitized SMA-cASIC1a channels beginning at the ion channel gate. Pore profile calculated with HOLE software (pore radius: red < 1.15 Å < green < 2.3 Å < purple) is shown. **b,** Plot of pore radius corresponding to the view in (**a**) for resting (PDB 5WKU), open (PDB 4NTW) and desensitized (PDB 4NYK) x-ray and SMA-cASIC1a cryo-EM structures. **c,** Detail view of lower ion permeation pathway formed by amino terminal re-entrant loop residues. **d,** Top-down view of the primary constriction point below the ion channel gate formed by His 29 of the desensitized SMA-cASIC1a channel with GAS belt residues in the foreground.

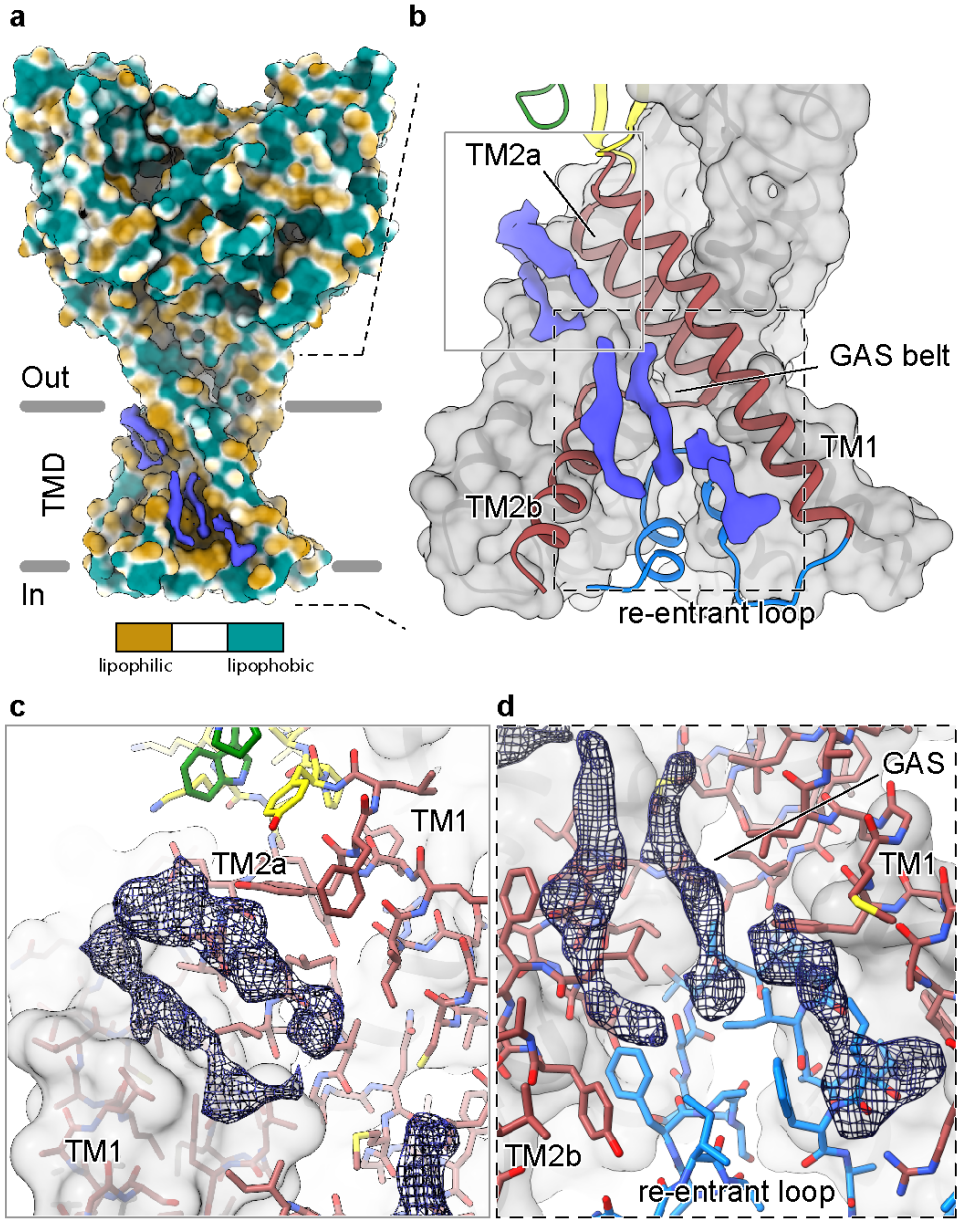

Figure 4.11. Elongated density within lipophilic channels at the TMD of SMA-cASIC1a channels. a, Surface representation of SMA-cASIC1a in a desensitized state colored by molecular lipophilicity potential calculated with pyMLP[173] in ChimeraX[174]. **b,** Hybrid cartoon and surface representation of putative lipid sites at the TMD. **c-d,** Putative lipid densities between TM1 and TM2a (**c**) and between TM1 and TM2b adjacent to the re-entrant loop (**d**) of SMA-cASIC1a.

Chapter 5

Light-coupled cryo-plunger enables time-resolved cryo-EM

The contents of chapter five will be submitted for publication in modified form:

Yoder, N., Jalali-Yazdi, F. and Gouaux, E. Light-coupled cryo-plunger enables photo uncaging of ligands and rapid vitrification. (to be submitted)

Author Contributions

N.Y., F.J.-Y. and E.G. designed the project. N.Y. designed and built the apparatus. N.Y. and F.J.-Y. tested the apparatus. N.Y. performed the protein purification and cryo-EM data collection and N.Y. and F.J.-Y. processed the cryo-EM data. N.Y wrote the manuscript and all authors edited the manuscript.

Abstract

Proteins are dynamic molecules that are capable of undergoing rapid conformational rearrangements in response to various stimuli. These structural changes are often critical to protein function, and thus elucidating such conformational landscapes has been a long-standing goal of structural biology. To harness the power of single particle cryo-EM methods to enable 'time-resolved' structure determination, we have developed an apparatus that couples flash-photolysis of caged ligands with rapid sample vitrification. The 'flash-plunger' consists of a high-power ultraviolet LED coupled with focusing optics and a motorized linear actuator, enabling the user to immobilize protein targets in vitreous ice within a programmable time window – as short as tens of milliseconds – after stimulus delivery. The flash-plunger provides the single-particle cryo-electron microscopy community with a simple, inexpensive and flexible tool to explore short-lived conformational states previously unobtainable by conventional sample preparation means.

Introduction

Proteins are ubiquitous components of our biological ecosystem and participate in a wide variety of biomolecular 'tasks' essential to nearly all physiological processes. In order to complete their biochemical duties, proteins are inherently dynamic and often undergo large-scale conformational rearrangements in response to a stimulus. Occupancy of individual functional states and the kinetics with which proteins move between them varies broadly and, given the critical nature of protein dynamics to cellular function, the elucidation of molecular structures associated with specific functional states has been an area of intense scrutiny. Ion channels in particular can open in milliseconds or less in response to agonists and move into a non-conducting inactive/desensitized conformation nearly as quickly, necessitating the use of mutagenic or pharmacological tools to study the structure of the channel's active conformation. As such, developing 'time-resolved' structural frameworks for the molecular mechanisms that underlie protein dynamics remains an outstanding goal of the structural biology field.

Despite their information rich nature, macromolecular structures provide what are inherently static 'snap-shots' of protein conformations and are devoid of biologically-relevant kinetic details. Furthermore, the successful formation of well-ordered crystals, or determining high-resolution cryo-electron microscopy (cryo-EM) reconstructions, often precludes the ability to capture transient conformational states via conventional structural means and instead selects for long-lived states. Therefore, while the wealth of information gained from the pursuit of high-resolution protein structures has contributed immensely to our understanding of biology, the lack of a meaningful correlation to kinetics represents a substantial gap in our understanding of protein structure/function relationships.

Given the inherent limitations of x-ray crystallography imposed by the crystal lattice, cryo-EM has become the favored technique for exploring time-resolved macromolecular structural changes, particularly in light of recent advancements in data processing algorithms aimed at parsing conformational heterogeneity in cryo-EM data[175,176]. Indeed, no special equipment is required to study slower structural transitions – such as those that occur on the order of tens of seconds or more – via cryo-EM. Rather, the user simply freezes grids at defined timepoints following the initiation of a reaction[177]. However, to study conformational changes within a time window of seconds or faster, such as those associated with activation and inactivation of some ion channels that occur on the order of single to tens of milliseconds, special techniques are needed to overcome the temporal limitations unavoidable in conventional cryo-EM sample preparation, including both blotting and sample handling delays.

A notable example of applying time-resolved cryo-EM to study rapid conformational changes in macromolecular structures was the landmark study on nicotinic acetylcholine receptors (nAChR) by Nigel Unwin and John Berriman[30,178,179]. Even though nAChRs open in microseconds and undergo desensitization within tens of milliseconds in the presence of acetylcholine[180], Unwin and Berriman were able to capture the receptor in both closed and open states by developing techniques to spray acetylcholine on cryo-EM grids immediately prior to vitrification. The spray-plunge technique has since evolved to encompass multiple approaches and apparatuses, from designs expanding upon Unwin and Berriman's initial method of spraying ligand onto a sample suspended on a cryo-EM grid[30], to recent developments aimed at mixing reactants prior to spray application[181-186]. Depending on the method used and the details of the experimental setup, temporal resolution down to single milliseconds is theoretically attainable. However, spray-plunging methods are not without downsides, as control over ice thickness, an

increase in the air-water interface as well as highly specialized equipment requirements all represent ongoing challenges.

In addition to spray-plunging methods, light has also been explored as a method to catalyze conformational changes for cryo-EM studies[187-189] and has been particularly successful in electron diffraction experiments[190,191]. These early 'flash-plunge' setups employed high-output flash-lamps coupled to liquid light guides and custom manual plunge apparatuses to vitrify samples following light exposure. However, despite the initial promise of light-based time-resolved cryo-EM methods and the aforementioned success when used in conjunction with electron crystallography, the approach has seen comparatively little development.

Whether used to study light-sensitive proteins, photo-uncage ligands or to perform photo-switching experiments, light is an attractive mechanism with which to initiate chemical reactions due to its immediate delivery and minimal sample perturbation. Furthermore, leveraging photolabile compounds has been instrumental in the study of many biological systems and has met with particular success in the field of neuroscience research[192-196]. As such, the chemistry of photolabile neuroactive compounds has seen significant development and many neurotransmitters such as ATP[197], GABA[198], glutamate[199], 5-HT[200], and dopamine[201] are commercially available today.

Here, we present a light-coupled cryo-plunger for time-resolved cryo-EM that utilizes light delivery to facilitate photochemical reactions in a sample suspended on a cryo-EM grid, immediately prior to sample vitrification. Furthermore, we demonstrate that LED-based UV irradiation is sufficient to uncage protons on a tens of millisecond time scale, driving large-scale conformational changes in an acid-sensing ion channel (ASIC) on a cryo-EM grid. This simple but robust system is easy to assemble and use, requires less than a square meter of lab space and

is fully adaptable to fill a variety of unique experimental requirements. As such, our flash-plunger represents an accessible and broadly applicable platform for time-resolved cryo-EM studies.

Materials and methods

Flash-plunger components: A general overview of the device can be found in the first section of this work. The major components that comprise the apparatus are as follows: (1) 100 mm stroke multi-phase 6 coil linear actuator with built in 5 μm encoder (LCA25-100-35-6, SMAC); (2) single axis brushless motion controller with built in amplifier (LCC-10, SMAC), an RS232 Kit (SMAC) and DB26HD breakout board (CZH Labs); (3) 240 W power supply (S8VK-G24048, Omron Automation); (4) high-power 365 nm UV LED (SOLIS-365C, Thor Labs) controlled by an LED driver (DC2200, Thor Labs) and equipped with an aspheric condenser lens AR-coated for 350-700 nm (ACL50832U-A, Thor Labs) housed in 2-inch lens tubes (Thor Labs). The linear actuator was affixed to a stainless-steel breadboard via a large diameter aluminum post (Spindle and Hoyer) and the LED and optical components were affixed to the breadboard via a three-axis manual micromanipulator (1680 XYZL, Siskiyou). The ethane/propane mixture was contained in a brass cup from an old-model Vitrobot (ThermoFisher Scientific) and housed within a small foam vessel (FD-500, SpearLab). Other electrical components included a breadboard connected to a momentary foot switch and affixed with three momentary push-buttons as well as a circular white LED for post-vitrification illumination of the working space (144W-ZK, AmScope). All programming, tuning and testing of the motion parameters was done in LCC Control Center V2.0.1 (SMAC) or MotionLab V1.8.1.0 (SMAC).

Certain components of the system were 3D printed in house on a large-format FDM 3D printer (N2Plus, Raise3D) using PLA or ABS filament. 3D printed parts include the adapter connecting the tweezers to the actuator piston, as well as numerous mounting brackets for components including the ethane/propane mixture, motion control board, linear actuator, breadboard/breakout board and foam cryogen container.

Flash-tests with caged compounds: A 2 µl sample containing 20 mM MNPS.Na, 5 mM Tris pH 8.0, 150 mM NaCl, 10 µM SNARF-4F was applied to a holey carbon grid held in self-closing tweezers (5376-NM, Pelco) and irradiated via UV LED. The sample was diluted to 10 µl total volume in a sub-micro fluorometer cuvette (701MFLUV10.10B, FireflySci) and emission spectra were recorded (Ex. 543 nm) on a UV-VIS spectrofluorophotometer (RF-5301PC, Shimadzu). The ratio of emission peaks at 642 and 586 nm (R642/586) was calculated and final pH values interpolated using a calibration curve generated using pH-adjusted buffer containing 80 mM Tris, 40 mM MES and 10 µM SNARF-4F. Experiments for standard curve data as well as all flash tests were performed in triplicate. The caged proton source MNPS.Na was synthesized by the medicinal chemistry core at OHSU.

For glutamate uncaging, 1 mM MNI-glutamate samples in water were prepared in a dark room. A 4 µl sample was applied to a holey carbon grid as described above and irradiated via UV LED. Following irradiation, a 2 µl sample was removed and diluted to 98 µl for HPLC-based measurement of uncaged glutamate.

Motion and illumination analysis: Given the short duration of irradiation as well as the velocity profile of the plunging grid, we used a camera capable of collecting 1000 frames per second (fps) modified to accept aftermarket lens systems (RibCage RX0 camera, Sony; Voightlander Nokton

17.5 mm f/0.95 lens). Recordings were collected at 1080p/1000 fps and movies were analyzed frame-by-frame in Premier Pro (Adobe).

Ray trance analysis for design and optimization of the lens system was performed using FRED optical engineering software (Photon Engineering). LED power was measured at the grid with a wireless power meter (PM160T-HP, Thor Labs) set to 365 nm.

Expression and purification of ASICs: Isolated membrane fractions containing recombinant full-length chicken ASIC1a (gallus gallus) containing an N-terminal 8x His enhanced green fluorescent protein (EGFP) tag were prepared as previously described[156]. For control and 1000 mA flash experiments, membrane pellets were dounce homogenized and solubilized in tris-buffered saline (TBS) containing 2% (w/v) SL300010 (polyscope) styrene-maleic acid copolymers. Membrane debris was removed via centrifugation and SMA-cASIC1a particles were bound in batch to Ni-NTA beads overnight at 4°C and in the presence of 10 mM imidazole.

The following day, SMA-cASIC1a particles were eluted from an XK-16 column with TBS containing 250 mM imidazole. Peak fractions were pooled and concentrated to ~ 5 mg/ml and the 8x-His EGFP tag was removed via thrombin digestion (1:25) overnight at room temperature (RT). Following tag removal, SMA-cASIC1a particles were subjected to size-exclusion chromatography (superose 6 increase) with a mobile buffer containing TBS with 1 mM dithiothreitol (DTT). Peak fractions were concentrated to 1 mg/ml for cryo-EM sample preparation.

For samples flashed at 3000 mA LED current, cASIC1a membranes were dounce homogenized in TBS with 1% (w/v) digitonin and membrane debris was removed via centrifugation. Subsequent purification of digitonon-cASIC1a occurred as described above but with some notable exceptions. First, digitonin-cASIC1a particles were bound to Ni-NTA beads

in batch for 1.5 hours at 4°C. Second, the 8x-His EGFP tag was removed from digitonin-cASIC1a particles via thrombin digestion (1:50) for 1 hour at RT. Finally, purification buffers for digitonin-cASIC1a were identical to those detailed for purification of SMA-cASIC1a but contained 0.1% (w/v) digitonin. Purified digitonin-cASIC1a sample was used for flash-plunge grid preparation at 5 mg/ml.

Sample preparation for cryo-EM flash-plunge experiments: All flash-plunge experiments took place in an environmentally controlled room maintained 4°C and 60-70% humidity. MNPS.Na was added to each sample to achieve a final concentration of 20 mM. 200 mesh Au Quantifoil holey carbon grids – R1.2/1.3 for un-flashed ASICs, R2/2 for 1000 mA-flashed ASICs, and R2/1 for 3000 mA-flashed ASICs – were glow-discharged for 1 min at 15 mA carbon side up and pre-cooled to 4°C.

A 4 µl sample was applied to the carbon side of a glow-discharged grid and blotted by hand using pre-cooled filter paper (Whatman, grade 1). The sequential 'flash-then-plunge' method described above was used to vitrify all samples in an ethane/propane mixture. A 25 ms flash was used for all grids and LED current was varied to set irradiation levels, resulting in a total time of ~ 70 ms between blot and vitrification. For control grids that were not irradiated, the LED current was set to 0 mA to maintain a constant time interval.

Cryo-EM data collection: Cryo-EM data were collected on a Titan Krios cryo-electron microscope (ThermoFisher) operated at 300 kV. Images were recorded on a Gatan K3 camera positioned after an energy filter (20-eV slit width) operating in super-resolution mode with a binned pixel size of 0.83 Å. Data were collected using SerialEM and dose-fractionated to 50 frames for a total exposure time of 2-3 s and a total dose of 40-50 e^{-} $Å^{-2}$.

Cryo-EM data processing for ASICs: Images were motion-corrected with UCSF MotionCor2 and defocus values were estimated with Gctf for 1000 mA-flashed ASICs or patch CTF estimation in cryoSPARC V2 for 3000 mA-flashed ASICs. Particles were picked using DoGPicker and reference-free 2D classification was performed in cryoSPARC. For 3000 mA-flashed particles a second round of particle picking was performed using initial 2D classes as templates. Following 2D classification, ab-initio model was generated in cryoSPARC and particles were subjected to iterative rounds of 3D classification and refinement, also in cryoSPARC. Final reconstructions were obtained via non-uniform refinement (C3 symmetry) in cryoSPARC for control particles or in Relion 3.0 for 1500 mA-flashed particles.

For 3000 mA-flashed particles, particle subtraction was performed in cryoSPARC V2 using a mask that removed signal from density corresponding to either the micelle or to the micelle and the TMD. Local refinement (C1 symmetry) was then performed on the subtracted particle stack to obtain reconstructions of the ECD alone or of the entire channel.

Results

Theory and design of the flash-plunge apparatus

The flash-plunger consists of two primary components, a motorized linear actuator mounted vertically above a foam cryogen container, and a high-power LED light source mounted perpendicular to the motion axis of the actuator (**Figure 5.1**). To maintain optimal alignment of components and facilitate easy transport into a variety of environments, such as a laboratory cold room, the flash-plunger is fully self-contained and is housed on an aluminum breadboard. Both the LED and the linear actuator are under the electronic control of a single motion control board, which is programmed and under control of the user (**Figure 5.2**).

In the flash-plunge setup, three pushbuttons and a simple foot switch allow the user to select a desired vitrification protocol and to proceed through the selected protocol, respectively (**Figure 5.3**). Programmable digital input pins detect user input via pushbutton during the experimental session, allowing for up to three independent protocols to be selected on a grid-by-grid basis without re-programming or re-initializing the system. Such control enables the user to explore the structural states of a sample at multiple defined timepoints post-photochemical reaction within a single grid preparation session. Moreover, the motion control board provides a central node of communication for the entire system, allowing the apparatus to be operated independently of a computer.

LED light source

To catalyze photochemical reactions within a short time window, we use a high-power LED emitter capable of providing greater than three watts of output power (365 nm), measured at the grid. Photons exit the UV LED as a ~ 2-inch diameter collimated beam, passing through a 50 mm wide aspheric condenser lens that focuses the photons onto the cryo-EM grid (**Figure 5.4a-b**). While optimizing beam dimensions and maximizing power delivery to the grid, this 'high-power' setup necessitates short working distances between lens and grid. For photochemical reactions requiring fewer photons, however, an alternate lens system may be used which provides a more diffuse beam that markedly increases the working distance (**Figure 5.4c-d**).

Caged compounds are often designed to be sensitive to specific wavelengths of light and, given differences in quantum yields and compound concentration requirements, experiments will likely have unique irradiation needs. To accommodate a wide array of potential experiments we have designed the LED component of the flash-plunge system to be fully modular, allowing the

user to easily swap LEDs without making substantial adjustments to the rest of the platform and thus providing access to a wide variety of commercially available light sources. Furthermore, while transistor-transistor logic (TTL) signals from the motion control board switch the LED on or off, power output is fully scalable by varying the LED current via the LED's driver, allowing the user to easily tailor the LED output to their experimental requirements (**Figure 5.2, 5.3**).

Protocol design for photo-uncaging and vitrification

Control over the interval separating sample vitrification from the initiation of a conformational change is an essential aspect of time-resolved cryo-EM. In our flash-plunge system, the user sets the desired irradiation time by programming the behavior of a general-purpose digital output pin which switches the LED on or off via a TTL signal. Additionally, the motion profile of the linear actuator, including but not limited to piston start/stop position, timing, acceleration/deceleration and velocity is fully programmable via the user interface (UI). Therefore, the length of the light exposure and the time between exposure and vitrification are under the user's control and easily specified via the UI.

In addition to programmable light exposure and plunge times, the system can accommodate multiple light exposure and vitrification approaches. For projects requiring substantial irradiation, a sequential 'flash-then-plunge' protocol (**Figure 5.5a**) will maximize light exposure at the expense of temporal resolution. Given the size and positioning of the optical components as well as the speed of the linear actuator, the temporal resolution of this method is currently limited to tens of milliseconds.

Alternatively, the desired photochemical result may be achieved by simply plunging a blotted grid through the path of a continuous beam (**Figure 5.5b**). Depending on the distance between the beam path and the cryogen, as well as the user-defined motion profile of the linear

actuator, adopting this exposure method improves temporal resolution to single milliseconds, thus approaching the limitations set by the formation of vitreous ice[202]. Notably, this approach will provide less irradiation than the aforementioned 'flash-then-plunge' approach, limiting its usefulness to projects that require fewer photochemical events to achieve a desired conformational change.

Photolysis of caged compounds

To demonstrate the capabilities of the flash-plunge apparatus to facilitate photochemical reactions on a cryo-EM grid, we used UV radiation to release either glutamate from 4-methoxy-7-nitroindolinyl caged L-glutamate (MNI-glutamate)[203] or protons from 2-methoxy-5-nitrophenyl sulfate sodium (MNPS.Na)[204] (**Figure 5.6**). Generating a pH drop in a buffered system such as tris-buffered saline (TBS) via photolysis represents a complex and challenging task for at least two primary reasons: first, generating a pH drop in buffered systems necessitates a greater number of photochemical events when compared to non-buffered systems such as those encountered in ligand uncaging or photo-switching applications, and second, caged proton compounds are not widely available and absorbance values are confined to the UV range (**Figure 5.6a**), limiting the available options for high-power light sources. Given these realities, we propose that photochemically altering the pH of TBS represents a particularly demanding task for the flash-plunge apparatus and thus serves as an extreme test of the system's capabilities, while uncaging glutamate serves as a more representative experiment.

We began the 'pH drop' experiments by first simply measuring the capacity of the photolyzed caged proton source to decrease the pH of a droplet of mildly buffered solution on an EM grid. To do this, we employed 20 mM of MNPS.Na (final concentration) in a solution of 5 mM Tris pH 8.0, 150 mM NaCl and exposed the solution to 365 nm UV radiation. Sample pH

was then assayed using a UV-VIS spectrofluorophotometer and the pH-dependent probe SNARF-4F, which harbors a characteristic ratiometric and pH-dependent emission spectrum when excited with 543 nm light (**Figure 5.7**). At the maximum current supported by our LED, exposure to UV radiation was sufficient to decrease the pH of the sample from ~ 8.0 to near 6.0 in 15 ms, and to pH 5 in 25 ms (**Figure 5.6b**). Alternatively, we were also able to titrate the pH drop by varying the LED current while maintaining a constant exposure time of 25 ms (**Figure 5.6c**).

To assess the capacity of our apparatus to uncage compounds more commonly used in biological experiments, we tested the flash-plunge device with MNI-glutamate, a caged compound regularly used for photo-activation of *N*-methyl-D-aspartate (NMDA) and α-amino-3-hydroxy-5-methyl-4-isoxazolepropionic acid (AMPA) glutamate receptors in electrophysiological recordings[205-208]. To this end, we exposed solutions containing 1 mM MNI-glutamate to UV radiation for 25 ms while varying the LED current (**Figure 5.6d**). Photolysis efficiency was assessed via HPLC analysis of the resulting grids and the extent of glutamate release was ~50% for a 1500 mA flash and over 90% for a 4500 mA flash. Because the EC_{50} values for glutamate activation of NMDA and AMPA receptors are in the low micromolar range, the initiation of receptor activation will likely require substantially less irradiation than the values tested here.

To test the effects of UV irradiation on biological samples immobilized on a cryo-EM grid, we flashed grids containing apoferritin in TBS with UV light immediately prior to vitrification in a liquid ethane/propane mixture. To mimic the conditions tested in our photolysis experiments, we irradiated grids for 25 ms with the LED set to either 10% (450 mA), 30% (1350 mA) or 100% (4500 mA) power. Ice quality and particle distribution were not noticeably

impacted for 10% or 30% power flashed when compared to control grids (**Figure 5.8a-f**). Grids exposed to full high-power irradiation from the UV LED, however, showed obvious detrimental impacts including much thinner ice, higher background signal and fewer particles (**Figure 5.8g**).

Given that our flash-plunge system is capable of releasing sufficient protons from MNPS.Na to substantially alter the pH of a buffered system by ~3 pH units at high power, and that moderate irradiation is capable of releasing ~ 500 μM glutamate in 25 ms, we propose that the apparatus is capable of photochemically modifying many commonly available caged and photo-switchable compounds and thus will be applicable to a wide variety of projects. Moreover, flashed apoferritin grids confirmed that sample and grid quality did not suffer when exposed to low to moderate levels of radiation from the UV LED.

Photo-uncaging protons drives conformational changes in a ligand-gated ion channel

Acid-sensing ion channels (ASICs) are proton-gated members of the epithelial sodium channel/degenerin superfamily of ion channels[35,128]. ASICs occupy a non-conducting resting state at high pH, open in response to low pH exposure, and enter a long-lived proton-bound but non-conducting desensitized state tens to hundreds of milliseconds following channel activation[54]. Proton-dependent structural rearrangements in ASICs are well documented and have been captured previously by both single-particle cryo-EM[156] and x-ray crystallography[20,55-57,101]. Therefore, a recapitulation of the pH-dependent conformations in ASICs by photo-uncaging of protons serves as a test of the efficacy and applicability of the flash-plunge system to biologically-relevant and biochemically-challenging projects.

To this end, we added 20 mM MNPS.Na to isolated ASICs purified at high pH and exposed the sample to UV radiation prior to vitrification on holey carbon cryo-EM grids. Each sample was irradiated following the aforementioned 'flash-then-plunge' technique (**Figure 5.5a**).

For these experiments, LED current was set to either 0, 1000 or 3000 mA and exposure time was kept constant at 25 ms, yielding a final pH of either ~ 8.0, 7.0 or 6.0, respectively (**Figure 5.6c**). For all experiments there was a ~ 70 ms interval between initial UV exposure and vitrification.

ASIC particles not exposed to UV radiation (Yoder and Gouaux, to be submitted) occupy a high pH resting conformation (**Figure 5.9a-b**) characterized by an expanded acidic pocket and a gate closed to ion permeation that mirrors existing x-ray and cryo-EM structures of ASIC1a in a high pH resting state[156]. Similarly, channels that were subjected to a 1000 mA flash – ostensibly reducing the pH to 7.0 (**Figure 5.6c**) – also retained a high pH resting state conformation (**Figure 5.9c-d**, **Figure 5.10**), indicative of insufficient channel activation and unsurprising given a pH_{50} of ~ 6.7 for chicken ASIC1a[20]. In contrast, channels exposed to a 3000 mA flash –bringing the pH to an estimated value of 6.0 (**Figure 5.6c**) – primarily occupy a low pH desensitized conformation (**Figure 5.9e-g, Figure 5.11**), characterized by a proton-bound collapsed acidic pocket (**Figure 5.9h**) and a characteristic arrangement of the channel's β11-β12/β1-β2 linkers unique to desensitized conformation (**Figure 5.9i**)[56,57].

Ultimately, particle distribution deteriorated when LED current was raised to 3000 mA, resulting in densely packed regions and clusters at the hole edges rather than an even distribution (**Figure 5.9e**). Accordingly, map quality suffered and the transmembrane domains were not well resolved in our reconstructions of the entire channel (**Figure 5.9f**). Interestingly, focused refinements including only the extracellular domain (ECD) showed improved map quality (**Figure 5.9g**) and confirmed the unique structural features at the ECD that correspond to proton-bound (**Figure 5.9h**) and desensitized (**Figure 5.9i**) channels solved previously[55-57]. Unfortunately, we were unable to capture a proton-bound open channel conformation with these

experiments, demonstrating a necessity for greater temporal resolution to capture isolated ASICs in a proton-activated state.

These results demonstrate that our flash-plunge system is capable of generating meaningful conformational changes in samples immobilized on cryo-EM grids and that moderate light exposure does not prohibit structure determination for even challenging membrane proteins. Of note, at high irradiation levels – such as those provided by a 3000 mA flash – we observed a degradation of particle quality that hampered, but did not prevent, structure determination. Therefore, while the amount of light applied to a grid to facilitate photochemical reactions harbors the potential for undesirable side effects, neither formation of vitreous ice nor structure determination is precluded by exposing blotted grids to even substantial UV radiation.

Discussion

Here we present an apparatus that couples light delivery and sample vitrification to observe time-resolved structural changes by cryo-EM. In our system, delivery of photons from a high-power LED light source to a sample immobilized on a cryo-EM grid initiates photochemical reactions that catalyze protein conformational changes captured by rapid vitrification. The majority of the components that comprise the flash-plunge apparatus are inexpensive, commercially available and require very little expertise to assemble, program and operate. Moreover, the inherent flexibility of the system allows the plunger to be readily adapted to a variety of projects. Finally, we demonstrate the efficacy of LED-based light sources for catalyzing photochemical reactions on grids by reducing the pH of tris-buffered solutions via photo-uncaging protons and, in doing so, driving large-scale conformational changes in recombinant ASICs.

We acknowledge that significant irradiation – even for short periods of time – will have detrimental effects on the sample that may indeed preclude successful structure determination. Due to the high number of uncaging events required to decrease the pH of a buffered solution to levels low enough to activate ASICs, we propose that photo-activation of ASICs represents a particularly demanding application of the flash-plunge device. Accordingly, protein quality suffered in the ASIC grids exposed to a 3000 mA flash. However, as demonstrated in the reconstructions of ASIC exposed to a 1000 mA flash, we did not observe significant impacts on particle quality or structure determination following moderate irradiation. Therefore, we submit that photochemically-demanding projects will be more prone to the detrimental effects of UV exposure, but that these effects are less likely to be observed at the levels of irradiation required for common flash-plunge applications.

While alternative approaches to time-resolved cryo-EM, including spray-plunge and flash-lamp photolysis techniques, have been shown to be effective, we propose that our apparatus mitigates existing issues related to ice variability and improves upon the flexibility and approachability of implementing a time-resolved system in most laboratory environments. As such, our flash-plunge system complements existing methods of sample preparation and provides the rapidly expanding cryo-EM community with a flexible new platform to approach time-resolved cryo-EM experiments.

Acknowledgements

We thank L. Vaskalis for help with figures, H. Owen for manuscript preparation and all Gouaux lab members for their support. Additionally, we thank Thomas Braun and Lucas Rima for helpful instruction regarding manual plunger design. This research was supported by the National

Institute of Diabetes and Digestive Kidney Diseases (5T32DK007680) and the National Institute of Neurological Disorders and Stroke (5F31NS096782 to N.Y., 5F32MH115595 to F.J.-Y, and 5R01NS038631 to E.G.). Cryo-EM data was collected at the Pacific Northwest Center for Cryo-EM. Additional support was provided by ARCS Foundation and Tartar Trust fellowships. E.G. is an Investigator with the Howard Hughes Medical Institute.

Tables

	cASIC1a 1000 mA flash	cASIC1a 3000 mA flash	
Data collection/processing			
Microscope	Krios (PNCC)	Krios (PNCC)	
Camera	K3	K3	
Magnification	105,000	105,000	
Voltage (kV)	300	300	
Exposure time (s)	2	2	
Frames (no.)	50	50	
Electron exposure (e–/Å^2)	40-50	40-50	
Defocus range (μm)	-0.8 – -2.2	-0.8 – -1.8	
Pixel size (Å)	0.83	0.83	
Initial micrographs (no.)	3,590	10,827	
Micrographs used (no.)	2,743	7,853	
Particles picked (no.)	430,583	3,647,147	
2D and 3D cleaned particles (no.)	92,450	189,366	
Final Refinement		**channel**	**ECD**
Symmetry imposed	C3	C1	
Final particles (no.)	16,673	45,135	
Map resolution (Å)	4.0	3.6	3.5
FSC threshold	0.143	0.143	

Table 5.1: Cryo-EM data collection and processing statistics

Figures and legends

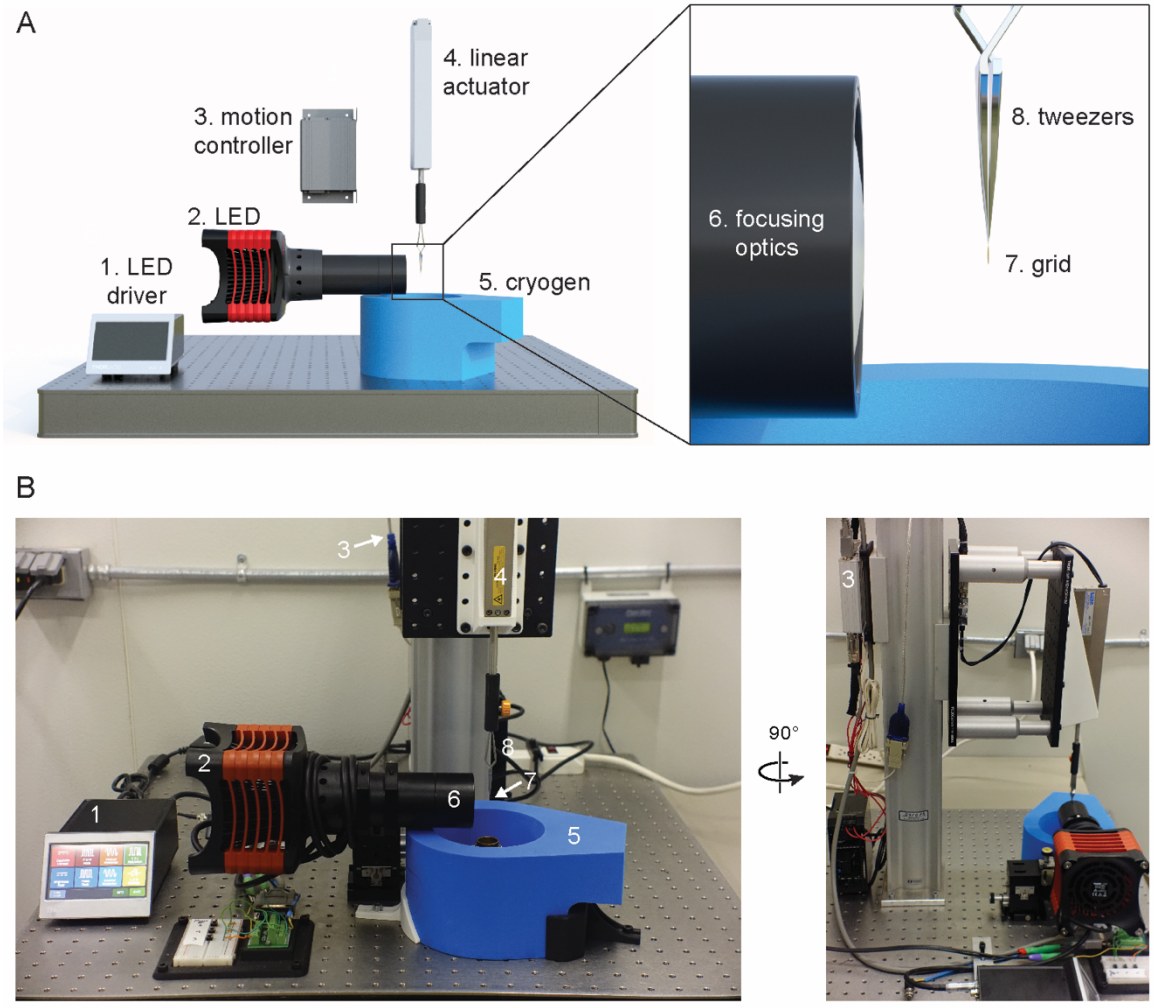

Figure 5.1. Instrument design and schematic. a, Cartoon representation of the flash-plunge device with inset showing close-up view of focusing optics and grid. **b,** Picture of the actual flash-plunge device with a side-view shown on the right. Numbers in white correlate to components outlined in (**a**).

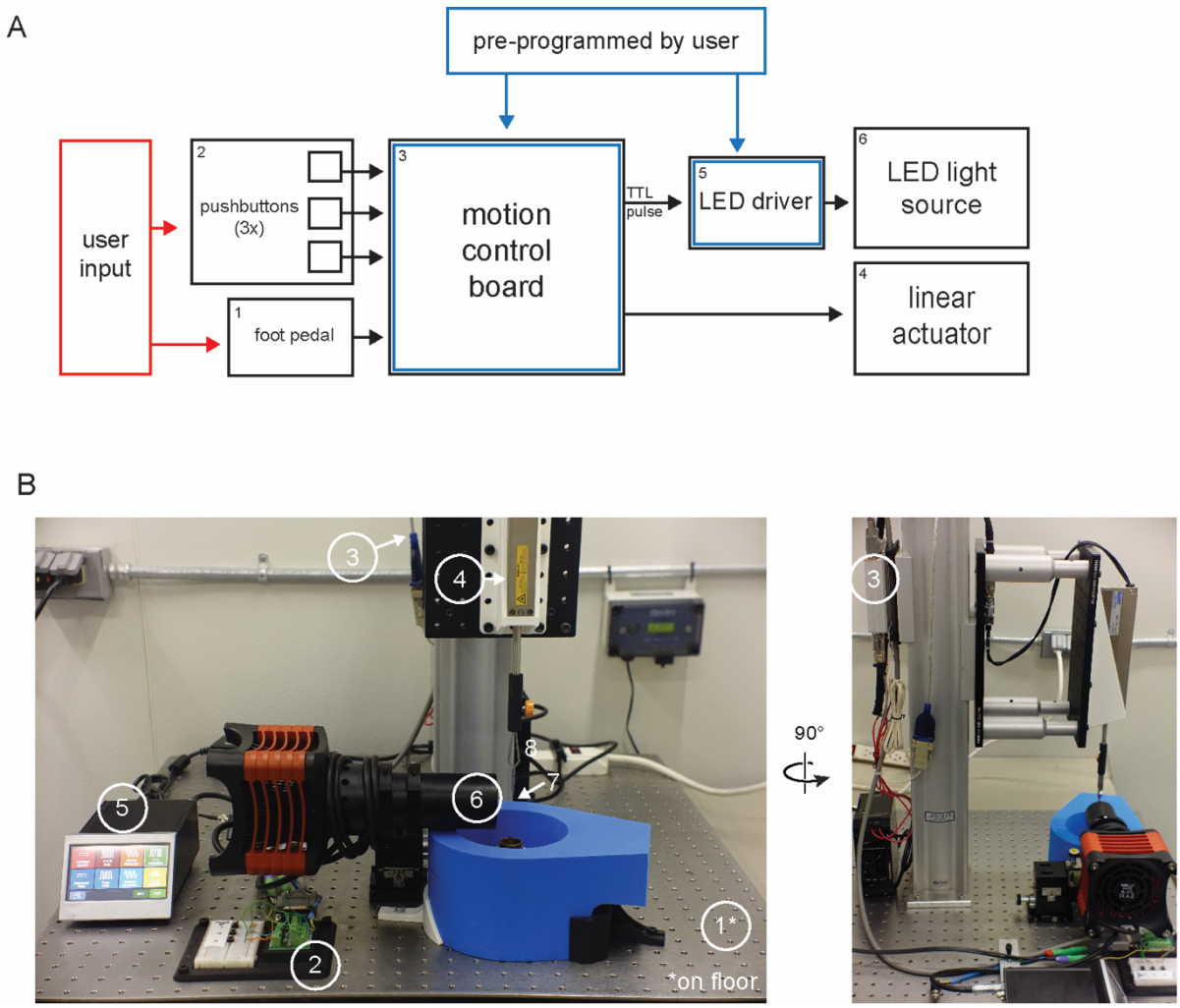

Figure 5.2. Instrument control diagram. a, Basic 2D schematic of instrument control and programming. Red denotes input required from the user to initiate the experiment, blue denotes information programmed by the user prior to the experiment. **b,** Picture of the actual flash-plunge device with a side-view shown on the right. Numbers in white correlate to components outlined in (**a**).

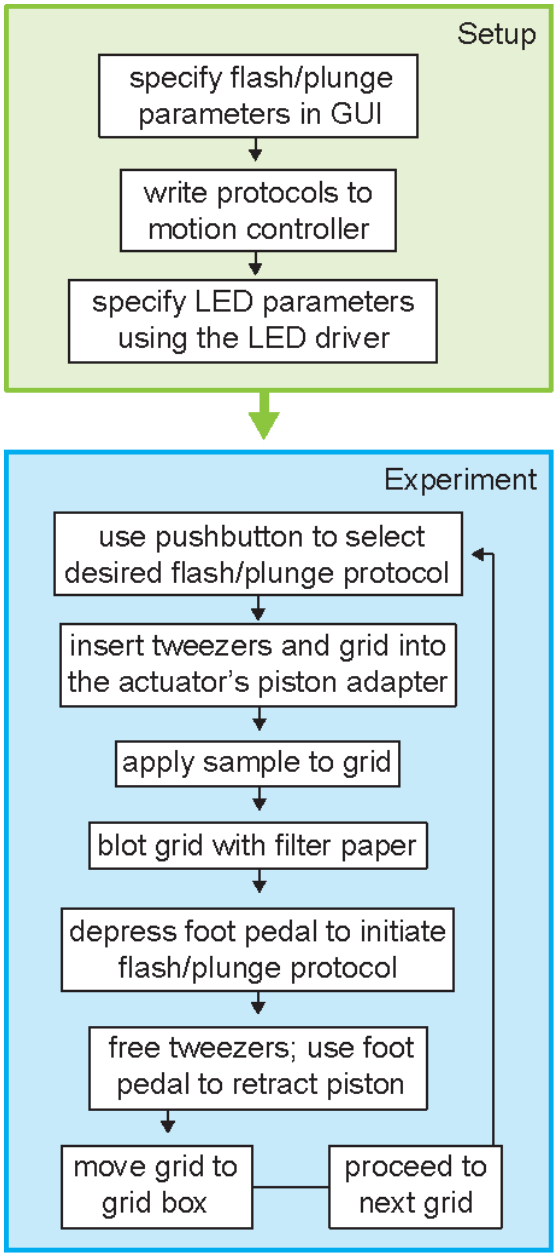

Figure 5.3. Sample workflow. Overview of the general workflow for the flash-plunge instrument.

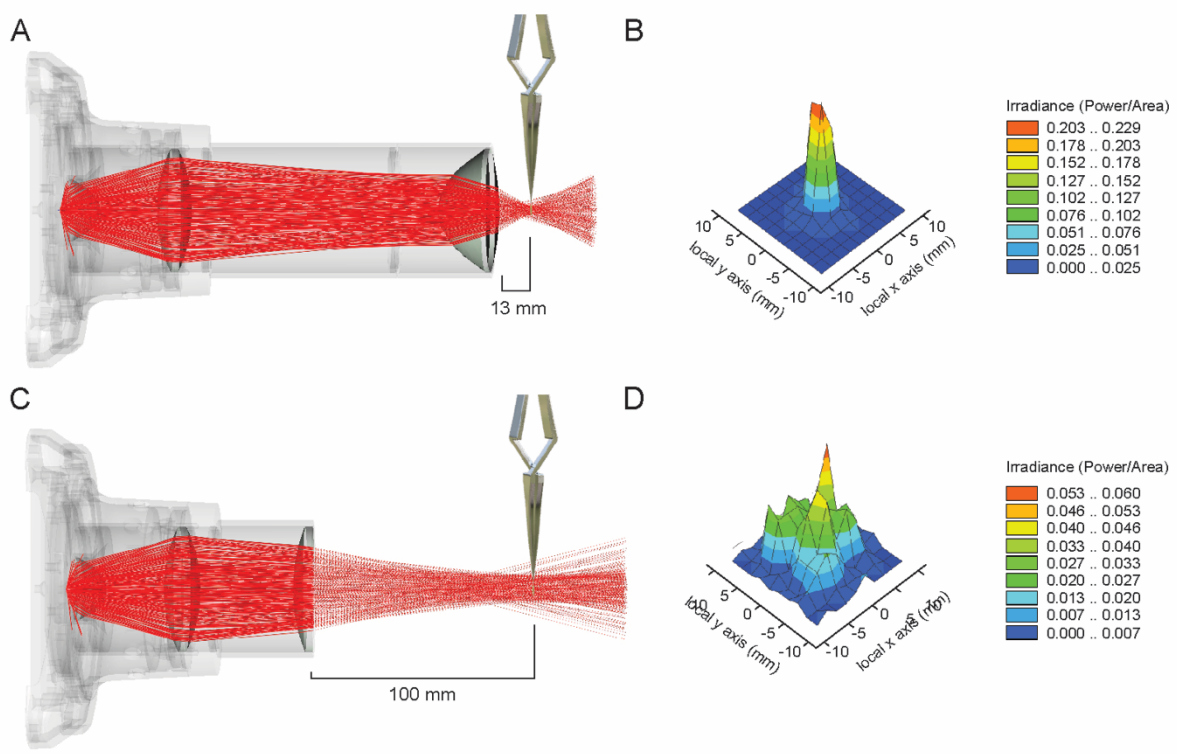

Figure 5.4. Light pathway. a-b, FRED ray-trace diagram (**a**) and irradiance distribution plot (**b**) for the flash-plunger equipped with an aspheric condenser lens. **c-d,** FRED ray-trace diagram (**c**) and irradiance distribution plot (**d**) for the alternative long working distance setup equipped with a plano convex lens.

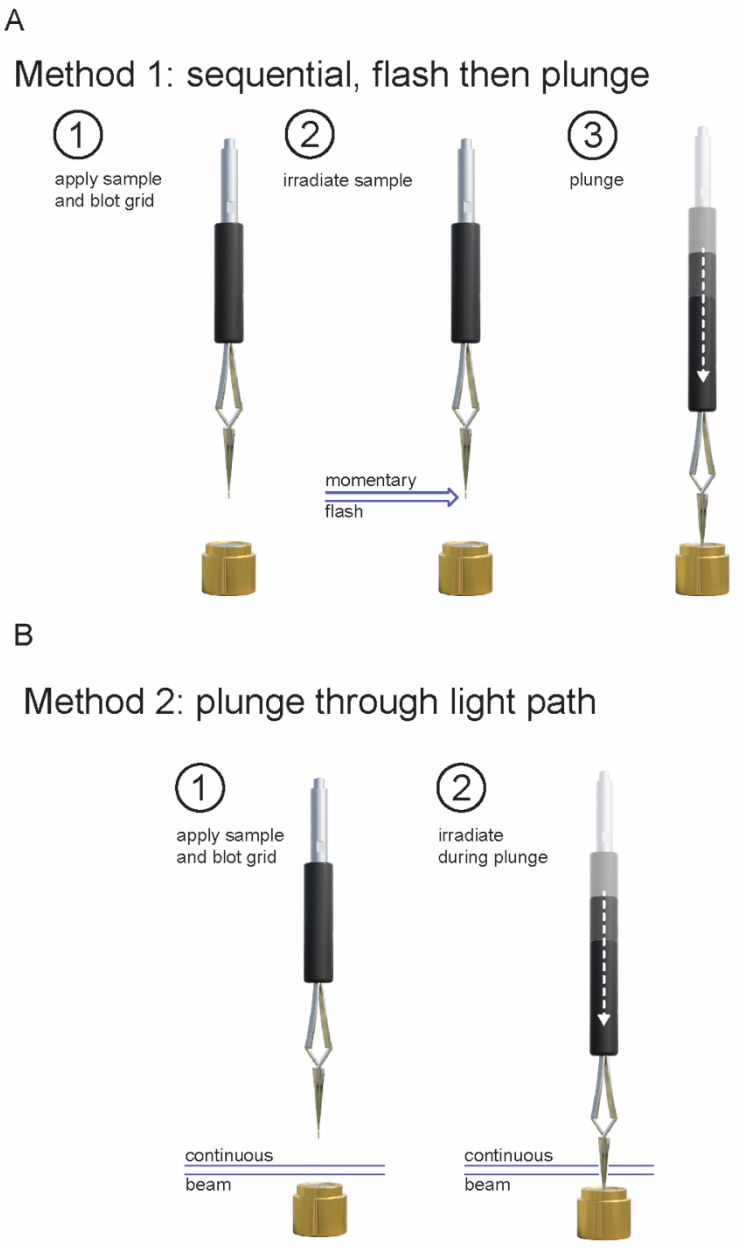

Figure 5.5. Flash-plunge protocols. a-b, Graphical representations of the sequential 'flash-then-plunge' protocol (**a**) and the faster alternate protocol (**b**) wherein a blotted grid is moved through a continuous beam path.

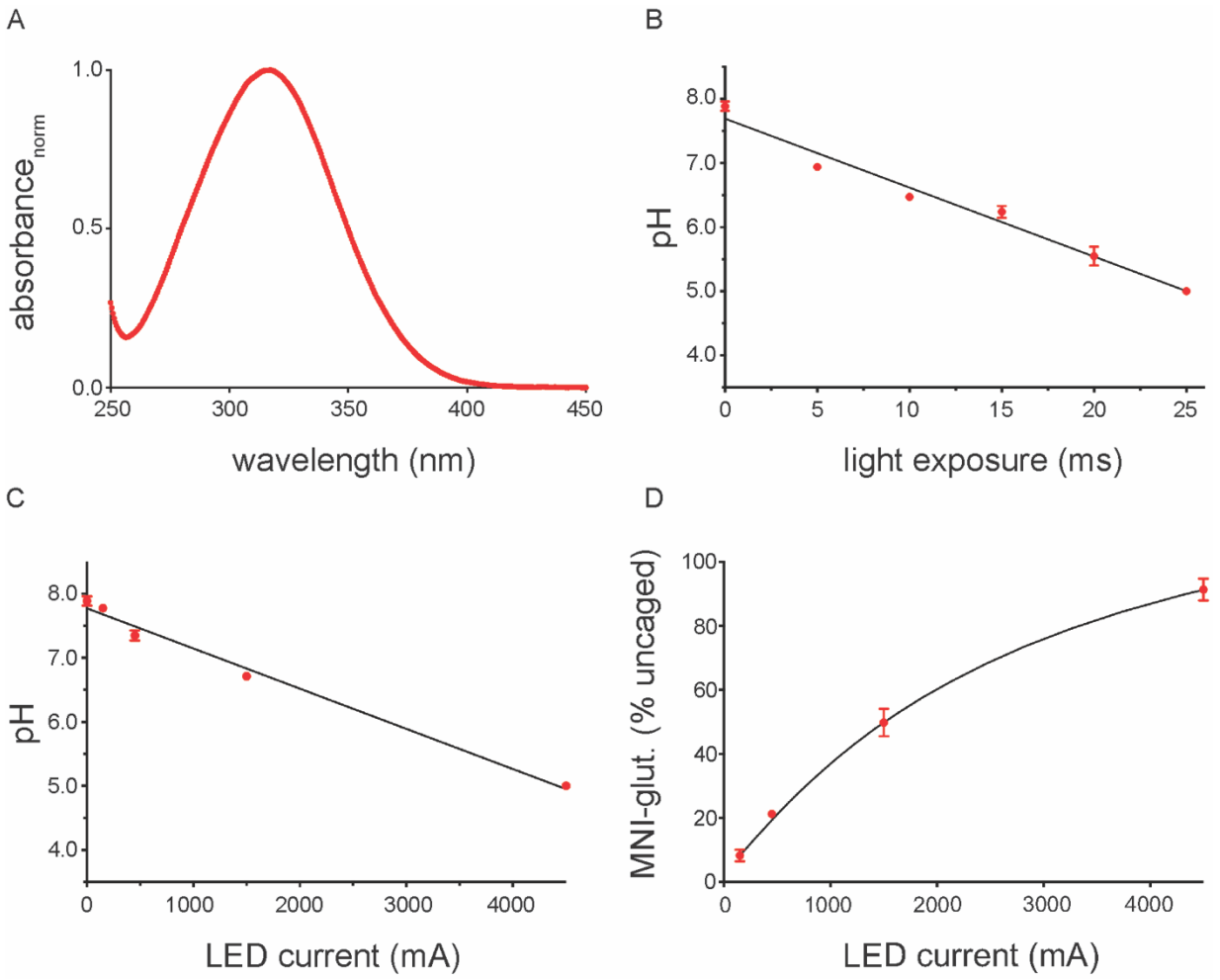

Figure 5.6. Uncaging protons and glutamate via light exposure. a, Absorbance spectrum for MNPS.Na between 250-450 nm. **b-c,** Plot of pH vs light exposure time at 4500 mA LED current (**b**) or pH vs LED current for a 25 ms exposure (**c**) for MNPS.Na. **d,** Plot of uncaged glutamate vs LED current for a 25 ms exposure. For **b-d**, n=3, data represent mean, error bars represent SEM and black lines represent interpolated linear (**b-c**) and sigmoidal (**d**) fits.

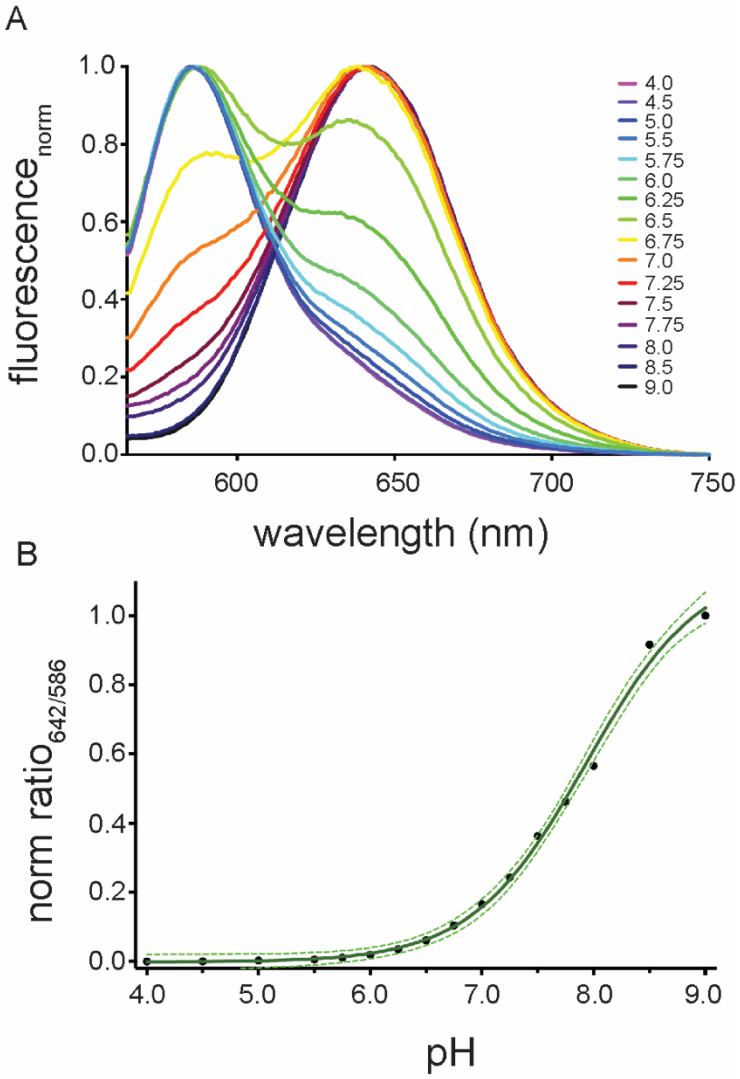

Figure 5.7. pH-dependence of SNARF-4F probe. a, Normalized fluorescence emission spectra (Ex. 543 nm) of pH-adjusted buffer containing 8 mM Tris, 4 mM MES, 150 mM NaCl and 10 µM SNARF-4F measured between 565 nm and 750 nm. n=3, data represent mean. b, Plot of pH vs ratio of fluorescence at 642nm (high pH peak) and 586 nm (low pH peak). n=3, data represent mean (black circles) and interpolated standard curve is shown as solid green line with 95% confidence internal shown in dashed green.

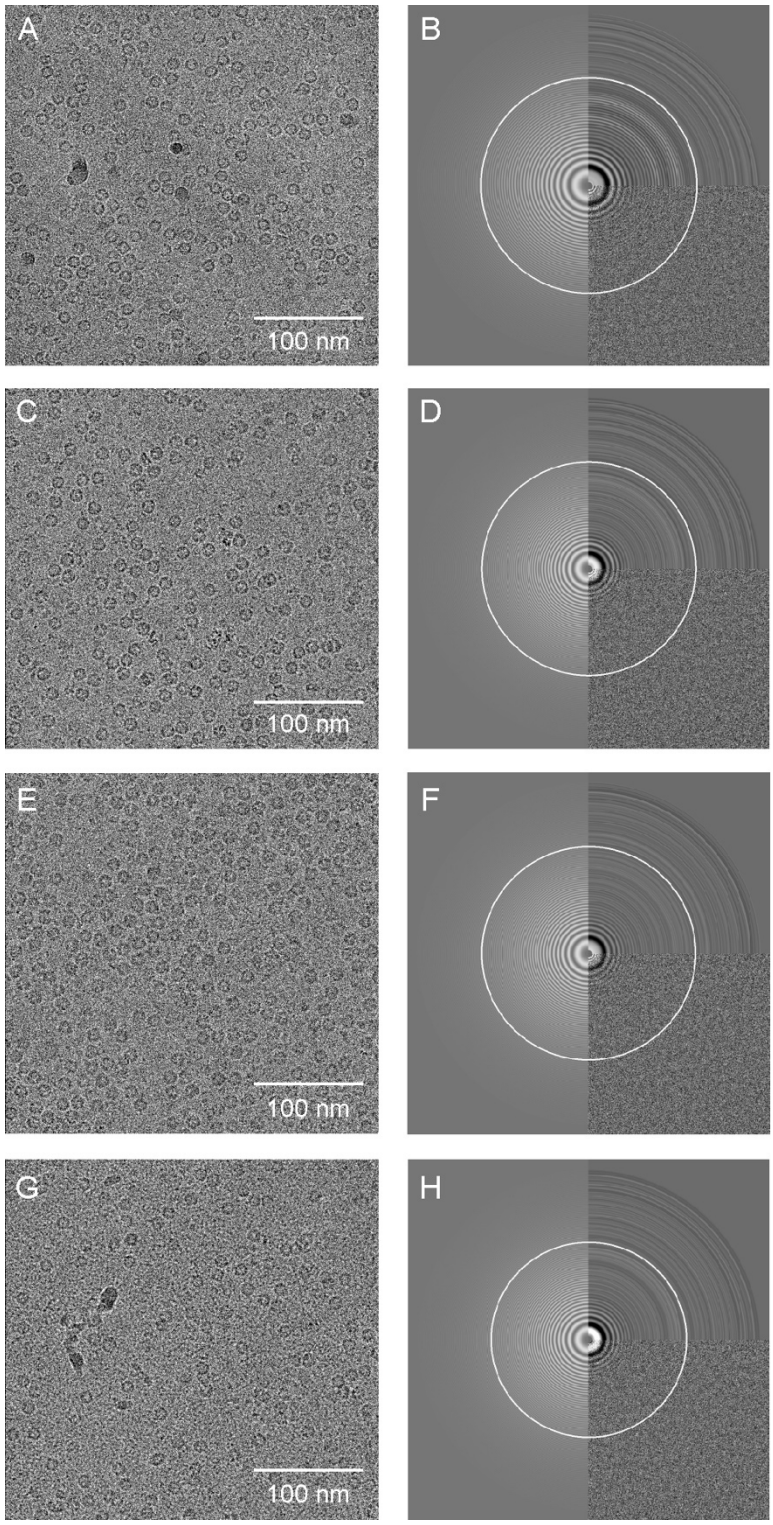

Figure 5.8. Flashed apoferritin grids. a-b, Representative micrograph (**a**) and Gctf power spectrum (**b**) for apoferritin grids not exposed to UV radiation. **c-d,** Representative micrograph (**c**) and Gctf power spectrum (**d**) for apoferritin grids exposed to a 25 ms 450 mA UV LED flash.

e-f, Representative micrograph (**e**) and Gctf power spectrum (**f**) for apoferritin grids exposed to a 25 ms 1350 mA UV LED flash. **g-h,** Representative micrograph (**g**) and Gctf power spectrum (**h**) for apoferritin grids exposed to a 25 ms 4500 mA UV LED flash.

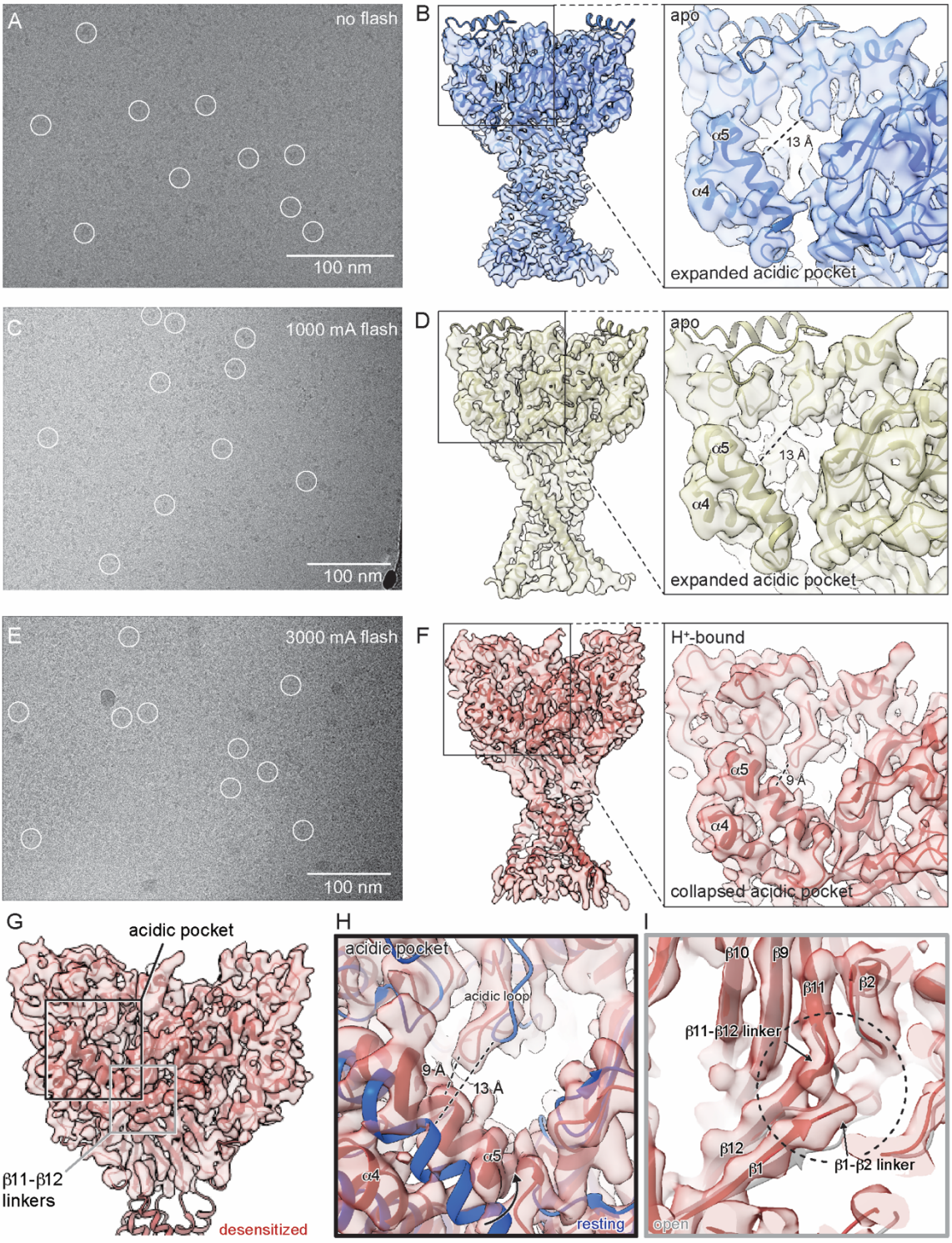

Figure 5.9. A photochemically-initiated conformational change in ASICs. a-b, Example micrograph with selected ten top-down views shown in white circles (**a**) and cryo-EM reconstruction (**b**) of cASIC1a not exposed to UV radiation and occupying a resting state (Yoder

and Gouaux, to be submitted). Coordinates for the x-ray structure of a resting channel (PDB 5WKU) were rigid body fit into the map. Inset shows close-up view of the acidic pocket. **c-d,** Example micrograph with selected ten top-down views shown in white circles (**c**) and cryo-EM reconstruction (**d**) of cASIC1a exposed to a 1000 mA UV flash for 25 ms and occupying a resting state. Coordinates for the x-ray structure of a resting channel (PDB 5WKU) were rigid body fit into the map. Inset shows close-up view of the acidic pocket. **e-f,** Example micrograph with selected ten top-down views shown in white circles (**e**) and cryo-EM reconstruction (**f**) of cASIC1a to a 3000 mA UV flash for 25 ms and occupying a desensitized state. Coordinates for the x-ray structure of a desensitized channel (PDB 4NYK) were rigid body fit into the map. Inset shows close-up view of the acidic pocket. **g-h,** Locally-refined map of the ECD from the 3000 mA flash dataset (**g**) demonstrating conformational changes at the acidic pocket (**h**) and β1-β2/β11-β12 linkers (**i**) associated with the desensitized channel conformation. Coordinates for the x-ray structure of a desensitized channel (PDB 4NYK, red) were rigid body fit into the ECD-map. For structural comparisons in **h-i**, coordinates for the resting (PDB 5wku, blue) and open (PDB 4NTW, grey) channels were superposed.

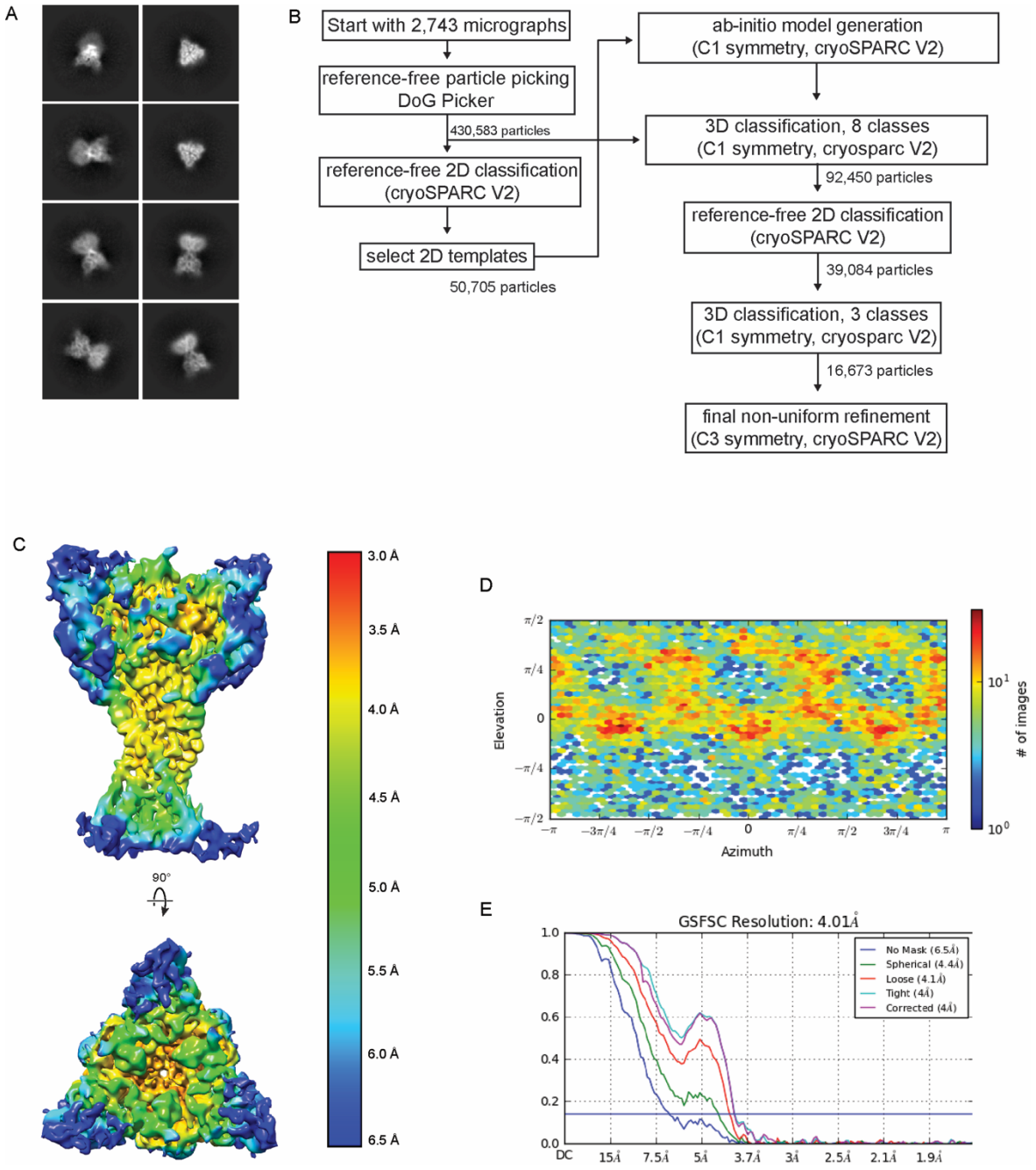

Figure 5.10. Cryo-EM data processing of 1000 mA flashed cASIC1a. a, Selected 2D classes. **b,** Schematic of cryo-EM data processing workflow. **c-e,** local resolution estimation (**c**) particle distribution (**d**) and resolution estimation (**e**) from final non-uniform refinement in cryoSPARC V2.

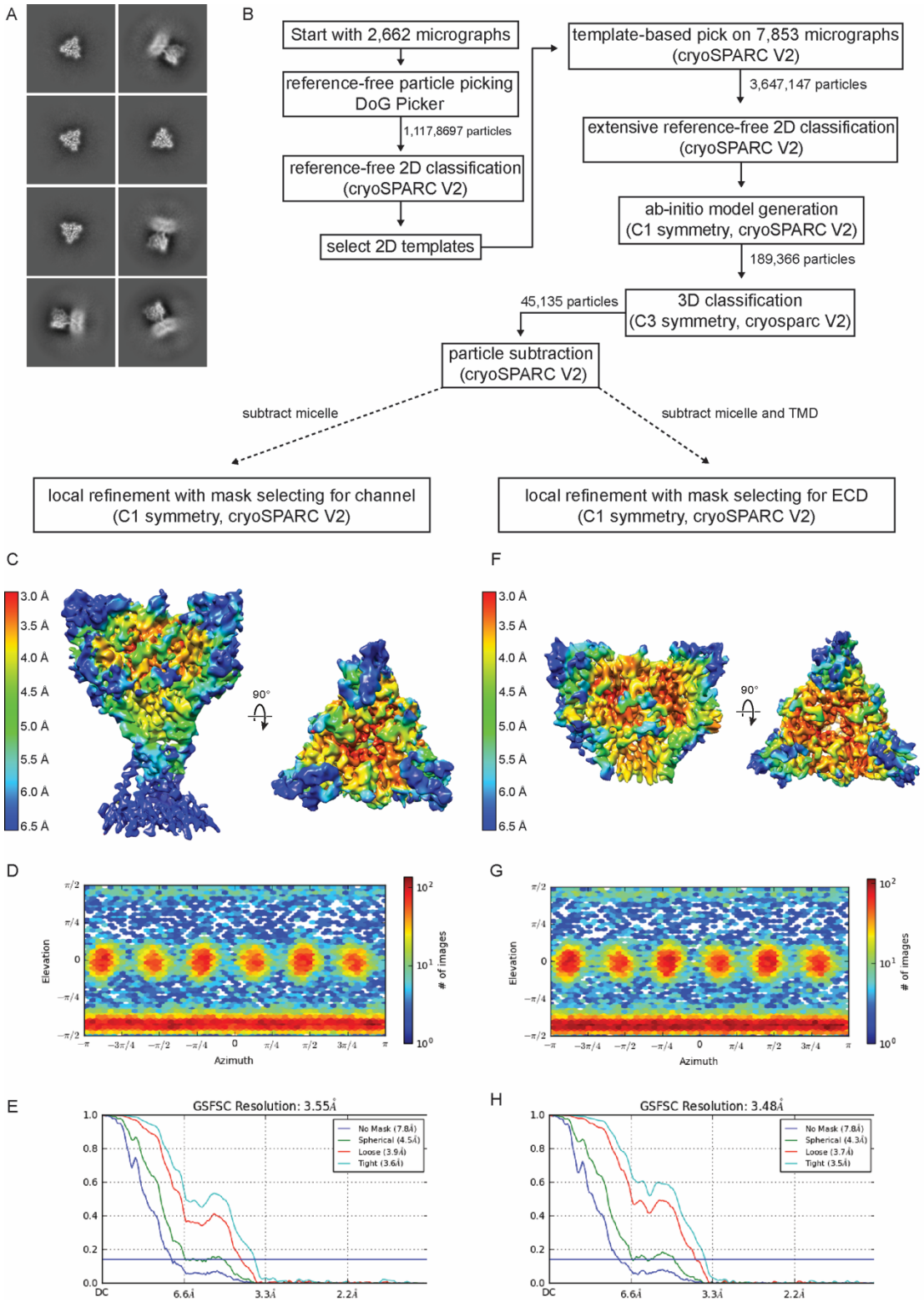

Figure 5.11. Cryo-EM data processing of 3000 mA flashed cASIC1a. a, Selected 2D classes. **b,** Schematic of cryo-EM data processing workflow. **c-e,** local resolution estimation (**c**) particle

distribution (**d**) and resolution estimation (**e**) from final local refinement using a map containing the whole channel. **f-h,** local resolution estimation (**c**) particle distribution (**d**) and resolution estimation (**e**) from final local refinement using a map containing the only the ECD.

Chapter 6

Concluding remarks

Summary

Members of the epithelial sodium channel/degenerin (ENaC/DEG) superfamily of ion channels participate in a diverse array of physiological processes, respond to a host of disparate stimuli and are subject to numerous mutations with ties to human disease. This broad expression pattern and high therapeutic relevance makes developing a structural framework for this family of ion channels an important step in determining molecular mechanisms for their contribution to biology and to developing targeted therapeutics.

As proton-gated[36] members of the ENaC/DEG superfamily[128], acid-sensing ion channels (ASICs) have been the subject of intense scrutiny due to mounting evidence for their participation in central and peripheral nervous systems processes, including nociception[40,66] and memory formation[77,78,86], and pathologies, such as ischemia[64], stroke and traumatic brain injury[162]. A simple gating scheme for ASICs includes three distinct functional states: a non-conducting resting state at high pH, a low pH open state and a low pH desensitized state[54]. Unlike most members of the ENaC/DEG family of ion channels, ASICs have proven tractable to structural exploration, yielding valuable atomic details pertaining to these pH-dependent channel conformations[20,55-57,101,156].

The first x-ray structure of ASIC1a illuminated a homotrimeric ion channel in a non-conducting conformation at low pH[20]. Each subunit resembles a clenched fist and consists of a large extracellular domain (ECD) split into thumb, finger, palm, β-ball, wrist, and knuckle domains separated from disordered intracellular termini by two slender membrane spanning helices. In addition to defining the architecture of the ECD, this landmark study exposed a highly electrostatically negative cavern formed between thumb, finger and palm domains – dubbed the acidic pocket – that was proposed to play a role in both proton-dependent gating and inhibition

by divalent cations. Amazingly, the first crystal structure represents the highest resolution structure of an ASIC to date and laid the groundwork for years of successful x-ray studies to follow.

Following the determination of the first x-ray structure of an ASIC, subsequent crystallographic efforts captured confirmations of the homotrimeric ASIC1a channel in low pH desensitized[57] and toxin-bound conformations – the latter encompassing the structures of open gating-modified and open channels bound to PcTx1[56,101] and MitTx[55], respectively. In contrast to prior ASIC structures, the structure of an open channel bound to the heterodimeric MitTx toxin uncovered a unique domain-swapped transmembrane helix 2 (TM2) split into TM2a and TM2b by an extended Gly-Ala-Ser loop motif. The 'GAS belt', named for its component residues and long thought to control selectivity in ENaCs[123,124,144], formed the primary constriction point along the ion permeation pathway of the open channel, providing a structural rationale for the GAS belt in determining ion selectivity. These structures elucidated the architecture of desensitized and open channels including the GAS belt TM2 domain swap, exposed mechanisms for modulation of channel gating by biological toxins and described molecular mechanisms for Na^+ selectivity in ASICs and ENaCs.

At the onset of this work, the expansive crystallographic efforts detailed above had contributed to an extensive body of research surrounding the molecular architecture, gating, modulation and ion permeation properties of ASICs. However, lacking the atomic structure of the resting channel at high pH, key details pertaining to activation and desensitization remained elusive. Furthermore, still undetermined were the location of binding sites for divalent cations and a molecular mechanism for their inhibition of proton-dependent gating in ASICs. As such, the work outlined in this dissertation pertains in large part to the pursuit of the resting channel

structure, the determination of binding sites for divalent cations, and the development of a comprehensive molecular mechanism for proton-dependent gating of ASIC1a.

The two primary challenges to working with chicken ASIC1a were the relatively low stability of the recombinant protein and its reticence to crystallization under high pH conditions. However, by including both cholesterol and divalent cations during the late stages of protein purification and crystallization, I successfully applied x-ray crystallographic methods to determine the structure of a resting channel at high pH. Furthermore, by leveraging the anomalous scattering characteristics of Ba^{2+}, I was able to map ion binding sites for divalent cations on both high pH resting and low pH desensitized channels. These x-ray structures of ASIC1a in a resting state at high pH provided molecular mechanisms for activation and desensitization and illuminated the complex interplay between proton-dependent gating and divalent cations, which likely compete for multiple binding sites at the ECD of the channel.

The architecture of a resting ASIC1a channel at high pH is characterized by an expanded acidic pocket and a pore closed to ion permeation, demonstrating that a collapse of the acidic pocket upon proton binding is indispensable to proton-dependent activation. Despite the disparate conformations of the upper ECD between high pH and low pH states, the lower domains of the resting channel – those below β1-β2 and β11-β12 linkers and including the TMDs and ion permeation gate – closely mirror those of the desensitized channel. Indeed, I demonstrate how the β11-β12 and β1-β2 linkers serve as a 'molecular clutch', anchoring proton-dependent collapse of the acidic pocket to the lower channel upon activation and permitting desensitization by effectively decoupling the collapsed acidic pocket from the lower channel via a dramatic 'side chain swap'.

Mapping sites for Ba^{2+} ions on resting and desensitized channels via anomalous scattering revealed a complex and pH-dependent network of ion binding sites. On the resting channel at high pH we detected three total Ba^{2+} ions per subunit – two within the expanded acidic pocket and one at the central vestibule. In contrast, Ba^{2+} occupancy on the desensitized channel at low pH was limited to a single site at the entrance to the proton-bound acidic pocket. That both the acidic pocket and central vestibule harbor state-dependent binding sites for divalent cations and contribute to proton-dependent gating is indicative of a spatial overlap between gating and modulation. As such, these results show that an increased requirement for protons to activate ASICs in the presence of high concentrations of divalent cations is due – at least in part – to competition for common binding sites. Notably, however, detailed molecular mechanisms and the contribution of individual residues to this modulation remain undetermined.

Within the past decade the development and optimization of techniques such as single-particle cryo-EM and methods for detergent-free purification of membrane proteins have dramatically improved our capacity as biochemists to study these proteins in near-native environments. As such, following the determination of the resting channel x-ray structure, subsequent research focused on elucidating the molecular architecture of full-length ASICs in both detergent micelles and in membrane-like lipid environments by single-particle cryo-EM, work previously inaccessible by conventional crystallographic means. Towards this end, I first pursued the structure of a full-length cASIC1a channel in a detergent micelle and in a resting state at high pH. Shortly thereafter, I developed detergent-free methods to extract and purify full-length cASIC1a channels from membranes using styrene-maleic acid (SMA) copolymers and, in combination with single-particle cryo-electron microscopy (cryo-EM), determined structures of

full-length channels in both high pH resting and low pH desensitized conformations in a membrane-like lipid environment.

Structures of both desensitized and resting cASIC1a channels in a membrane-like environment exposed a re-entrant loop at the amino terminus that harbors the highly conserved His-Gly motif known to be critical for gating in ENaCs[102], providing the first structure-based evidence for contributions of pre-TM1 residues to gating and ion permeation characteristics of ENaC/DEG ion channels. In contrast, cryo-EM structures of resting cASIC1a channels in a detergent micelle mirrored x-ray structures of the truncated channel in a resting state at high pH[156], including disordered terminal residues, indicating that the architecture of the lower ion permeation pathway is indeed sensitive to the local environment.

Homotrimeric cASIC1a opens within milliseconds and enters a long-lived desensitized state within tens to hundreds of milliseconds[57]. As such, in contrast to long-lived resting and desensitized states, capturing the structure of an open channel in a membrane-like environment without the use of pharmacological or mutagenic means was not possible by conventional cryo-EM methods. To meet these challenges, I developed a system to couple photoactivation of ligands and sample vitrification with temporal resolution approaching tens of milliseconds. The 'flash-plunge' system enabled me to drive conformational changes in ASICs by photo-uncaging protons, thus decreasing the pH of the solution and, in theory, activating channels tens of milliseconds prior to freezing the grids.

Despite freezing samples within ~ 65 milliseconds of photo-activation, I was only able to obtain a reconstruction of cASIC1a in a proton-bound desensitized state, indicating that isolated channels passed through an open state and entered the non-conducting desensitized state prior to sample vitrification. Therefore, while the flash-plunge system was effective at driving an on-grid

conformational change, the temporal resolution of the system was insufficient to capture the architecture of an open, proton-activated channel. Furthermore, the substantial light application required to uncage sufficient protons to activate ASICs had a detrimental impact on both ice quality and particle distribution, complicating data processing and structure determination. Consequently, while the flash-plunge technique and associated instrumentation is promising, further optimization is required for the system to be fully effective, and thus the structure of a full-length ASIC in a proton-activated open state remains unknown.

The research outlined in this dissertation represents substantial progress towards understanding the molecular functions of a proton-gated ion channel of broad physiological and therapeutic significance. Moreover, given the striking structural similarities uncovered by the recent determination of the first structure of a human ENaC channel[164], the mechanisms uncovered through the study of ASICs may pertain to the entire ENaC/DEG family of ion channels, whose influence extends well beyond the nervous system.

Future directions

Explore channel-lipid interactions

Though the lipid composition of SMA-cASIC1a particles is as of yet unknown, the fact that we did not observe a structured pre-TM1 re-entrant loop in cASIC1a channels solubilized in micelles comprised of certain detergents – namely *n*-dodecyl β-D-maltoside and n-decyl-β-D-thiomaltopyranoside – reveals a sensitivity of the lower pore architecture to its external environment. Subsequent research will likely shed light upon how local lipids interact with the TM domains to support or alter the structure and function of ASICs. Toward this end, it will be important to apply mass-spectrometry methods to SMA-extracted ASICs in an effort to

determine lipids and other cofactors retained in SMA-ASIC lipid particles through purification. Furthermore, reconstituting recombinant ASICs into nanodiscs of defined lipid composition and assessing the conformational and/or functional consequences via single-particle cryo-EM and planar lipid bilayer recordings, respectively, will inform our understanding of the interaction between ASICs and the plasma membrane.

Pursue the atomic structures of other ASICs

The entirety of ASIC structural biology efforts to date have focused on the homotrimeric splice variant ASIC1a. However, numerous other ASIC isoforms exist within central and peripheral nervous systems that assemble as homo- or heterotrimers, representing a diverse group of ion channels of broad significance. As such, efforts to determine the structures of homomeric ASIC3 channels – which are particularly relevant to peripheral processes – and heteromeric channels containing ASIC1a and ASIC2a isoforms – which are primary localized to the central nervous system – represents an outstanding goal of the field. In order to determine the structure of a heteromeric channel, successful subunit assignment, as well as alignment of particles for high-resolution cryo-EM reconstructions, will likely require the use of antibodies specific to individual subunits, an approach that proved essential to determining the first structure of the heteromeric α/β/γ ENaC by single-particle cryo-EM[164].

Pursuit of native receptors

Excitingly, the relatively low protein requirements for cryo-EM as well as improvements in methods for generating targeted antibodies have opened the doors to extracting membrane proteins directly from native sources for structure determination. This, in combination with detergent-free methods of protein extraction and purification, is likely to represent a new standard for physiological relevance in structural biology. Accordingly, future structural

experiments for ASICs should include efforts to obtain channels from native membranes including – but not limited to – mouse and rat whole-brain preparations using antibodies with a demonstrated specificity toward a 3D epitope pertaining to individual ASIC subunits.

Optimize flash-plunge device for time-resolved structure determination

The results of my initial experiments using the flash-plunge device for time-resolved cryo-EM showed promise, confirming the capability of the method to drive an on-grid conformational change in ASICs by photo-uncaging protons. Despite my limited success, however, the goal of time-resolved structure determination has not yet been fully realized as I was unable to capture an ASIC in a proton-activated open state by this approach. As such, future efforts should address outstanding issues pertaining to the flash-plunge method and instrumentation including mitigating light-induced temperature spikes and associated sample evaporation, minimizing conformational heterogeneity of the sample and improving blot conditions. Furthermore, effort should be made to improve the temporal resolution of the device to capture rapid conformational changes and to therefore encompass a wider array of potential projects.

References

1 Ringer, S. A further Contribution regarding the influence of the different Constituents of the Blood on the Contraction of the Heart. *J Physiol* **4**, 29-42 23 (1883).

2 Ringer, S. Concerning the Influence exerted by each of the Constituents of the Blood on the Contraction of the Ventricle. *J Physiol* **3**, 380-393 (1882).

3 Bernstein, J. Untersuchungen zur Thermodynamik der bioelektrischen Ströme. *Pflüger Archiv für die Gesammte Physiologie des Menschen und der Thiere* **92**, 521-562, doi:10.1007/bf01790181 (1902).

4 Hodgkin, A. L. & Huxley, A. F. Propagation of electrical signals along giant nerve fibers. *Proc R Soc Lond B Biol Sci* **140**, 177-183 (1952).

5 Hodgkin, A. L. & Huxley, A. F. A quantitative description of membrane current and its application to conduction and excitation in nerve. *J Physiol* **117**, 500-544 (1952).

6 Hodgkin, A. L. & Huxley, A. F. The dual effect of membrane potential on sodium conductance in the giant axon of Loligo. *J Physiol* **116**, 497-506 (1952).

7 Hodgkin, A. L. & Huxley, A. F. The components of membrane conductance in the giant axon of Loligo. *J Physiol* **116**, 473-496 (1952).

8 Hodgkin, A. L. & Huxley, A. F. Currents carried by sodium and potassium ions through the membrane of the giant axon of Loligo. *J Physiol* **116**, 449-472 (1952).

9 Hodgkin, A. L., Huxley, A. F. & Katz, B. Measurement of current-voltage relations in the membrane of the giant axon of Loligo. *J Physiol* **116**, 424-448 (1952).

10 Neher, E. & Sakmann, B. Single-channel currents recorded from membrane of denervated frog muscle fibres. *Nature* **260**, 799-802 (1976).

11 Neher, E., Sakmann, B. & Steinbach, J. H. The extracellular patch clamp: a method for resolving currents through individual open channels in biological membranes. *Pflugers Arch* **375**, 219-228 (1978).

12 Hille, B. *Ion channels of excitable membranes*. 3rd edn, (Sinauer, 2001).

13 Jordt, S.-E. *et al.* Mustard oils and cannabinoids excite sensory nerve fibres through the TRP channel ANKTM1. *Nature* **427**, 260-265, doi:10.1038/nature02282 (2004).

14 McKemy, D. D., Neuhausser, W. M. & Julius, D. Identification of a cold receptor reveals a general role for TRP channels in thermosensation. *Nature* **416**, 52-58, doi:10.1038/nature719 (2002).

15 Caterina, M. J. *et al.* The capsaicin receptor: a heat-activated ion channel in the pain pathway. *Nature* **389**, 816-824, doi:10.1038/39807 (1997).

16 Coste, B. *et al.* Piezo1 and Piezo2 Are Essential Components of Distinct Mechanically Activated Cation Channels. *Science* **330**, 55-60, doi:10.1126/science.1193270 (2010).

17 Doyle, D. A. *et al.* The structure of the potassium channel: molecular basis of K+ conduction and selectivity. *Science* **280**, 69-77 (1998).

18 Jiang, Y. *et al.* X-ray structure of a voltage-dependent K+ channel. *Nature* **423**, 33-41, doi:10.1038/nature01580 (2003).

19 Kawate, T., Michel, J. C., Birdsong, W. T. & Gouaux, E. Crystal structure of the ATP-gated P2X(4) ion channel in the closed state. *Nature* **460**, 592-598, doi:10.1038/nature08198 (2009).

20 Jasti, J., Furukawa, H., Gonzales, E. B. & Gouaux, E. Structure of acid-sensing ion channel 1 at 1.9 Å resolution and low pH. *Nature* **449**, 316-323, doi:10.1038/nature06163 (2007).

21 Jiang, Y. *et al.* Crystal structure and mechanism of a calcium-gated potassium channel. *Nature* **417**, 515-522, doi:10.1038/417515a (2002).

22 Sobolevsky, A. I., Rosconi, M. P. & Gouaux, E. X-ray structure, symmetry and mechanism of an AMPA-subtype glutamate receptor. *Nature* **462**, 745-756, doi:10.1038/nature08624 (2009).

23 Lee, C. H. *et al.* NMDA receptor structures reveal subunit arrangement and pore architecture. *Nature* **511**, 191-197, doi:10.1038/nature13548 (2014).

24 Karakas, E. & Furukawa, H. Crystal structure of a heterotetrameric NMDA receptor ion channel. *Science* **344**, 992-997, doi:10.1126/science.1251915 (2014).

25 Goehring, A. *et al.* Screening and large-scale expression of membrane proteins in mammalian cells for structural studies. *Nat Protoc* **9**, 2574-2585, doi:10.1038/nprot.2014.173 (2014).

26 Magnani, F. *et al.* A mutagenesis and screening strategy to generate optimally thermostabilized membrane proteins for structural studies. *Nature Protocols* **11**, 1554-1571, doi:10.1038/nprot.2016.088 (2016).

27 Li, X. *et al.* Electron counting and beam-induced motion correction enable near-atomic-resolution single-particle cryo-EM. *Nature Methods* **10**, 584-590, doi:10.1038/nmeth.2472 (2013).

28 Liao, M., Cao, E., Julius, D. & Cheng, Y. Structure of the TRPV1 ion channel determined by electron cryo-microscopy. *Nature* **504**, 107-112, doi:10.1038/nature12822 (2013).

29 Unwin, N. Refined structure of the nicotinic acetylcholine receptor at 4A resolution. *J Mol Biol* **346**, 967-989, doi:10.1016/j.jmb.2004.12.031 (2005).

30 Berriman, J. & Unwin, N. Analysis of transient structures by cryo-microscopy combined with rapid mixing of spray droplets. *Ultramicroscopy* **56**, 241-252 (1994).

31 Kuhlbrandt, W. Biochemistry. The resolution revolution. *Science* **343**, 1443-1444, doi:10.1126/science.1251652 (2014).

32 Cheng, Y. Membrane protein structural biology in the era of single particle cryo-EM. *Current Opinion in Structural Biology* **52**, 58-63, doi:10.1016/j.sbi.2018.08.008 (2018).

33 Garcia-Anoveros, J., Derfler, B., Neville-Golden, J., Hyman, B. T. & Corey, D. P. BNaC1 and BNaC2 constitute a new family of human neuronal sodium channels related to degenerins and epithelial sodium channels. *Proc Natl Acad Sci U S A* **94**, 1459-1464 (1997).

34 Waldmann, R., Champigny, G., Bassilana, F., Heurteaux, C. & Lazdunski, M. A proton-gated cation channel involved in acid-sensing. *Nature* **386**, 173-177, doi:10.1038/386173a0 (1997).

35 Kellenberger, S. & Schild, L. Epithelial sodium channel/degenerin family of ion channels: a variety of functions for a shared structure. *Physiol Rev* **82**, 735-767, doi:10.1152/physrev.00007.2002 (2002).

36 Krishtal, O. A. & Pidoplichko, V. I. A receptor for protons in the nerve cell membrane. *Neuroscience* **5**, 2325-2327 (1980).

37 Alvarez de la Rosa, D., Zhang, P., Shao, D., White, F. & Canessa, C. M. Functional implications of the localization and activity of acid-sensitive channels in rat peripheral nervous system. *Proc Natl Acad Sci U S A* **99**, 2326-2331, doi:10.1073/pnas.042688199 (2002).

38 Krishtal, O. A. & Pidoplichko, V. I. Receptor for protons in the membrane of sensory neurons. *Brain Res* **214**, 150-154 (1981).

39 Krishtal, O. A. & Pidoplichko, V. I. A receptor for protons in the membrane of sensory neurons may participate in nociception. *Neuroscience* **6**, 2599-2601 (1981).

40 Krishtal, O. A. & Pidoplichko, V. I. A "receptor" for protons in small neurons of trigeminal ganglia: possible role in nociception. *Neurosci Lett* **24**, 243-246 (1981).

41 Price, M. P., Snyder, P. M. & Welsh, M. J. Cloning and expression of a novel human brain Na+ channel. *J Biol Chem* **271**, 7879-7882 (1996).

42 Delaunay, A. *et al.* Human ASIC3 channel dynamically adapts its activity to sense the extracellular pH in both acidic and alkaline directions. *Proc Natl Acad Sci U S A* **109**, 13124-13129, doi:10.1073/pnas.1120350109 (2012).

43 Hesselager, M., Timmermann, D. B. & Ahring, P. K. pH Dependency and desensitization kinetics of heterologously expressed combinations of acid-sensing ion channel subunits. *J Biol Chem* **279**, 11006-11015, doi:10.1074/jbc.M313507200 (2004).

44 Gründer, S., Geissler, H.-S., Bässler, E.-L. & Ruppersberg, J. P. A new member of acid-sensing ion channels from pituitary gland. *NeuroReport* **11**, 1607-1611 (2000).

45 Yang, L. & Palmer, L. G. Ion conduction and selectivity in acid-sensing ion channel 1. *J Gen Physiol* **144**, 245-255, doi:10.1085/jgp.201411220 (2014).

46 Gründer, S. & Pusch, M. Biophysical properties of acid-sensing ion channels (ASICs). *Neuropharmacology* **94**, 9-18, doi:10.1016/j.neuropharm.2014.12.016 (2015).

47 Sutherland, S. P., Benson, C. J., Adelman, J. P. & McCleskey, E. W. Acid-sensing ion channel 3 matches the acid-gated current in cardiac ischemia-sensing neurons. *Proc Natl Acad Sci U S A* **98**, 711-716, doi:10.1073/pnas.011404498 (2001).

48 Bassilana, F. *et al.* The Acid-sensitive Ionic Channel Subunit ASIC and the Mammalian Degenerin MDEG Form a Heteromultimeric H+-gated Na+Channel with Novel Properties. *Journal of Biological Chemistry* **272**, 28819-28822, doi:10.1074/jbc.272.46.28819 (1997).

49 Immke, D. C. & McCleskey, E. W. ASIC3: a lactic acid sensor for cardiac pain. *ScientificWorldJournal* **1**, 510-512, doi:10.1100/tsw.2001.254 (2001).

50 Immke, D. C. & McCleskey, E. W. Lactate enhances the acid-sensing Na+ channel on ischemia-sensing neurons. *Nat Neurosci* **4**, 869-870, doi:10.1038/nn0901-869 (2001).

51 Babini, E., Paukert, M., Geisler, H. S. & Gründer, S. Alternative splicing and interaction with di- and polyvalent cations control the dynamic range of acid-sensing ion channel 1 (ASIC1). *J Biol Chem* **277**, 41597-41603, doi:10.1074/jbc.M205877200 (2002).

52 Paukert, M., Babini, E., Pusch, M. & Gründer, S. Identification of the Ca2+ blocking site of acid-sensing ion channel (ASIC) 1: implications for channel gating. *J Gen Physiol* **124**, 383-394, doi:10.1085/jgp.200308973 (2004).

53 Immke, D. C. & McCleskey, E. W. Protons open acid-sensing ion channels by catalyzing relief of Ca2+ blockade. *Neuron* **37**, 75-84 (2003).

54 Zhang, P., Sigworth, F. J. & Canessa, C. M. Gating of acid-sensitive ion channel-1: release of Ca2+ block vs. allosteric mechanism. *J Gen Physiol* **127**, 109-117, doi:10.1085/jgp.200509396 (2006).

55 Baconguis, I., Bohlen, C. J., Goehring, A., Julius, D. & Gouaux, E. X-ray structure of acid-sensing ion channel 1-snake toxin complex reveals open state of a Na(+)-selective channel. *Cell* **156**, 717-729, doi:10.1016/j.cell.2014.01.011 (2014).

56 Baconguis, I. & Gouaux, E. Structural plasticity and dynamic selectivity of acid-sensing ion channel-spider toxin complexes. *Nature* **489**, 400-405, doi:10.1038/nature11375 (2012).

57 Gonzales, E. B., Kawate, T. & Gouaux, E. Pore architecture and ion sites in acid-sensing ion channels and P2X receptors. *Nature* **460**, 599-604, doi:10.1038/nature08218 (2009).

58 Wang, W., Duan, B., Xu, H., Xu, L. & Xu, T. L. Calcium-permeable acid-sensing ion channel is a molecular target of the neurotoxic metal ion lead. *J Biol Chem* **281**, 2497-2505, doi:10.1074/jbc.M507123200 (2006).

59 Chu, X. P. *et al.* Subunit-dependent high-affinity zinc inhibition of acid-sensing ion channels. *J Neurosci* **24**, 8678-8689, doi:10.1523/JNEUROSCI.2844-04.2004 (2004).

60 Baron, A., Schaefer, L., Lingueglia, E., Champigny, G. & Lazdunski, M. Zn2+ and H+ are coactivators of acid-sensing ion channels. *J Biol Chem* **276**, 35361-35367, doi:10.1074/jbc.M105208200 (2001).

61 Escoubas, P. *et al.* Isolation of a Tarantula Toxin Specific for a Class of Proton-gated Na+Channels. *Journal of Biological Chemistry* **275**, 25116-25121, doi:10.1074/jbc.m003643200 (2000).

62 Escoubas, P., Bernard, C., Lambeau, G., Lazdunski, M. & Darbon, H. Recombinant production and solution structure of PcTx1, the specific peptide inhibitor of ASIC1a proton-gated cation channels. *Protein Science* **12**, 1332-1343, doi:10.1110/ps.0307003 (2003).

63 Chen, X., Kalbacher, H. & Gründer, S. The tarantula toxin psalmotoxin 1 inhibits acid-sensing ion channel (ASIC) 1a by increasing its apparent H+ affinity. *J Gen Physiol* **126**, 71-79, doi:10.1085/jgp.200509303 (2005).

64 Xiong, Z. G. *et al.* Neuroprotection in ischemia: blocking calcium-permeable acid-sensing ion channels. *Cell* **118**, 687-698, doi:10.1016/j.cell.2004.08.026 (2004).

65 Mazzuca, M. *et al.* A tarantula peptide against pain via ASIC1a channels and opioid mechanisms. *Nature Neuroscience* **10**, 943-945, doi:10.1038/nn1940 (2007).

66 Bohlen, C. J. *et al.* A heteromeric Texas coral snake toxin targets acid-sensing ion channels to produce pain. *Nature* **479**, 410-414, doi:10.1038/nature10607 (2011).

67 Diochot, S. *et al.* Black mamba venom peptides target acid-sensing ion channels to abolish pain. *Nature* **490**, 552-555, doi:10.1038/nature11494 (2012).

68 Jensen, J. E. *et al.* Understanding the Molecular Basis of Toxin Promiscuity: The Analgesic Sea Anemone Peptide APETx2 Interacts with Acid-Sensing Ion Channel 3 and hERG Channels via Overlapping Pharmacophores. **57**, 9195-9203, doi:10.1021/jm501400p (2014).

69 Blanchard, M. G., Rash, L. D. & Kellenberger, S. Inhibition of voltage-gated Na+ currents in sensory neurones by the sea anemone toxin APETx2. *British Journal of Pharmacology* **165**, 2167-2177, doi:10.1111/j.1476-5381.2011.01674.x (2012).

70 Lynagh, T., Romero-Rojo, J. L., Lund, C. & Pless, S. A. Molecular Basis for Allosteric Inhibition of Acid-Sensing Ion Channel 1a by Ibuprofen. *J Med Chem* **60**, 8192-8200, doi:10.1021/acs.jmedchem.7b01072 (2017).

71 Lin, J. *et al.* Inhibition of Acid Sensing Ion Channel Currents by Lidocaine in Cultured Mouse Cortical Neurons. *Anesthesia & Analgesia* **112**, 977-981, doi:10.1213/ane.0b013e31820a511c (2011).

72 Leng, T., Lin, J., Cottrell, J. E. & Xiong, Z.-G. Subunit and Frequency-Dependent Inhibition of Acid Sensing Ion Channels by Local Anesthetic Tetracaine. *Molecular Pain* **9**, 1744-8069-1749-1727, doi:10.1186/1744-8069-9-27 (2013).

73 Price, M. P. *et al.* The mammalian sodium channel BNC1 is required for normal touch sensation. *Nature* **407**, 1007-1011, doi:10.1038/35039512 (2000).

74 Liu, M. G. *et al.* Acid-sensing ion channel 1a contributes to hippocampal LTP inducibility through multiple mechanisms. *Sci Rep* **6**, 23350, doi:10.1038/srep23350 (2016).

75 Du, J. *et al.* Protons are a neurotransmitter that regulates synaptic plasticity in the lateral amygdala. *Proc Natl Acad Sci U S A* **111**, 8961-8966, doi:10.1073/pnas.1407018111 (2014).

76 Wemmie, J. A. *et al.* The acid-activated ion channel ASIC contributes to synaptic plasticity, learning, and memory. *Neuron* **34**, 463-477 (2002).

77 Coryell, M. W. *et al.* Restoring acid-sensing ion channel-1a in the amygdala of knock-out mice rescues fear memory but not unconditioned fear responses. *J Neurosci* **28**, 13738-13741, doi:10.1523/JNEUROSCI.3907-08.2008 (2008).

78 Wemmie, J. A. *et al.* Overexpression of acid-sensing ion channel 1a in transgenic mice increases acquired fear-related behavior. *Proc Natl Acad Sci U S A* **101**, 3621-3626, doi:10.1073/pnas.0308753101 (2004).

79 Wemmie, J. A. *et al.* Acid-sensing ion channel 1 is localized in brain regions with high synaptic density and contributes to fear conditioning. *J Neurosci* **23**, 5496-5502 (2003).

80 Wang, Y. Z. *et al.* Tissue acidosis induces neuronal necroptosis via ASIC1a channel independent of its ionic conduction. *Elife* **4**, doi:10.7554/eLife.05682 (2015).

81 Li, M. *et al.* Acid-sensing ion channels in acidosis-induced injury of human brain neurons. *J Cereb Blood Flow Metab* **30**, 1247-1260, doi:10.1038/jcbfm.2010.30 (2010).

82 Pignataro, G., Simon, R. P. & Xiong, Z. G. Prolonged activation of ASIC1a and the time window for neuroprotection in cerebral ischaemia. *Brain* **130**, 151-158, doi:10.1093/brain/awl325 (2007).

83 Xiong, Z. G., Chu, X. P. & Simon, R. P. Ca2+ -permeable acid-sensing ion channels and ischemic brain injury. *J Membr Biol* **209**, 59-68, doi:10.1007/s00232-005-0840-x (2006).

84 Zha, X. M., Wemmie, J. A., Green, S. H. & Welsh, M. J. Acid-sensing ion channel 1a is a postsynaptic proton receptor that affects the density of dendritic spines. *Proc Natl Acad Sci U S A* **103**, 16556-16561, doi:10.1073/pnas.0608018103 (2006).

85 Zha, X. M. *et al.* ASIC2 subunits target acid-sensing ion channels to the synapse via an association with PSD-95. *J Neurosci* **29**, 8438-8446, doi:10.1523/JNEUROSCI.1284-09.2009 (2009).

86 Chiang, P. H., Chien, T. C., Chen, C. C., Yanagawa, Y. & Lien, C. C. ASIC-dependent LTP at multiple glutamatergic synapses in amygdala network is required for fear memory. *Sci Rep* **5**, 10143, doi:10.1038/srep10143 (2015).

87 Pidoplichko, V. I. *et al.* ASIC1a activation enhances inhibition in the basolateral amygdala and reduces anxiety. *J Neurosci* **34**, 3130-3141, doi:10.1523/JNEUROSCI.4009-13.2014 (2014).

88 Coryell, M. W. *et al.* Acid-sensing ion channel-1a in the amygdala, a novel therapeutic target in depression-related behavior. *J Neurosci* **29**, 5381-5388, doi:10.1523/JNEUROSCI.0360-09.2009 (2009).

89 Kreple, C. J. *et al.* Acid-sensing ion channels contribute to synaptic transmission and inhibit cocaine-evoked plasticity. *Nat Neurosci* **17**, 1083-1091, doi:10.1038/nn.3750 (2014).

90 Michaelson, D. M. & Angel, I. Determination of delta pH in cholinergic synaptic vesicles: its effect on storage and release of acetylcholine. *Life Sci* **27**, 39-44 (1980).

91 DeVries, S. H. Exocytosed protons feedback to suppress the Ca2+ current in mammalian cone photoreceptors. *Neuron* **32**, 1107-1117 (2001).

92 Palmer, M. J., Hull, C., Vigh, J. & von Gersdorff, H. Synaptic cleft acidification and modulation of short-term depression by exocytosed protons in retinal bipolar cells. *J Neurosci* **23**, 11332-11341 (2003).

93 Krishtal, O. A., Osipchuk, Y. V., Shelest, T. N. & Smirnoff, S. V. Rapid extracellular pH transients related to synaptic transmission in rat hippocampal slices. *Brain Research* **436**, 352-356, doi:10.1016/0006-8993(87)91678-7 (1987).

94 Dietrich, C. J. & Morad, M. Synaptic acidification enhances GABAA signaling. *J Neurosci* **30**, 16044-16052, doi:10.1523/JNEUROSCI.6364-09.2010 (2010).

95 González-Inchauspe, C., Urbano, F. J., Di Guilmi, M. N. & Uchitel, O. D. Acid-Sensing Ion Channels Activated by Evoked Released Protons Modulate Synaptic Transmission at the Mouse Calyx of Held Synapse. *The Journal of Neuroscience* **37**, 2589-2599, doi:10.1523/jneurosci.2566-16.2017 (2017).

96 Morgan, D. L., Borys, D. J., Stanford, R., Kjar, D. & Tobleman, W. Texas coral snake (Micrurus tener) bites. *South Med J* **100**, 152-156, doi:10.1097/01.smj.0000253596.39121.19 (2007).

97 Waldmann, R. *et al.* Molecular cloning of a non-inactivating proton-gated Na+ channel specific for sensory neurons. *J Biol Chem* **272**, 20975-20978 (1997).

98 Yu, Y. *et al.* A nonproton ligand sensor in the acid-sensing ion channel. *Neuron* **68**, 61-72, doi:10.1016/j.neuron.2010.09.001 (2010).

99 Sluka, K. A. & Gregory, N. S. The dichotomized role for acid sensing ion channels in musculoskeletal pain and inflammation. *Neuropharmacology* **94**, 58-63, doi:10.1016/j.neuropharm.2014.12.013 (2015).

100 Price, M. P. *et al.* The DRASIC Cation Channel Contributes to the Detection of Cutaneous Touch and Acid Stimuli in Mice. *Neuron* **32**, 1071-1083, doi:10.1016/s0896-6273(01)00547-5 (2001).

101 Dawson, R. J. *et al.* Structure of the acid-sensing ion channel 1 in complex with the gating modifier Psalmotoxin 1. *Nat Commun* **3**, 936, doi:10.1038/ncomms1917 (2012).

102 Grunder, S., Jaeger, N. F., Gautschi, I., Schild, L. & Rossier, B. C. Identification of a highly conserved sequence at the N-terminus of the epithelial Na+ channel alpha subunit involved in gating. *Pflugers Arch* **438**, 709-715 (1999).

103 Pfister, Y. *et al.* A gating mutation in the internal pore of ASIC1a. *J Biol Chem* **281**, 11787-11791, doi:10.1074/jbc.M513692200 (2006).

104 Coscoy, S., de Weille, J. R., Lingueglia, E. & Lazdunski, M. The pre-transmembrane 1 domain of acid-sensing ion channels participates in the ion pore. *J Biol Chem* **274**, 10129-10132 (1999).

105 Duggan, A., GarcíA-Añoveros, J. & Corey, D. P. The PDZ Domain Protein PICK1 and the Sodium Channel BNaC1 Interact and Localize at Mechanosensory Terminals of Dorsal Root Ganglion Neurons and Dendrites of Central Neurons. *Journal of Biological Chemistry* **277**, 5203-5208, doi:10.1074/jbc.m104748200 (2002).

106 Schnizler, M. K. *et al.* The cytoskeletal protein alpha-actinin regulates acid-sensing ion channel 1a through a C-terminal interaction. *J Biol Chem* **284**, 2697-2705, doi:10.1074/jbc.M805110200 (2009).

107 Sherwood, T. *et al.* Identification of protein domains that control proton and calcium sensitivity of ASIC1a. *J Biol Chem* **284**, 27899-27907, doi:10.1074/jbc.M109.029009 (2009).

108 Mukhopadhyay, M., Singh, A., Sachchidanand, S. & Bera, A. K. Quercetin inhibits acid-sensing ion channels through a putative binding site in the central vestibular region. *Neuroscience*, doi:10.1016/j.neuroscience.2017.02.025 (2017).

109 Liechti, L. A. *et al.* A combined computational and functional approach identifies new residues involved in pH-dependent gating of ASIC1a. *J Biol Chem* **285**, 16315-16329, doi:10.1074/jbc.M109.092015 (2010).

110 Vullo, S. *et al.* Conformational dynamics and role of the acidic pocket in ASIC pH-dependent gating. *Proc Natl Acad Sci U S A* **114**, 3768-3773, doi:10.1073/pnas.1620560114 (2017).

111 Springauf, A., Bresenitz, P. & Gründer, S. The interaction between two extracellular linker regions controls sustained opening of acid-sensing ion channel 1. *J Biol Chem* **286**, 24374-24384, doi:10.1074/jbc.M111.230797 (2011).

112 Li, T., Yang, Y. & Canessa, C. M. Two residues in the extracellular domain convert a nonfunctional ASIC1 into a proton-activated channel. *Am J Physiol Cell Physiol* **299**, C66-73, doi:10.1152/ajpcell.00100.2010 (2010).

113 Cushman, K. A., Marsh-Haffner, J., Adelman, J. P. & McCleskey, E. W. A conformation change in the extracellular domain that accompanies desensitization of acid-sensing ion channel (ASIC) 3. *J Gen Physiol* **129**, 345-350, doi:10.1085/jgp.200709757 (2007).

114 Grunder, S. *et al.* A mutation causing pseudohypoaldosteronism type 1 identifies a conserved glycine that is involved in the gating of the epithelial sodium channel. *EMBO J* **16**, 899-907, doi:10.1093/emboj/16.5.899 (1997).

115 Chang, S. S. *et al.* Mutations in subunits of the epithelial sodium channel cause salt wasting with hyperkalaemic acidosis, pseudohypoaldosteronism type 1. *Nat Genet* **12**, 248-253, doi:10.1038/ng0396-248 (1996).

116 Waldmann, R., Champigny, G., Voilley, N., Lauritzen, I. & Lazdunski, M. The mammalian degenerin MDEG, an amiloride-sensitive cation channel activated by mutations causing neurodegeneration in Caenorhabditis elegans. *J Biol Chem* **271**, 10433-10436 (1996).

117 Goodman, M. B. *et al.* MEC-2 regulates C. elegans DEG/ENaC channels needed for mechanosensation. *Nature* **415**, 1039-1042, doi:10.1038/4151039a (2002).

118 Garcia-Anoveros, J., Garcia, J. A., Liu, J. D. & Corey, D. P. The nematode degenerin UNC-105 forms ion channels that are activated by degeneration- or hypercontraction-causing mutations. *Neuron* **20**, 1231-1241 (1998).

119 Li, T., Yang, Y. & Canessa, C. M. Asn415 in the beta11-beta12 linker decreases proton-dependent desensitization of ASIC1. *J Biol Chem* **285**, 31285-31291, doi:10.1074/jbc.M110.160382 (2010).

120 Wu, Y., Chen, Z. & Canessa, C. M. A valve-like mechanism controls desensitization of functional mammalian isoforms of acid-sensing ion channels. *eLife* **8**, doi:10.7554/elife.45851 (2019).

121 Canessa, C. M., Horisberger, J.-D. & Rossier, B. C. Epithelial sodium channel related to proteins involved in neurodegeneration. *Nature* **361**, 467-470, doi:10.1038/361467a0 (1993).

122 Canessa, C. M. *et al.* Amiloride-sensitive epithelial Na+ channel is made of three homologous subunits. *Nature* **367**, 463-467, doi:10.1038/367463a0 (1994).

123 Kellenberger, S., Gautschi, I. & Schild, L. A single point mutation in the pore region of the epithelial Na+ channel changes ion selectivity by modifying molecular sieving. *Proc Natl Acad Sci U S A* **96**, 4170-4175 (1999).

124 Snyder, P. M., Olson, D. R. & Bucher, D. B. A pore segment in DEG/ENaC Na(+) channels. *J Biol Chem* **274**, 28484-28490 (1999).

125 Lynagh, T. *et al.* A selectivity filter at the intracellular end of the acid-sensing ion channel pore. *Elife* **6**, doi:10.7554/eLife.24630 (2017).

126 Bassler, E. L., Ngo-Anh, T. J., Geisler, H. S., Ruppersberg, J. P. & Gründer, S. Molecular and functional characterization of acid-sensing ion channel (ASIC) 1b. *J Biol Chem* **276**, 33782-33787, doi:10.1074/jbc.M104030200 (2001).

127 Yermolaieva, O., Leonard, A. S., Schnizler, M. K., Abboud, F. M. & Welsh, M. J. Extracellular acidosis increases neuronal cell calcium by activating acid-sensing ion channel 1a. *Proc Natl Acad Sci U S A* **101**, 6752-6757, doi:10.1073/pnas.0308636100 (2004).

128 Waldmann, R. & Lazdunski, M. H(+)-gated cation channels: neuronal acid sensors in the NaC/DEG family of ion channels. *Curr Opin Neurobiol* **8**, 418-424 (1998).

129 Gourdon, P. *et al.* HiLiDe—systematic approach to membrane protein crystallization in lipid and detergent. *Crystal Growth & Design* **11**, 2098-2106, doi:10.1021/cg101360d (2011).

130 Kabsch, W. Xds. *Acta Crystallogr D Biol Crystallogr* **66**, 125-132, doi:10.1107/S0907444909047337 (2010).

131 Hanson, M. A. *et al.* Crystal structure of a lipid G protein-coupled receptor. *Science* **335**, 851-855, doi:10.1126/science.1215904 (2012).

132 McCoy, A. J. Solving structures of protein complexes by molecular replacement with Phaser. *Acta Crystallogr D Biol Crystallogr* **63**, 32-41, doi:10.1107/S0907444906045975 (2007).

133 Emsley, P., Lohkamp, B., Scott, W. G. & Cowtan, K. Features and development of Coot. *Acta Crystallogr D Biol Crystallogr* **66**, 486-501, doi:10.1107/S0907444910007493 (2010).

134 Adams, P. D. *et al.* PHENIX: building new software for automated crystallographic structure determination. *Acta Crystallogr D Biol Crystallogr* **58**, 1948-1954 (2002).

135 Mastronarde, D. N. SerialEM: A program for automated tilt series acquisition on Tecnai microscopes using prediction of speciment position. *Microscopy and Microanalysis* **9**, 1182-1183 (2003).

136 Zheng, S. Q. *et al.* MotionCor2: anisotropic correction of beam-induced motion for improved cryo-electron microscopy. *Nat Methods* **14**, 331-332, doi:10.1038/nmeth.4193 (2017).

137 Zhang, K. Gctf: Real-time CTF determination and correction. *J Struct Biol* **193**, 1-12, doi:10.1016/j.jsb.2015.11.003 (2016).

138 Voss, N. R., Yoshioka, C. K., Radermacher, M., Potter, C. S. & Carragher, B. DoG Picker and TiltPicker: software tools to facilitate particle selection in single particle electron microscopy. *J Struct Biol* **166**, 205-213 (2009).

139 Scheres, S. H. RELION: Implementation of a Bayesian approach to cryo-EM structure determination. *J Struct Biol* **180**, 519-530, doi:10.1016/j.jsb.2012.09.006 (2012).

140 Grigorieff, N. Frealign: An exploratory tool for single-particle cryo-EM. *Methods Enzymol* **579**, 191-226, doi:10.1016/bs.mie.2016.04.013 (2016).

141 Heymann, J. B. Bsoft: image and molecular processing in electron microscopy. *J Struct Biol* **133**, 156-169, doi:10.1006/jsbi.2001.4339 (2001).

142 Goddard, T. D., Huang, C. C. & Ferrin, T. E. Visualizing density maps with UCSF Chimera. *J Struct Biol* **157**, 281-287, doi:10.1016/j.jsb.2006.06.010 (2007).

143 Afonine, P. V., Headd, J. J., Terwilliger, T. C. & Adams, P. D. New tool: phenix.real_space_refine. *Computational Crysatllography Newsletter* **4**, 43-44 (2013).

144 Kellenberger, S., Hoffmann-Pochon, N., Gautschi, I., Schneeberger, E. & Schild, L. On the molecular basis of ion permeation in the epithelial Na+ channel. *J Gen Physiol* **114**, 13-30 (1999).

145 Zhang, P. Single channel properties of rat acid-sensitive ion channel-1alpha, -2a, and -3 expressed in Xenopus oocytes. *The Journal of General Physiology* **120**, 553-566, doi:10.1085/jgp.20028574 (2002).

146 Gwiazda, K., Bonifacio, G., Vullo, S. & Kellenberger, S. Extracellular subunit interactions control transitions between functional states of acid-sensing ion channel 1a. *J Biol Chem* **290**, 17956-17966, doi:10.1074/jbc.M115.641688 (2015).

147 Li, T., Yang, Y. & Canessa, C. M. Leu85 in the beta1-beta2 linker of ASIC1 slows activation and decreases the apparent proton affinity by stabilizing a closed conformation. *J Biol Chem* **285**, 22706-22712, doi:10.1074/jbc.M110.134114 (2010).

148 Coric, T., Zhang, P., Todorovic, N. & Canessa, C. M. The extracellular domain determines the kinetics of desensitization in acid-sensitive ion channel 1. *J Biol Chem* **278**, 45240-45247, doi:10.1074/jbc.M304441200 (2003).

149 Bonifacio, G., Lelli, C. I. & Kellenberger, S. Protonation controls ASIC1a activity via coordinated movements in multiple domains. *J Gen Physiol* **143**, 105-118, doi:10.1085/jgp.201311053 (2014).

150 Ramaswamy, S. S., MacLean, D. M., Gorfe, A. A. & Jayaraman, V. Proton-mediated conformational changes in an acid-sensing ion channel. *J Biol Chem* **288**, 35896-35903, doi:10.1074/jbc.M113.478982 (2013).

151 Yokokawa, M., Carnally, S. M., Henderson, R. M., Takeyasu, K. & Edwardson, J. M. Acid-sensing ion channel (ASIC) 1a undergoes a height transition in response to acidification. *FEBS Lett* **584**, 3107-3110, doi:10.1016/j.febslet.2010.05.050 (2010).

152 Zuo, Z. *et al.* Identification of a unique Ca(2+)-binding site in rat acid-sensing ion channel 3. *Nat Commun* **9**, 2082, doi:10.1038/s41467-018-04424-0 (2018).

153 Kusama, N., Harding, A. M. & Benson, C. J. Extracellular chloride modulates the desensitization kinetics of acid-sensing ion channel 1a (ASIC1a). *J Biol Chem* **285**, 17425-17431, doi:10.1074/jbc.M109.091561 (2010).

154 Collier, D. M. & Snyder, P. M. Identification of epithelial Na+ channel (ENaC) intersubunit Cl- inhibitory residues suggests a trimeric alpha gamma beta channel architecture. *J Biol Chem* **286**, 6027-6032, doi:10.1074/jbc.M110.198127 (2011).

155 Collier, D. M. & Snyder, P. M. Extracellular chloride regulates the epithelial sodium channel. *J Biol Chem* **284**, 29320-29325, doi:10.1074/jbc.M109.046771 (2009).

156 Yoder, N., Yoshioka, C. & Gouaux, E. Gating mechanisms of acid-sensing ion channels. *Nature* **555**, 397-401, doi:10.1038/nature25782 (2018).

157 Reeves, P. J., Callewaert, N., Contreras, R. & Khorana, H. G. Structure and function in rhodopsin: high-level expression of rhodopsin with restricted and homogeneous N-glycosylation by a tetracycline-inducible N-acetylglucosaminyltransferase I-negative HEK293S stable mammalian cell line. *Proc Natl Acad Sci U S A* **99**, 13419-13424, doi:10.1073/pnas.212519299 (2002).

158 Adams, P. D. *et al.* PHENIX: a comprehensive Python-based system for macromolecular structure solution. *Acta Crystallogr D Biol Crystallogr* **66**, 213-221, doi:10.1107/S0907444909052925 (2010).

159 Jiang, C., Agulian, S. & Haddad, G. G. Cl- and Na+ homeostasis during anoxia in rat hypoglossal neurons: intracellular and extracellular in vitro studies. *J Physiol* **448**, 697-708 (1992).

160 Plested, A. J. & Mayer, M. L. Structure and mechanism of kainate receptor modulation by anions. *Neuron* **53**, 829-841, doi:10.1016/j.neuron.2007.02.025 (2007).

161 Hu, R. *et al.* Role of acid-sensing ion channel 1a in the secondary damage of traumatic spinal cord injury. *Ann Surg* **254**, 353-362, doi:10.1097/SLA.0b013e31822645b4 (2011).

162 Yin, T. *et al.* Loss of Acid sensing ion channel-1a and bicarbonate administration attenuate the severity of traumatic brain injury. *PLoS One* **8**, e72379, doi:10.1371/journal.pone.0072379 (2013).

163 Duan, B. *et al.* Extracellular spermine exacerbates ischemic neuronal injury through sensitization of ASIC1a channels to extracellular acidosis. *J Neurosci* **31**, 2101-2112, doi:10.1523/JNEUROSCI.4351-10.2011 (2011).

164 Noreng, S., Bharadwaj, A., Posert, R., Yoshioka, C. & Baconguis, I. Structure of the human epithelial sodium channel by cryo-electron microscopy. *Elife* **7**, doi:10.7554/eLife.39340 (2018).

165 Suloway, C. *et al.* Automated molecular microscopy: The new Leginon system. *Journal of Structural Biology* **151**, 41-60, doi:10.1016/j.jsb.2005.03.010 (2005).

166 Punjani, A., Rubinstein, J. L., Fleet, D. J. & Brubaker, M. A. cryoSPARC: algorithms for rapid unsupervised cryo-EM structure determination. *Nature Methods* **14**, 290-296, doi:10.1038/nmeth.4169 (2017).

167 Knowles, T. J. *et al.* Membrane Proteins Solubilized Intact in Lipid Containing Nanoparticles Bounded by Styrene Maleic Acid Copolymer. *Journal of the American Chemical Society* **131**, 7484-7485, doi:10.1021/ja810046q (2009).

168 Dörr, J. M. *et al.* Detergent-free isolation, characterization, and functional reconstitution of a tetrameric K+channel: The power of native nanodiscs. *Proc Natl Acad Sci U S A* **111**, 18607-18612, doi:10.1073/pnas.1416205112 (2014).

169 Kawate, T. & Gouaux, E. Fluorescence-detection size-exclusion chromatography for precrystallization screening of integral membrane proteins. *Structure* **14**, 673-681, doi:10.1016/j.str.2006.01.013 (2006).

170 Kellenberger, S., Auberson, M., Gautschi, I., Schneeberger, E. & Schild, L. Permeability properties of ENaC selectivity filter mutants. *J Gen Physiol* **118**, 679-692 (2001).

171 Esmaili, M. & Overduin, M. Membrane biology visualized in nanometer-sized discs formed by styrene maleic acid polymers. *Biochim Biophys Acta*, doi:10.1016/j.bbamem.2017.10.019 (2017).

172 Teo, A. C. K. *et al.* Analysis of SMALP co-extracted phospholipids shows distinct membrane environments for three classes of bacterial membrane protein. *Scientific Reports* **9**, doi:10.1038/s41598-018-37962-0 (2019).

173 A., L. M. S. M. D. J. P. C. MLPP: A program for the calculation of molecular lipophilicity potential in proteins. *Pharm. Sci.*, doi:10.1111/j.2042-7158.1997.tb00257.x (1997).

174 Goddard, T. D. *et al.* UCSF ChimeraX: Meeting modern challenges in visualization and analysis. *Protein Science* **27**, 14-25, doi:10.1002/pro.3235 (2018).

175 Nakane, T., Kimanius, D., Lindahl, E. & Scheres, S. H. Characterisation of molecular motions in cryo-EM single-particle data by multi-body refinement in RELION. *eLife* **7**, doi:10.7554/elife.36861 (2018).

176 Zhang, C. *et al.* Analysis of discrete local variability and structural covariance in macromolecular assemblies using Cryo-EM and focused classification. *Ultramicroscopy* **203**, 170-180, doi:10.1016/j.ultramic.2018.11.016 (2019).

177 Fischer, N., Konevega, A. L., Wintermeyer, W., Rodnina, M. V. & Stark, H. Ribosome dynamics and tRNA movement by time-resolved electron cryomicroscopy. *Nature* **466**, 329-333, doi:10.1038/nature09206 (2010).

178 Unwin, N. Structure and action of the nicotinic acetylcholine receptor explored by electron microscopy. *FEBS Lett* **555**, 91-95 (2003).

179 Unwin, N. Acetylcholine receptor channel imaged in the open state. *Nature* **373**, 37-43, doi:10.1038/373037a0 (1995).

180 Matsubara, N., Billington, A. P. & Hess, G. P. How fast does an acetylcholine receptor channel open? Laser-pulse photolysis of an inactive precursor of carbamoylcholine in the microsecond time region with BC3H1 cells. *Biochemistry* **31**, 5507-5514 (1992).

181 Kaledhonkar, S., Fu, Z., White, H. & Frank, J. Time-Resolved Cryo-electron Microscopy Using a Microfluidic Chip. *Methods Mol Biol* **1764**, 59-71, doi:10.1007/978-1-4939-7759-8_4 (2018).

182 Feng, X. *et al.* A Fast and Effective Microfluidic Spraying-Plunging Method for High-Resolution Single-Particle Cryo-EM. *Structure* **25**, 663-670 e663, doi:10.1016/j.str.2017.02.005 (2017).

183 Lu, Z. *et al.* Gas-Assisted Annular Microsprayer for Sample Preparation for Time-Resolved Cryo-Electron Microscopy. *J Micromech Microeng* **24**, 115001, doi:10.1088/0960-1317/24/11/115001 (2014).

184 Kharlamova, A., Prentice, B. M., Huang, T. Y. & McLuckey, S. A. Electrospray droplet exposure to gaseous acids for the manipulation of protein charge state distributions. *Anal Chem* **82**, 7422-7429, doi:10.1021/ac101578q (2010).

185 Fu, Z. *et al.* The structural basis for release-factor activation during translation termination revealed by time-resolved cryogenic electron microscopy. *Nature Communications* **10**, doi:10.1038/s41467-019-10608-z (2019).

186 Chen, B. *et al.* Structural Dynamics of Ribosome Subunit Association Studied by Mixing-Spraying Time-Resolved Cryogenic Electron Microscopy. **23**, 1097-1105, doi:10.1016/j.str.2015.04.007 (2015).

187 White, H. D., Walker, M. L. & Trinick, J. A computer-controlled spraying-freezing apparatus for millisecond time-resolution electron cryomicroscopy. *J Struct Biol* **121**, 306-313, doi:10.1006/jsbi.1998.3968 (1998).

188 White, H. D., Thirumurugan, K., Walker, M. L. & Trinick, J. A second generation apparatus for time-resolved electron cryo-microscopy using stepper motors and electrospray. *J Struct Biol* **144**, 246-252 (2003).

189 Shaikh, T. R., Barnard, D., Meng, X. & Wagenknecht, T. Implementation of a flash-photolysis system for time-resolved cryo-electron microscopy. *J Struct Biol* **165**, 184-189, doi:10.1016/j.jsb.2008.11.007 (2009).

190 Subramaniam, S. & Henderson, R. Electron crystallography of bacteriorhodopsin with millisecond time resolution. *J Struct Biol* **128**, 19-25, doi:10.1006/jsbi.1999.4178 (1999).

191 Subramaniam, S., Gerstein, M., Oesterhelt, D. & Henderson, R. Electron diffraction analysis of structural changes in the photocycle of bacteriorhodopsin. *EMBO J* **12**, 1-8 (1993).

192 Callaway, E. M. & Yuste, R. Stimulating neurons with light. *Current Opinion in Neurobiology* **12**, 587-592, doi:10.1016/s0959-4388(02)00364-1 (2002).

193 Korkotian, E., Oron, D., Silberberg, Y. & Segal, M. Confocal microscopic imaging of fast UV-laser photolysis of caged compounds. *Journal of Neuroscience Methods* **133**, 153-159, doi:10.1016/j.jneumeth.2003.10.007 (2004).

194 Eder, M., Zieglgänsberger, W. & Dodt, H.-U. in *Reviews in the Neurosciences* Vol. 15 167 (2004).

195 Watanabe, S. *et al.* Ultrafast endocytosis at mouse hippocampal synapses. *Nature* **504**, 242-247, doi:10.1038/nature12809 (2013).

196 Watanabe, S. *et al.* Clathrin regenerates synaptic vesicles from endosomes. *Nature* **515**, 228-233, doi:10.1038/nature13846 (2014).

197 Kaplan, J. H., Forbush, B. & Hoffman, J. F. Rapid photolytic release of adenosine 5'-triphosphate from a protected analog: utilization by the sodium:potassium pump of human red blood cell ghosts. *Biochemistry* **17**, 1929-1935, doi:10.1021/bi00603a020 (1978).

198 Wieboldt, R., Ramesh, D., Carpenter, B. K. & Hess, G. P. Synthesis and Photochemistry of Photolabile Derivatives of .gamma.-Aminobutyric Acid for Chemical Kinetic Investigations of the .gamma.-Aminobutyric Acid Receptor in the Millisecond Time Region. *Biochemistry* **33**, 1526-1533, doi:10.1021/bi00172a032 (1994).

199 Wieboldt, R. *et al.* Photolabile precursors of glutamate: synthesis, photochemical properties, and activation of glutamate receptors on a microsecond time scale. *Proc Natl Acad Sci U S A* **91**, 8752-8756, doi:10.1073/pnas.91.19.8752 (1994).

200 Breitinger, H.-G. A., Wieboldt, R., Ramesh, D., Carpenter, B. K. & Hess, G. P. Synthesis and Characterization of Photolabile Derivatives of Serotonin for Chemical Kinetic Investigations of the Serotonin 5-HT3Receptor†. *Biochemistry* **39**, 5500-5508, doi:10.1021/bi992781q (2000).

201 Araya, R., Andino-Pavlovsky, V., Yuste, R. & Etchenique, R. Two-Photon Optical Interrogation of Individual Dendritic Spines with Caged Dopamine. *ACS Chemical Neuroscience* **4**, 1163-1167, doi:10.1021/cn4000692 (2013).

202 Kasas, S., Dumas, G., Dietler, G., Catsicas, S. & Adrian, M. Vitrification of cryoelectron microscopy specimens revealed by high-speed photographic imaging. *Journal of Microscopy* **211**, 48-53, doi:10.1046/j.1365-2818.2003.01193.x (2003).

203 Matsuzaki, M. *et al.* Dendritic spine geometry is critical for AMPA receptor expression in hippocampal CA1 pyramidal neurons. *Nature Neuroscience* **4**, 1086-1092, doi:10.1038/nn736 (2001).

204 Abbruzzetti, S., Sottini, S., Viappiani, C. & Corrie, J. E. Kinetics of proton release after flash photolysis of 1-(2-nitrophenyl)ethyl sulfate (caged sulfate) in aqueous solution. *J Am Chem Soc* **127**, 9865-9874, doi:10.1021/ja051702x (2005).

205 Araya, R., Eisenthal, K. B. & Yuste, R. Dendritic spines linearize the summation of excitatory potentials. *Proc Natl Acad Sci U S A* **103**, 18799-18804, doi:10.1073/pnas.0609225103 (2006).

206 Digregorio, D. A., Rothman, J. S., Nielsen, T. A. & Silver, R. A. Desensitization Properties of AMPA Receptors at the Cerebellar Mossy Fiber Granule Cell Synapse. *Journal of Neuroscience* **27**, 8344-8357, doi:10.1523/jneurosci.2399-07.2007 (2007).

207 Pugh, J. R. & Jahr, C. E. NMDA Receptor Agonists Fail To Alter Release from Cerebellar Basket Cells. *Journal of Neuroscience* **31**, 16550-16555, doi:10.1523/jneurosci.3910-11.2011 (2011).

208 Carter, B. C. & Jahr, C. E. Postsynaptic, not presynaptic NMDA receptors are required for spike-timing-dependent LTD induction. *Nature Neuroscience* **19**, 1218-1224, doi:10.1038/nn.4343 (2016).